Design and Fabrication of the MesoMill: A Five-Axis Milling Machine for Meso-Scaled parts

by

Jaime Brooke Werkmeister

B. S. Mechanical Engineering
University of California, San Diego, 2001

SUBMITTED TO THE DEPARTMENT OF MECHANICAL ENGINEERING
IN PARTIAL FULFILLMENT OF THE REQUIREMENTS FOR THE DEGREE OF

MASTER OF SCIENCE IN MECHANICAL ENGINEERING
AT THE
MASSACHUSETTS INSTITUTE OF TECHNOLOGY
[June 2004]
May 2004

Signature of Author.....
Department of Mechanical Engineering
May 7, 2004

Certified by.....
.....
nder H. Slocum
ical Engineering
hesis Supervisor

Accepted by.....
.....
Ain Sonin
cal Engineering
Chairman, Committee for Graduate Students

Design and Fabrication of the MesoMill: A Five-Axis Milling Machine for Meso-Scaled parts

by

Jaime Brooke Werkmeister

Submitted to the Department of Mechanical Engineering
on May 7, 2004 in Partial Fulfillment of the
Requirements for the Degree of Master of Science in
Mechanical Engineering

Abstract

With the increased prevalence of meso-scaled products, new tools are being developed to bridge the gap between fabrication processes tailored for micrometer and millimeter sized features. Compared to its traditional counterpart, a small machine tool designed for meso-scale could potentially have a smaller overall footprint, shorter structural loop and lower cost than a conventional machine; in addition, a small machine presents opportunities for improved machine metrology, and easier environmental control. This paper describes the design of the MesoMill: a test machine designed to evaluate the use of components new to the design of machining centers including wire capstan drives, ball-screw splines, and an air bearing spindle with an integral Z-axis.

Thesis Supervisor: Alexander H. Slocum
Title: Professor of Mechanical Engineering

Acknowledgements

The fabrication of the Mesomill would have not been possible without the aid of Wojciech Kosmowski and Mark Kosmowski of ESI who donated the Westwind aerostatic spindle. Kevan Perkins at THK donated the ball-screw spline. Thomas Massie of SensAble Technologies donated a capstan drive for initial experiments. Sava Industries donated the steel cable for the capstan drive and Alkan Donmez and Brad Damazo of NIST offered their endless knowledge and support in seeing the Mesomill built and tested.

I extend thanks to Mike Roberts who worked on experimentation for the beam bending calculations, Margaret Cho for building the capstan experimental setup, and Brian LaCrosse and Pierece Hayward for helping with the cable testing in the Instron™ machine.

A big thank you also extends to my family and friends. As always my Mom and Dad have been very supporting and encouraging through these few years and through the distant past. Thank you for your encouraging words and long venting hours on the phone. I'm glad the west coast is 3 hours behind the East. By the time I go to bed it's still a decent hour to call and by the time I get up my dad is up going to work. My labmates have been supportive as well. They gave me the right advice at the right time and endless laughs. Special thanks goes to Patrick Willoughby for throwing ketchup packets at me when I slacked off and lending an ear when I needed advise.

Most of all thank you Alex Slocum. He has served as an advisor and friend. He has given me strength and courage in conquering the battle of writing (by the way I still owe him a red pen.) Alex has given me good advice and is a great source of enthusiasm about engineering. I am looking forward to doing my Phud with him.

Table of Contents

1 Introduction

The objective of this thesis is to present the design of the MesoMill: a five-axis milling machine with intersecting sets of modular axes for the machining of meso-scaled parts. Detailed calculations of choosing and sizing the components of the MesoMill will be discussed.

With the increased prevalence of meso-scaled products, new tools are being developed to bridge the gap between fabrication processes tailored for micrometer and millimeter sized features [1][**2**]. Compared to its traditional counterpart [3], a small machine tool designed for meso-scale could potentially have a smaller overall footprint, shorter structural loop and lower cost than a conventional machine; in addition, a small machine presents opportunities for improved machine metrology, and easier environmental control. This thesis describes the design of the MesoMill: a test machine designed to evaluate the use of components new to the design of machining centers including wire capstan drives, ball-screw splines, and an air bearing spindle with an integral Z-axis.

1.1 Currently Available Machines

Compared to its traditional counterpart, a small machine tool designed for meso-scale parts has the advantages of: ease-of-use, smaller footprint, smaller structural loop, shorter distances between the work piece and the machine's metrology devices, opportunities for improved machine metrology, and easier environmental control [4][5].

There are many machines that can mill small parts, small as in no larger than a 25 mm cube. For instance the 2000/2010 mill by Sherline Products [6]. The overall size of this machine is 381 x 565 x 568 mm and has a tolerance of 10-12 microns. Another machine is the Prazi BF400-450 Powermill Series Precision Benchtop Milling Machine [7] with an accuracy of 5 microns. Its dimensions are 585 x 559 x 813 mm. Similarly, one other machine that produces small parts is the Star Machine by Small Engineering [8]. They specialize in small parts and obtain tolerance of ±5microns, but they use a large machine, roughly 2 x 1.5 x 1 m, to fabricate small parts.

The Modela, model number MDX15 and MDX20, [9][10] is capable of milling and scanning, and is designed for 3D modeling, however given the broad range of tools and accessories available, the Modela can do light machining and PCB manufacturing. The dimensions of the Modela's MDX-15E are 426 x 280 x 305 mm and has a scanning resolution of 50 microns. Another machine, the HexVantage™ by Pathfinders Incorporated [11], can machine in 5 axes and obtain resolution of 0.2 microns per count of its encoder and has an accuracy of 12 microns. This version of a Hexapod can fit on the bench top with dimensions of 1.2 x 1.2 x 1.2 m [12]. Light Machines' Benchman™ small machining centers are designed to be placed on top of a bench, and operate with high speed spindles for CNC machining of small parts with features as small as 10-20 microns [13].

Sandia National Laboratories in their Manufacturing Science and Technology Center [14], have began to develop four new meso-machining technologies which are: Focused ion beam (FIB) machining, Micro-milling and –turning, Excimer and Femto-second laser, and Micro-Electro Discharge Machining (Micro-EDM) [15]. These meso-machines will create features sizes in the micron range between 1-50 microns. The Micro-wire EDM has a positional accuracy of ±1.5 microns and the Femto-second laser machining can machine a hole with a micron in diameter.

Researchers have also been investigating new approaches to machine and process design for manufacture of small parts. For example, DeVor and Kapoor at the University of Illinois [16] have been working on the "Development of a Meso-Machine Tool System" [17], and indications are that it is indeed worthwhile to investigate configurations for meso machines that are not merely scaled-down versions of macro machines.

1.2 Characteristics of the MesoMill

When considering the manufacture of small parts, one design option not regularly used in large machines, due to size issues, is collinearity of axes. Given this design, a logical question that was sought to be answered was can a ball-screw spline shaft, which can provide linear and rotary motions, be oversized so it could also serve as the principal moving structural element? It is this concept that was chosen for consideration. A MesoMill which uses this concept is shown in Figure 1. It is designed to be a 5-axis milling machine that is capable of machining components no larger than a 25 mm cube and it has a size of about 400 x 400 x 400 mm. A five-axis machine allows for five sides of a part to be machined in one setup, thus minimizing errors introduced by re-clamping [18].

The fundamental design principle of the Mesomill is to use two intersecting linear/rotary axes which support the workpiece and a Z-θ spindle assembly, respectively. The air bearing spindle, from an ESI circuit board drilling machine, has a speed range of 40,000 to 110,000 rpm, and the spindle incorporates a linear machining axis in Z with a travel of 10 mm. The other four machining axes are realized by two identical orthogonal THK[1] ball-screw splines, each producing a combination of linear and rotary movement. Wire capstan drives couple the servo motors to the ball-screw spline. This design has the advantage of no backlash and a high rotational stiffness on the order of 6,000 N-m/rad. Positioning feedback is achieved close to the workpiece using a new encoder capable of simultaneously measuring both linear and rotary movement. An error budget of the machine was developed, and used to help determine the proper placement of the nuts on the ball-screw spline shafts to give an "optimal" spacing to reduce errors.

[1] Commercial equipment, instruments, or materials are identified in this thesis in order to specify adequately certain procedures. In no case, does such identification imply recommendation or endorsement by the author, nor does it imply that the material or equipment identified is necessarily the best available for the purpose.

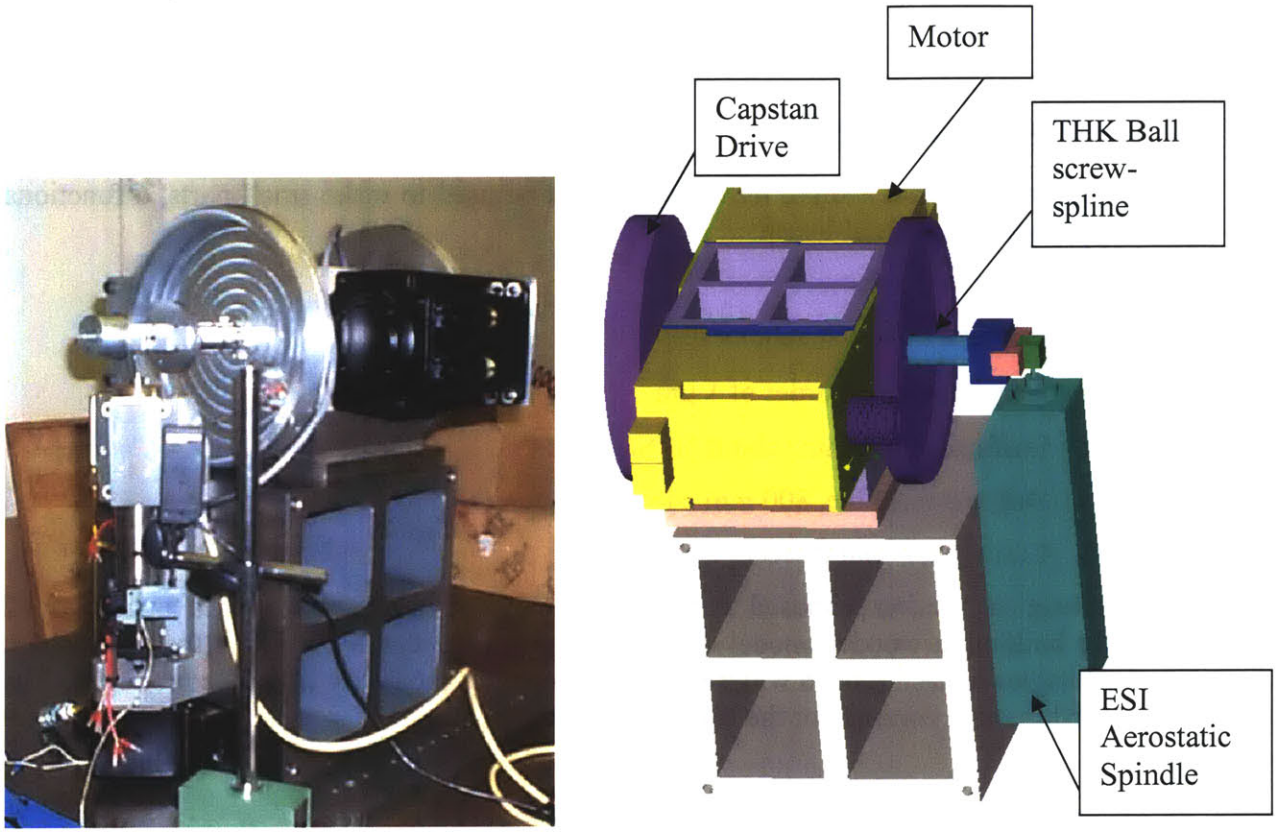

Figure 1: MesoMill prototype (left) and solid model (right)

2 Background

The hypotheses that a small machine can best be used to make small parts, 6 functional requirements were established:

1. Move in 5 axis
2. Part size of 1 inch cube or less
3. Accuracy on the order of 1 μm
4. Stiffness of machine about 50 N/ μm
5. Desktop machine, 800 mm cube and
6. Cutting material is steel

The original version proposed by Professor Slocum, had two axis crossed as in Figure 2. After building a wooden model of this configuration, it was noticed if the axis were at right angles to each other a wider range of machining capability would be produced. This created the first concept for the MesoMill.

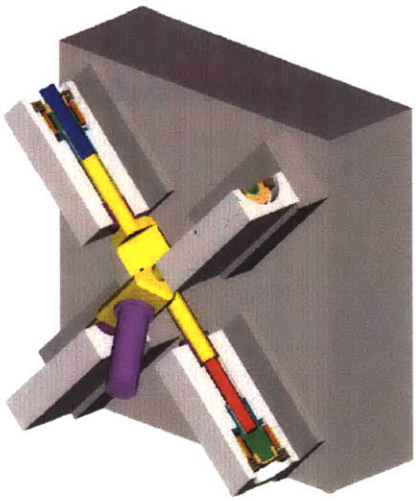

Figure 2: Preliminary concept of the MesoMill presented by Professor Slocum

The main concern having a machine this small is its stiffness and damping characteristics. A small machine that has insufficient stiffness and cannot damp the vibrations from the cutting force is inadequate compared to the standard precision CNC machines[2][3][4]. To overcome these features, the ball screw spline shaft by THK [19] was looked upon, along with air bearings by New Way Bearings[5] to control the chatter from the aerostatic spindle which was donated by ESI[6].

---

[2] Bobő Services Group, Inc. Esslingen, Germany, 1996. http://www.boko.com/
[3] Mecona Teknik AB, Keckel Maho DMU 50 eVolution, 2002. http://www.mecona.se/dmu50ev.htm
[4] Makino, 5-axis machining center, 2000. http://www.makino.co.jp/product_e/
[5] NewWay Bearing, http://newwaybearings.com/productpages/airbushings.html
[6] ESI Corporation, http://www.esi.com/

Analysis was performed on the MesoMill. These include: error analysis, tool stiffness, beam bending, natural frequency of the system, and motor determination (capstan drive, dual pinion, iterative process to figure out proper motor.) The analysis will be discussed in more detail in chapter 4.

Secondly, experiments were performed to confirm analytic results, and gather data where calculations could not be performed. The experiments include: bending the shaft under a given force, stiffness of air bearings, torsional stiffness of a capstan drive, and errors in an aerostatic spindle. The experiments and results are shown in Chapter 5.

In Chapter 6, suggestion will be given and then the conclusion will follow to put everything in perspective. References are listed at the end but before the Appendix. The appendix contains evolutionary pictures of the MesoMill, data, and further details of the calculations.

3 Preliminary Concepts of the MesoMill

Presented below are the preliminary design concepts of the MesoMill. Each version was updated as more analysis was performed.

Initial concept of the MesoMill which was originally presented by Professor Slocum. Note the axes are crossed.

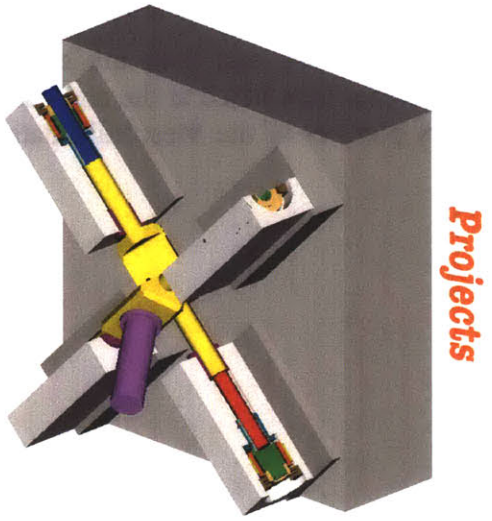

Figure 3: Concept 1 of MesoMill by Professor Slocum.

Sketch to see if possible to machine in all 5 axis and if the axis could be perpendicular (right angle) to each other instead of crossed. It was shown the right angle axes can machine efficently compared to the crossed. More components were needed if the axes were crossed as in Figure 3.

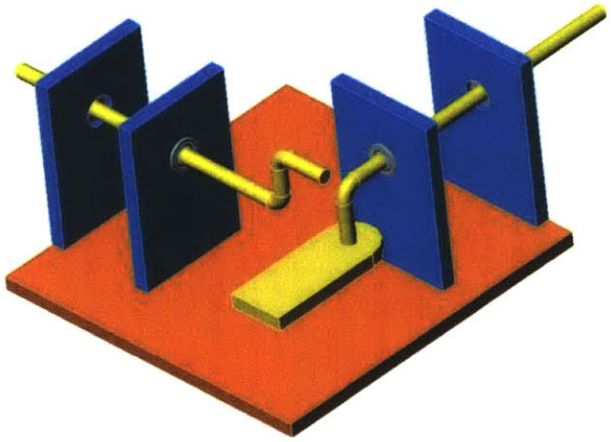

Figure 4: Determination if can machine on all 5-axis.

Bench level experiment of the solid model in Figure 4 is given in Figure 5. This experiment was to see if the right angle axis would be able to machine in all 5 axes.

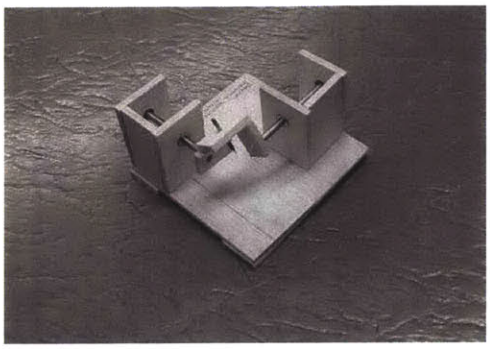

Figure 5: Bench level experiment of machining capability of MesoMill.

Solidworks representation of what the MesoMill could look like. Since this is an early drawing, all the components were still being sized.

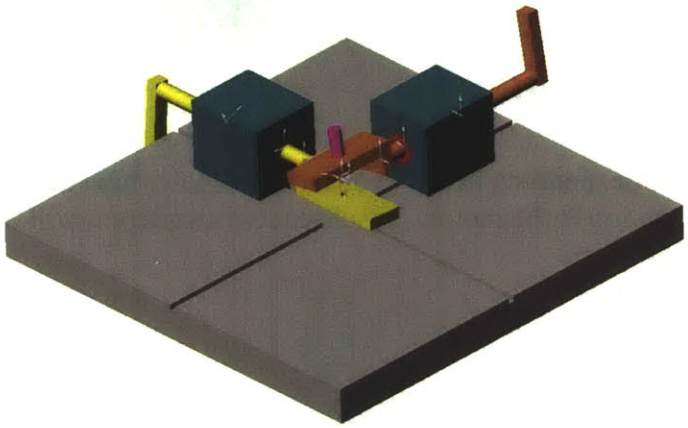

Figure 6: Preliminary sketch model of MesoMill

Bench level Experiment of how the right angle axis would move in relation to the other axis.

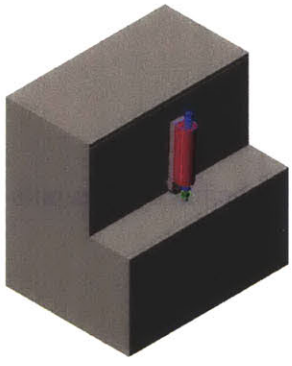

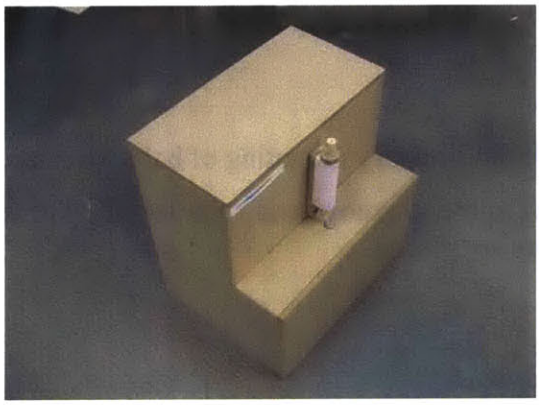

Figure 7: Bench level experiments of how axes would move in relation to each other.

Below is the overall configuration of the MesoMill with the two axes, spindle and work piece at right angles to each other. The large cylinders are the motors that drive the ballscrew-spline nuts and the rectangles are where the air bearings would reside.

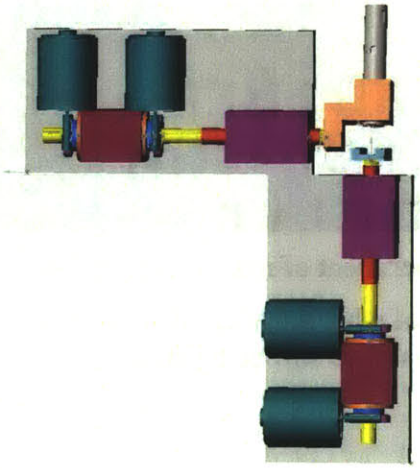

Figure 8: Configuration of axis.

The spindle axis will be mounted in a V-groove. This shows how the spindle will move. The long rectangle on top is the motor. In subsequent chapters it will be shown the V-groove is not necessary.

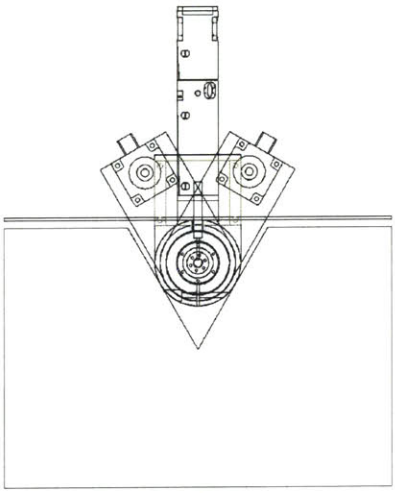

Figure 9: Preliminary mounting of ballscrew-spline in holder

Side view of the V-groove and spindle axis. The rectangle in the back represents where the motors are placed.

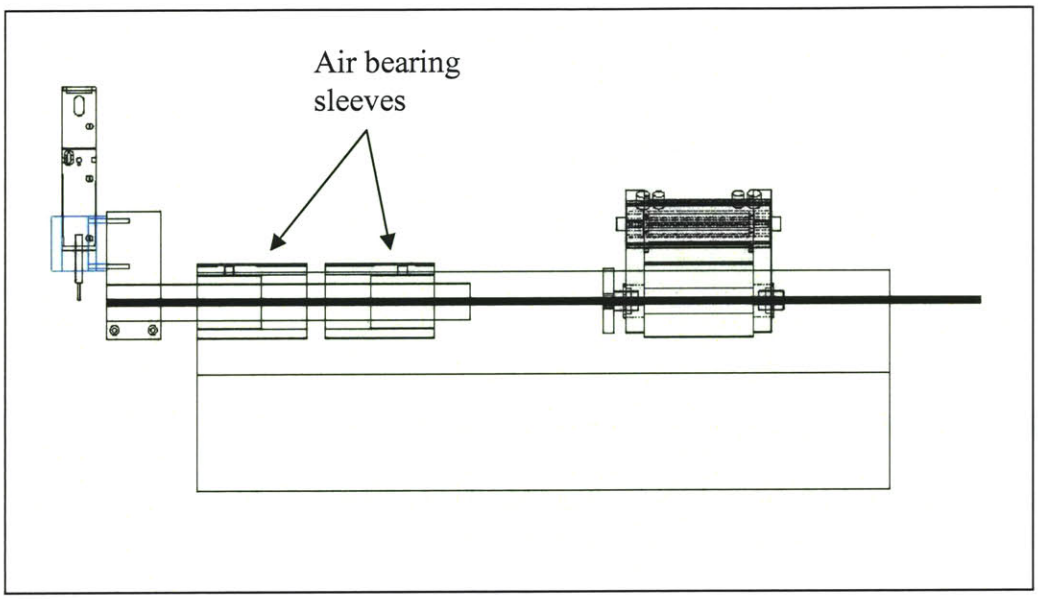

Figure 10: Side view of v-groove mounting.

Isometric view of what the spindle axis will look like. How the shaft will be attached is shown by the copper color plates.

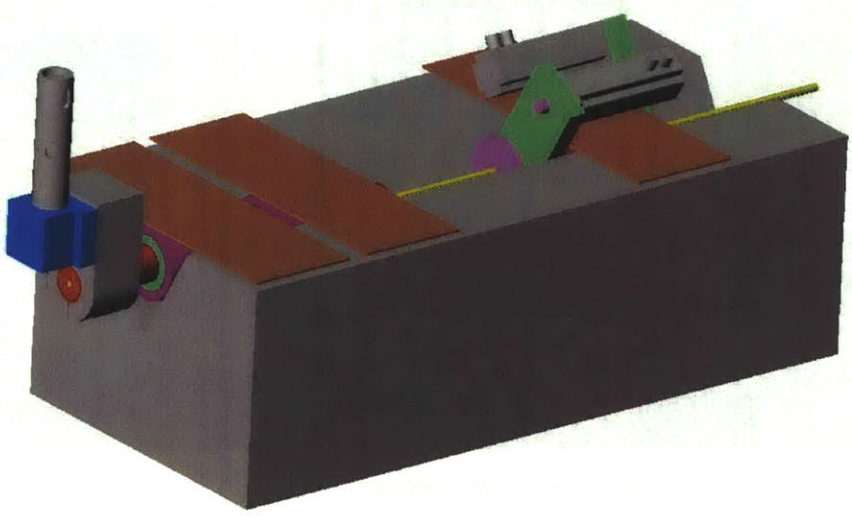

Figure 11: Overall view of v-groove mounting of spindle axis.

Drawing of the experiment apparatus. The goal was to see how much the tip deflects if a force is implemented between the ball screw-spline shaft (by THK.)

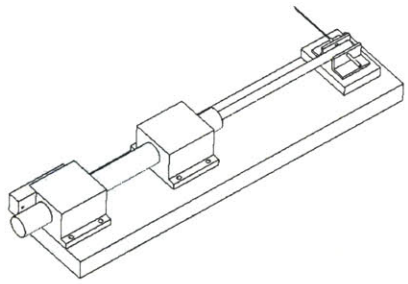

Figure 12: Model of the experimental setup of ball screw-spline

Linear bearings with a shaft through them. Steel blocks on the side hold the capacitance probes. These devices send out a voltage when movement is detected.

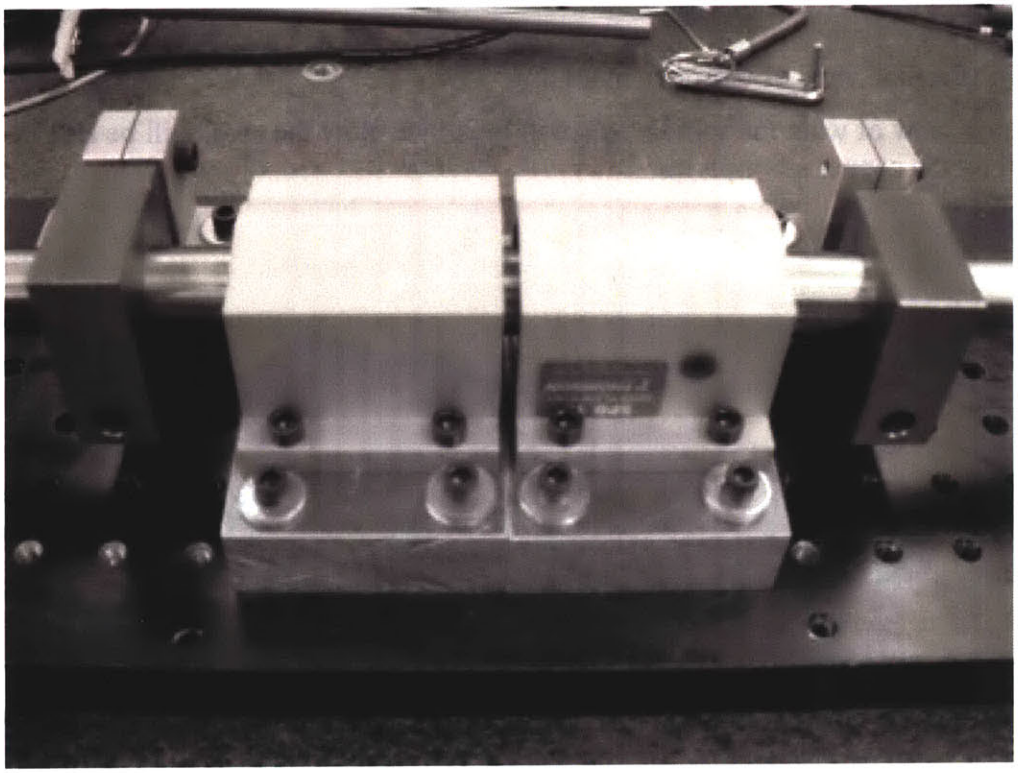

Figure 13: Bearing block experimentation setup.

Long view of what the shaft and linear bearings looked like.

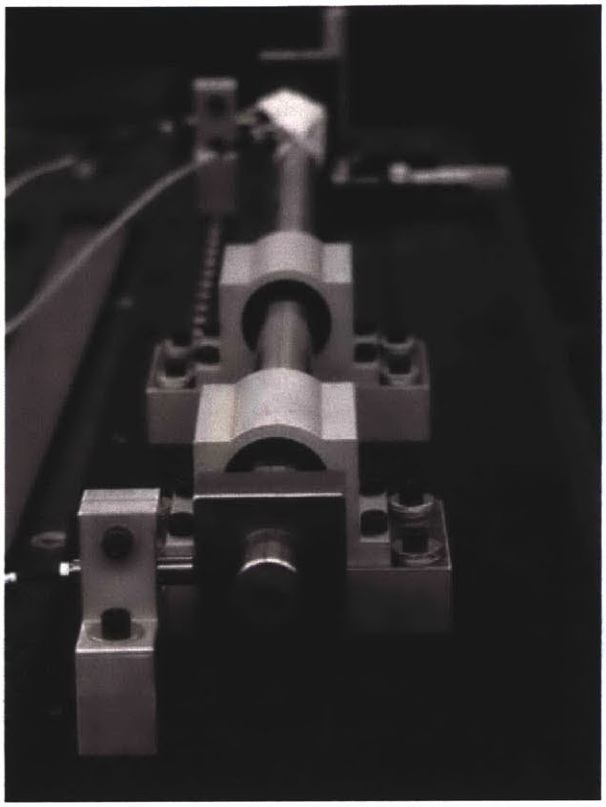

Figure 14: Long view of bearing block experimentation.

Top view of the input force onto the shaft and the detection of movement by the capacitance probe (bottom left of picture.) Square block on the shaft was used in aligning and detecting movement of the shaft.

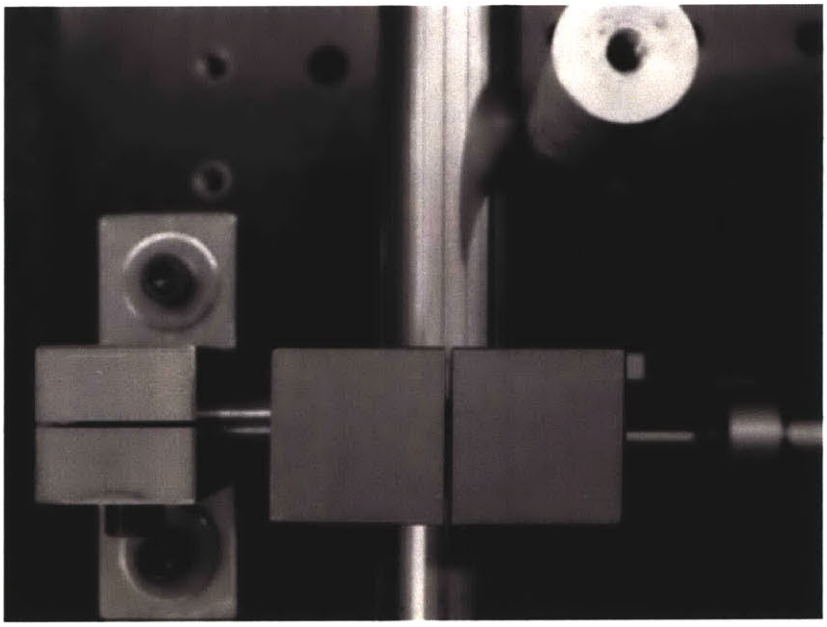

Figure 15: Top view of bearing block experimentation.

For the results of these experimentations refer to Chapter 6.

Lastly the final concept for the MesoMill is shown below.

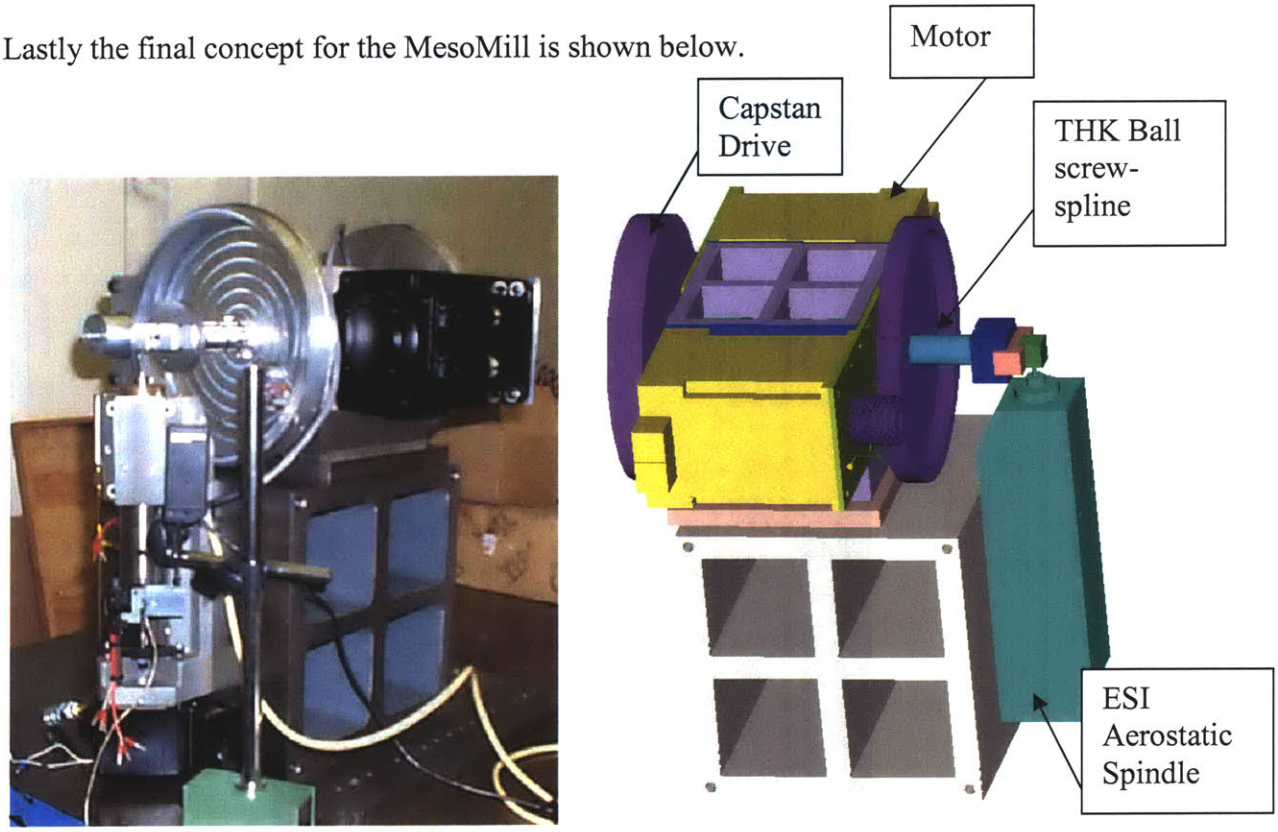

Figure 16: MesoMill final concept.

4 Calculations

There were many calculations performed to determine the feasibility of the MesoMill. Calculations performed on the ball screw-spline shaft were: error analysis, tool stiffness, beam bending, natural frequency, V-block hertz contact/top plate bending, and motor sizing. The calculations performed to compare two options for the transmission were a cable capstan drive and dual pinion. Each calculation is described below and the results are presented in the results section.

4.1 Error Analysis

An error budget of the MesoMill was created to compare it to a normal size machine which assesses whether the concept has merit. The MesoMill can be divided into two primary components, the work and tool path, which each are attached to a comparatively rigid base, as shown in Figure 1. In Figure 17 the structural loop of the work and tool path is shown. The total distance from the reference base to D_5 is considered the work path where: D_1 is the distance from the reference to the midsection between the two nuts on the ball-screw spline, D_2 is the distance from the midpoint of the nuts to the end of the ball-screw spline shaft where the disc connects, D_3 is the distance from the end of the shaft through the thickness of the disc, D_4 is the distance from the disc to the fixture, and D_5 is the distance from the fixture to the part. The total distance from D_6 through D_{12} is considered the tool path where: D_6 is the distance from the tool tip to the collet, D_7 is the distance from the collet to the center of the shaft in the air bearing spindle which gives the spindle translation, D_8 is the distance from the shaft center to the air bearings in the aerostatic spindle, D_9 is the distance from the air bearings to the spindle holder mount, D_{10} is the distance from the holder to its connection on the ball-screw spline shaft, D_{11} is the distance from the end of the shaft to the midpoint of the ball-screw spline nuts, and D_{12} is the distance from the midpoint of these nuts to the reference base.

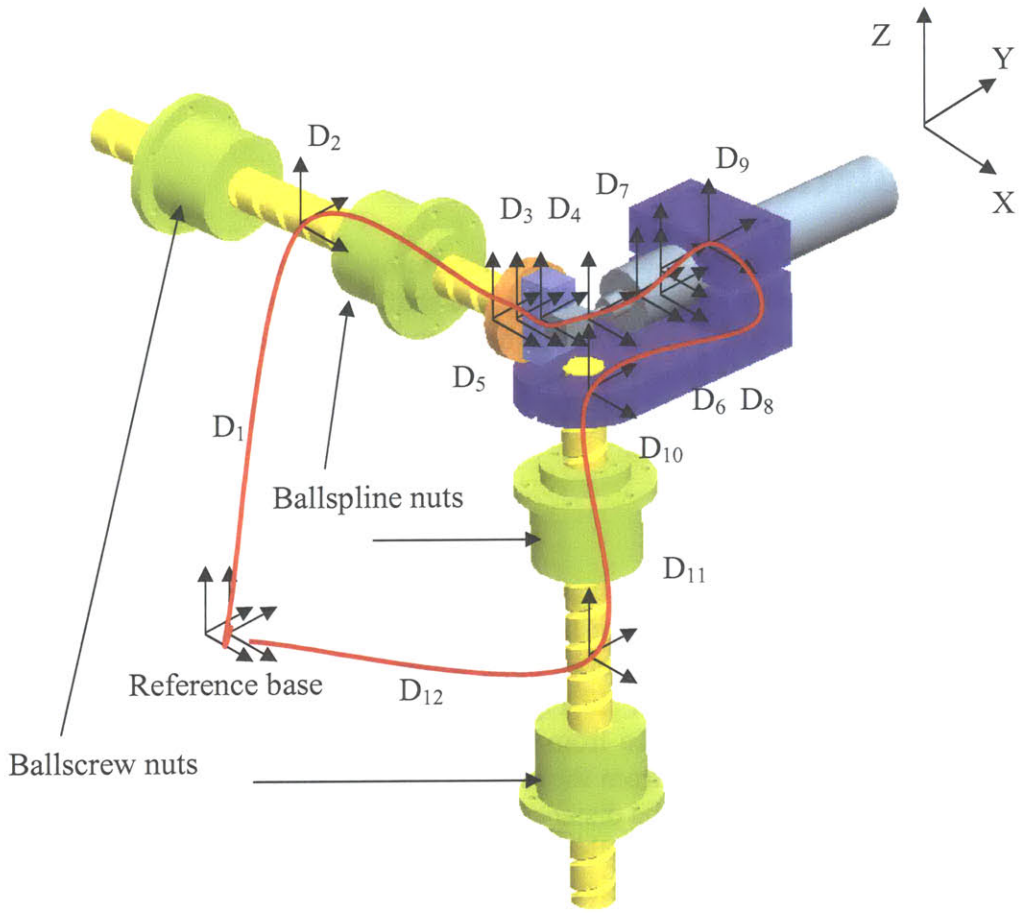

Figure 17: Structural Loop, shown in red, of the MesoMill: Work path is from the work piece to the center of the nuts (D_1-D_5). The tool path is from tip of tool to the center of the nuts (D_5-D_{12}).

Given the right angle configuration shown in Figure 17, Table 1, and Table 2 show the estimated errors for each distance $D_1 - D_5$ for the work path and $D_5 - D_{12}$ for the tool path. For these estimates, the individual component-to-component alignment errors are estimated to be 10 ppm. Misalignment of the tool extension in the chuck and through the shaft in the aerostatic spindle is the largest contributing factor to the error. The further the Z-axis (D_8 increases) of the spindle is extended, the larger the error. With the Z-axis retracted and the axes centered, the predicted accuracy is 8 microns. With all the axes at the limit of their travel, the predicted accuracy is 9 microns. By mapping of the axes' errors, a factor of 10 improvement is expected because there are only preloaded rolling element joints in the machine. A setting tool station can also be used to reduce all offsets [20].

Table 1: Work path error for retracted and extended tool. The relative dimensions of each coordinate system are given along with its random errors. Random errors are predicted to be 10 ppm of length of component.

Retracted	**Part-to-Fixture** (D_5)		**Fixture to Disc** (D_4)		**Disc to Shaft** (D_3)	
Axes	Dimensions (mm)	Random Errors (μm)	Dimensions (mm)	Random Errors (μm)	Dimensions (mm)	Random Errors (μm)
X	**0.0**	**0.25**	**0.0**	**0.13**	**0.0**	**0.32**
Y	**0.0**	**0.25**	**0.0**	**0.13**	**0.0**	**0.32**
Z	**-25.4**	**0.25**	**-12.7**	**0.13**	**-12.7**	**0.32**
θX (rad)	**0.0**	**1.0E-5**	**0.0**	**1.0E-5**	**0.0**	**1.0E-5**
θY (rad)	**0.0**	**1.0E-5**	**0.0**	**1.0E-5**	**0.0**	**1.0E-5**
θZ (rad)	**0.0**	**1.0E-5**	**0.0**	**1.0E-5**	**0.0**	**1.0E-5**

Retracted	**Shaft to Bearing** (D_2)		**Bearing to Reference** (D_1)	
Axes	Dimensions (mm)	Random Errors (μm)	Dimensions (mm)	Random Errors (μm)
X	**0.0**	**1.68**	**-240.0**	**2.4**
Y	**0.0**	**1.68**	**0.0**	**2.4**
Z	**-125.7**	**1.68**	**0.0**	**2.4**
θX (rad)	**0.0**	**1.0E-5**	**0.0**	**1.0E-5**
θY (rad)	**0.0**	**1.0E-5**	**0.0**	**1.0E-5**
θZ (rad)	**0.0**	**1.0E-5**	**0.0**	**1.0E-5**

Sum Random Errors in the reference CS		RSS Random Errors in the reference CS		Average SUM & RSS random errors in the reference CS	
δX (μm) =	**7.7**	δX (μm) =	**4.8**	δX (μm) =	**6.2**
δY (μm) =	**7.7**	δY (μm) =	**4.8**	δY (μm) =	**6.2**
δZ (μm) =	**4.8**	δZ (μm) =	**2.9**	δZ (μm) =	**3.9**
εX (rad) =	**50.0**	εX (rad) =	**22.4**	εX (rad) =	**36.2**
εY (rad) =	**50.0**	εY (rad) =	**22.4**	εY (rad) =	**36.2**
εZ (rad) =	**50.0**	εZ (rad) =	**22.4**	εZ (rad) =	**36.2**

Extended	Part-to-fixture (D_5)		Fixture to Disc (D_4)		Disc to Shaft (D_3)	
Axes	Dimensions (mm)	Random Errors (μm)	Dimensions (mm)	Random Errors (μm)	Dimensions (mm)	Random Errors (μm)
X	**0.0**	**0.25**	**0.0**	**0.13**	**0.0**	**0.32**
Y	**0.0**	**0.25**	**0.0**	**0.13**	**0.0**	**0.32**
Z	**-25.4**	**0.25**	**-12.7**	**0.13**	**-12.7**	**0.32**
θX (rad)	**0.0**	**1.0E-5**	**0.0**	**1.0E-5**	**0.0**	**1.0E-5**
θY (rad)	**0.0**	**1.0E-5**	**0.0**	**1.0E-5**	**0.0**	**1.0E-5**
θZ (rad)	**0.0**	**1.0E-5**	**0.0**	**1.0E-5**	**0.0**	**1.0E-5**

Extended	Shaft to Bearing (D_2)		Bearing to Reference (D_1)	
Axes	Dimensions (mm)	Random Errors (μm)	Dimensions (mm)	Random Errors (μm)
X	**0.0**	**1.68**	**-240.0**	**2.4**
Y	**0.0**	**1.68**	**0.0**	**2.4**
Z	**-176.5**	**1.68**	**0.0**	**2.4**
θX (rad)	**0.0**	**1.0E-5**	**0.0**	**1.0E-5**
θY (rad)	**0.0**	**1.0E-5**	**0.0**	**1.0E-5**
θZ (rad)	**0.0**	**1.0E-5**	**0.0**	**1.0E-5**

Sum Random Errors in the reference CS		RSS Random Errors in the reference CS		Average SUM & RSS random errors in the reference CS	
δX (μm) =	**8.4**	δX (μm) =	**5.2**	δX (μm) =	**6.8**
δY (μm) =	**8.4**	δY (μm) =	**5.2**	δY (μm) =	**6.8**
δZ (μm) =	**4.9**	δZ (μm) =	**2.9**	δZ (μm) =	**3.9**
εX (rad) =	**50.0**	εX (rad) =	**22.4**	εX (rad) =	**36.2**
εY (rad) =	**50.0**	εY (rad) =	**22.4**	εY (rad) =	**36.2**
εZ (rad) =	**50.0**	εZ (rad) =	**22.4**	εZ (rad) =	**36.2**

Table 2: Tool path error for tool retracted and extended. The relative dimensions of each coordinate system are given along with its random errors. Each random error is estimated to be 10 ppm of component length.

Retracted	**Tool tip to Collet** (D_6)		**Collet to Shaft** (D_7)		**Shaft to Bearing** (D_8)	
Axes	Dimensions (mm)	Random Errors (μm)	Dimensions (mm)	Random Errors (μm)	Dimensions (mm)	Random Errors (μm)
X	**0.0**	**0.1**	**0.0**	**2.5E-3**	**0.0**	**2.5E-3**
Y	**0.0**	**0.1**	**0.0**	**2.5E-3**	**0.0**	**2.5E-3**
Z	**-44.4**	**0.0**	**-60.2**	**0.0**	**12.7**	**0.0**
θX (rad)	**0.0**	**1.0E-5**	**0.0**	**1.0E-5**	**0.0**	**1.0E-5**
θY (rad)	**0.0**	**1.0E-5**	**0.0**	**1.0E-5**	**0.0**	**1.0E-5**
θZ (rad)	**0.0**	**1.0E-5**	**0.0**	**1.0E-5**	**0.0**	**1.0E-5**
Retracted	**Bearings to holder** (D_9)		**Holder to Shaft** (D_{10})		**Shaft to Bearings** (D_{11})	
Axes	Dimensions (mm)	Random Errors (μm)	Dimensions (mm)	Random Errors (μm)	Dimensions (mm)	Random Errors (μm)
X	**0.0**	**0.9**	**50.8**	**0.25**	**189.2**	**189.2**
Y	**0.0**	**0.9**	**0.0**	**0.25**	**0.0**	**0.0**
Z	**-39.5**	**0.0**	**-131.4**	**0.25**	**0.0**	**0.0**
θX (rad)	**0.0**	**1.0E-6**	**0.0**	**1.0E-5**	**0.0**	**0.0**
θY (rad)	**0.0**	**1.0E-6**	**0.0**	**1.0E-5**	**0.0**	**0.0**
θZ (rad)	**0.0**	**1.0E-6**	**0.0**	**1.0E-5**	**0.0**	**0.0**

Retracted	**Bearings to Reference** (D_{12})	
Axes	Dimensions (mm)	Random Errors (μm)
X	**0.0**	**2.7**
Y	**0.0**	**2.7**
Z	**227.4**	**2.7**
θX (rad)	**0.0**	**1.0E-5**
θY (rad)	**0.0**	**1.0E-5**
θZ (rad)	**0.0**	**1.0E-5**

Sum Random Errors in the reference CS		RSS Random Errors in the reference CS		Average SUM & RSS random errors in the reference CS	
δX (μm) =	**8.1**	δX (μm) =	**3.6**	δX (μm) =	**5.8**
δY (μm) =	**11.0**	δY (μm) =	**5.6**	δY (μm) =	**8.3**
δZ (μm) =	**7.1**	δZ (μm) =	**5.2**	δZ (μm) =	**6.1**
εX (rad) =	**60.1**	εX (rad) =	**24.5**	εX (rad) =	**42.7**
εY (rad) =	**60.1**	εY (rad) =	**24.5**	εY (rad) =	**42.7**
εZ (rad) =	**60.1**	εZ (rad) =	**24.5**	εZ (rad) =	**42.7**

Extended	Tool tip to Collet (D_6)		Collet to Shaft (D_7)		Shaft to Bearing (D_8)	
Axes	Dimensions (mm)	Random Errors (μm)	Dimensions (mm)	Random Errors (μm)	Dimensions (mm)	Random Errors (μm)
X	**0.0**	**0.1**	**0.0**	**2.5E-3**	**0.0**	**2.5E-3**
Y	**0.0**	**0.1**	**0.0**	**2.5E-3**	**0.0**	**2.5E-3**
Z	**-44.4**	**0.0**	**-60.2**	**0.0**	**12.7**	**0.0**
θX (rad)	**0.0**	**1.0E-5**	**0.0**	**1.0E-5**	**0.0**	**1.0E-5**
θY (rad)	**0.0**	**1.0E-5**	**0.0**	**1.0E-5**	**0.0**	**1.0E-5**
θZ (rad)	**0.0**	**1.0E-5**	**0.0**	**1.0E-5**	**0.0**	**1.0E-5**
Extended	**Bearings to holder** (D_9)		**Holder to Shaft** (D_{10})		**Shaft to Bearings** (D_{11})	
Axes	Dimensions (mm)	Random Errors (μm)	Dimensions (mm)	Random Errors (μm)	Dimensions (mm)	Random Errors (μm)
X	**0.0**	**0.9**	**50.8**	**0.25**	**189.2**	**1.68**
Y	**0.0**	**0.9**	**0.0**	**0.25**	**0.0**	**1.68**
Z	**-64.9**	**0.0**	**-131.4**	**0.25**	**0.0**	**1.68**
θX (rad)	**0.0**	**1.0E-6**	**0.0**	**1.0E-5**	**0.0**	**1.0E-5**
θY (rad)	**0.0**	**1.0E-6**	**0.0**	**1.0E-5**	**0.0**	**1.0E-5**
θZ (rad)	**0.0**	**1.0E-6**	**0.0**	**1.0E-5**	**0.0**	**1.0E-5**

Extended	Bearings to Reference (D_{12})	
Axes	Dimensions (mm)	Random Errors (μm)
X	**0.0**	**2.7**
Y	**0.0**	**2.7**
Z	**227.4**	**2.7**
θX (rad)	**0.0**	**1.0E-5**
θY (rad)	**0.0**	**1.0E-5**
θZ (rad)	**0.0**	**1.0E-5**

Sum Random Errors in the reference CS		RSS Random Errors in the reference CS		Average SUM & RSS random errors in the reference CS	
δX (μm) =	**9.7**	δX (μm) =	**4.3**	δX (μm) =	**7.0**
δY (μm) =	**12.6**	δY (μm) =	**6.4**	δY (μm) =	**9.5**
δZ (μm) =	**7.1**	δZ (μm) =	**5.2**	δZ (μm) =	**6.1**
εX (rad) =	**60.1**	εX (rad) =	**24.5**	εX (rad) =	**42.7**
εY (rad) =	**60.1**	εY (rad) =	**24.5**	εY (rad) =	**42.7**
εZ (rad) =	**60.1**	εZ (rad) =	**24.5**	εZ (rad) =	**42.7**

The largest estimated random error is 2.7 microns from the bearings to the reference base due to the distance from the axis to the center of the bearings. This is the same reasoning for the work path error for a value of 2.4 microns.

As seen from Table 2, the major two errors are from the bearing to reference and the tip of the tool to the collet. In order to reduce these errors the structural loop would have to be decreased. Minimal amount of the tool shank should be exposed out of the collet. As for the bearing to reference, the retracted position would be most beneficial to cut at. No design alteration at this point for the distance between the bearings to the reference can be made.

Now if the spindle is moved in the y-direction, Table 3 and Table 4 are produced, note the work path can not change in the y direction, only the tool path can. These tables show that the error is the same but the movement has changed from the z-axis to the y-axis.

Table 3: Work path with movement in x and y directions. No movement in y can be performed within the work path. Note the random error values and dimensions of the coordinate systems are in Appendix B. Each random error is estimated to be 10 ppm of length of component.

Sum Random Errors in the reference CS		RSS Random Errors in the reference CS		Average SUM & RSS random errors in the reference CS	
δX (μm) =	7.9	δX (μm) =	4.7	δX (μm) =	6.3
δY (μm) =	7.8	δY (μm) =	4.7	δY (μm) =	6.3
δZ (μm) =	4.9	δZ (μm) =	2.9	δZ (μm) =	3.9
εX (rad) =	50.0	εX (rad) =	22.3	εX (rad) =	36.2
εY (rad) =	50.0	εY (rad) =	22.3	εY (rad) =	36.2
εZ (rad) =	50.0	εZ (rad) =	22.3	εZ (rad) =	36.2

Table 4: Tool path with movement in the x and y directions. Note the random error values and dimensions of the coordinate systems are in Appendix B. Each random error is estimated to be 10 ppm of length of component.

Sum Random Errors in the reference CS		RSS Random Errors in the reference CS		Average SUM & RSS random errors in the reference CS	
δX (μm) =	8.1	δX (μm) =	3.6	δX (μm) =	5.8
δY (μm) =	8.1	δY (μm) =	5.2	δY (μm) =	6.7
δZ (μm) =	10.0	δZ (μm) =	5.5	δZ (μm) =	7.8
εX (rad) =	61.0	εX (rad) =	24.5	εX (rad) =	42.8
εY (rad) =	61.0	εY (rad) =	24.5	εY (rad) =	42.8
εZ (rad) =	61.0	εZ (rad) =	24.5	εZ (rad) =	42.8

The error for the tool and work path for the above case is 7 microns. Note the largest errors are in the δY direction for the tool path and δY and δX direction for the work path. Thus the errors are better handled with the movement in the X and Y direction and should be used while machining.

Now with movement in the y and z directions, Table 5 shows the new configuration and errors. The work path has the same values as Table 3.

Table 5: Tool path movement in the x, y, and z axes. Work path is same case as previous. Note the random error values and dimensions of the coordinate systems are in Appendix B. Each random error is estimated to be 10 ppm of length of component.

Sum Random Errors in the reference CS		RSS Random Errors in the reference CS		Average SUM & RSS random errors in the reference CS	
δX (μm) =	10.7	δX (μm) =	5.2	δX (μm) =	7.9
δY (μm) =	10.0	δY (μm) =	6.5	δY (μm) =	8.20
δZ (μm) =	10.8	δZ (μm) =	6.0	δZ (μm) =	8.4
εX (rad) =	61.0	εX (rad) =	24.5	εX (rad) =	42.8
εY (rad) =	61.0	εY (rad) =	24.5	εY (rad) =	42.8
εZ (rad) =	61.0	εZ (rad) =	24.5	εZ (rad) =	42.8

The tool path error is 8 microns and the largest occurs in the δY direction. Again as stated above, a factor of 5-10 times improvement of the axes' errors is expected because there are only preloaded rolling element joints in the machine.

The above tables show the machine's accuracy is determined by two important distances, bearings to reference point and tool tip to collet. These can be reduced by machining in the x and y directions and keeping the distance small.

4.2 Tool Stiffness

The stiffness of the tool was used in the error analysis calculation to determine how much the tool bit would deflect given the cutting force. To calculate the stiffness of a standard tool requires knowing the elastic modulus, diameter, and length of the tool. The deflection for a tool, which is in any standard strength of materials book [21], is

$$\delta = \frac{PL^3}{3EI} \tag{1}$$

Rearranging the above equation to give the stiffness K:

$$K = \frac{P}{\delta} = \frac{3EI}{L^3}$$

The polar moment if inertia I is

$$I_p = \frac{\pi d^4}{32} \tag{2}$$

and substituting this into the equation for stiffness gives the strength of the tool in terms of modulus of elasticity, diameter of the bit, and the length of the tool:

$$K = \frac{3\pi d^4}{32L^3}$$

(3)

Since a tool bit has two diameters, D_1 for the shaft portion and d_2 for the cutting portion, the stiffness of each section is calculated and then added like springs in series to give the over all stiffness of

$$\frac{1}{K_{tot}} = \frac{1}{K_{D1}} + \frac{1}{K_{d2}}$$

(4)

Assuming the tool is steel makes the modulus of elasticity 2.1 N/mm^2 and taking a standard tool of D_1 3.175 mm with length of 12 mm and d_2 0.5 mm with length of 0.5 mm makes the stiffness 3254 N/mm

4.3 Beam Bending

The principal moving structural elements are the ball-screw splines, and originally it was thought that the ball-screw splines could project through air bearing sleeves in order to provide a greater degree of accuracy and dynamic stiffness, refer to Figure 10. In the next subsection and in Chapter 6 it is shown this is not the case. The grooved portion of the shaft could be of a smaller diameter than the portion through the air bearings, and hence radial error motions induced by the nuts could be reduced. Figure 18 shows the model of this concept [22]. It is found, as the length of c and d increase, the deflection ratio between the work piece end (x = 0) and the nut end (x = c + d) decrease for a given radial deflection at the nut; however, the size of the machine grows in proportion to its workspace. This poses the question, how much "self coupling" is desired verses buying more accurate components in the first place?.

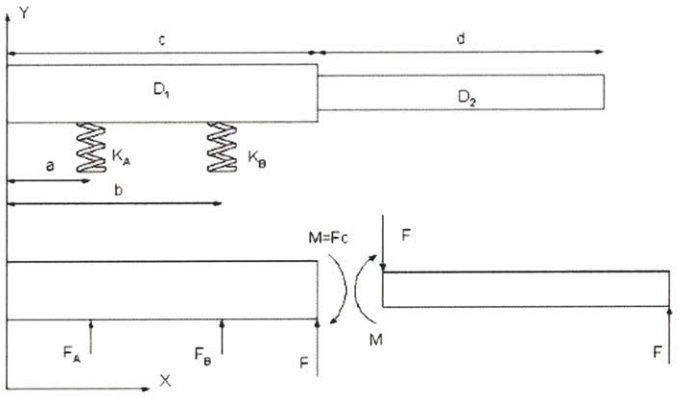

Figure 18: Stepped shaft model of the ball-screw spline supported at its front end by air bearings, where radial displacement from the nut closest to the air bearings is applied to the end of shaft segment D_2.

However, adding length to the shaft to enable it to be supported by the air bearings makes the machine very large with respect to its work volume; hence an important part of the tests are to determine if they are really even needed. Thus the initial test machine does

not use the air bearings to help support the shaft; it only uses the screw and ballspline nuts. This is one of the fundamental principals in deciding to use the nuts on the ball-screw spline to support the shaft because it is compact and no additional component are needed to increase the accuracy. The next section describes the beam theory for two types of beams, a constant diameter and a variable diameter shaft. Then the proper sizing of the shaft is presented for each case.

4.3.1 Beam theory background

The ball screw-spline with two air bearings supporting the far end of the shaft can be represented as a beam with two springs. Figure 19 describes what the system should look like.

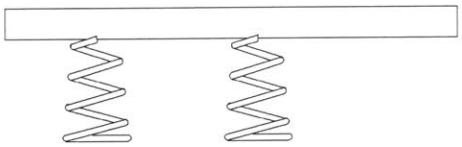

Figure 19: Shaft diameter shaft with 2 air bearings

When a force is applied between the center of the ball screw-spline nut, it is necessary to determine the deflection in the beam, namely at the opposite end of where the force is applied, Figure 20 .

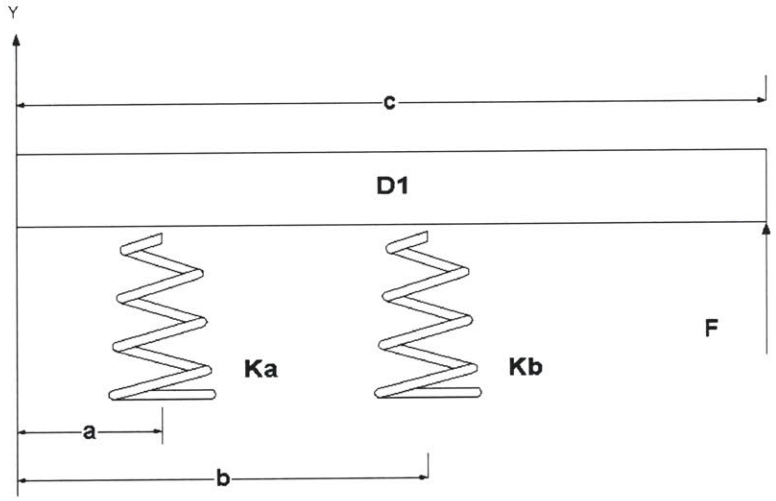

Figure 20: Forces on a beam.

Assuming the beam has constant flexural rigidity, EI where E is the modulus of elasticity and I is the moment of inertia, the deflection of the beam can be determined. If the beam did not have constant flexural rigidity, EI would be a function of x (See the section on variable cross section below.) Thus by assuming constant flexural rigidity, the

calculation is more desirable. To determine the deflection of the beam, the equation for the elastic curve is found. The equations to obtain the elastic curve are:

$$EI\frac{d^4y}{dx^4} = -q(x) \tag{5}$$

$$EI\frac{d^3y}{dx^3} = V(x) = -\int q(x)dx + C_1 \tag{6}$$

$$EI\frac{d^2y}{dx^2} = M(x) = -\int dx \int q(x)dx + C_1x + C_2 \tag{7}$$

$$EI\frac{d^1y}{dx^1} = EI\theta(x) = -\int dx \int dx \int q(x)dx + \frac{1}{2}C_1x^2 + C_2x + C_3 \tag{8}$$

$$EIy(x) = -\int dx \int dx \int dx \int q(x)dx + \frac{1}{6}C_1x^3 + \frac{1}{2}C_2x^2 + C_3x + C_4 \tag{9}$$

These equations are derived in any mechanics of materials book [21]. Noticing four constants of integration, these values can be obtained from the boundary conditions of the system. The boundary conditions of the beam/spring system are:

$$V(0) = 0 \tag{10}$$

$$M(0) = 0 \tag{11}$$

$$y(a) = \delta_1 \tag{12}$$

$$y(b) = \delta_2 \tag{13}$$

The first two conditions are obtained from the shear and moment forces at the ends of the beam. Since there are no shear or bending moment at the ends, the values are 0. The last two conditions are obtained from the beam supports. The value of deflection or the value of y at the supports is equal to the amount of deformation that the individual supports go through. Since they are modeled as springs, the deflection is $\delta = F/K$.

To determine *q(x)*, the concept of singularity functions will be used. Singularity functions have the form

$$f_n(x) = \langle x - a \rangle^n \tag{14}$$

This is valid for n≥0. For 0≥n f_n becomes 0 because the expression in the brackets is negative. If the expression is positive, then the value of f_n is $(x-a)^n$. Notice the brackets changed to parentheses or ordinary brackets when the quantity inside is positive. Likely when 0≥n, f_n is 0 no matter what the value is in the brackets. The singularity function has the following integration law

$$\int_{-\infty}^{x} \langle x - a \rangle^n dx = \frac{\langle x - a \rangle^{n+1}}{n+1} \qquad \text{where } n \geq 0 \tag{15}$$

The value of n represents the different loading types. For example when n = -2, this represents a unit concentrated moment. Similarly when n = -1,0,1, this represents a unit concentrated load, unit step, and unit ramp respectfully. The loads on the system presented in Figure 20, which are the air bearings, are represented as concentrated loads.

Lastly for cases of n= -2 and -1, the values are 0 everywhere except at x=a. At that point they are infinite. They are included in the calculations but n is written as a subscript instead of a superscript because in (15) n≥0. Upon integration, they become $\langle x-a \rangle_{-2} = \langle x-a \rangle_{-1}$ and $\langle x-a \rangle_{-1} = \langle x-a \rangle^0$.

4.3.2 Beam Analysis – Constant shaft deflection

Drawing a free body diagram of the beam represented in Figure 20:

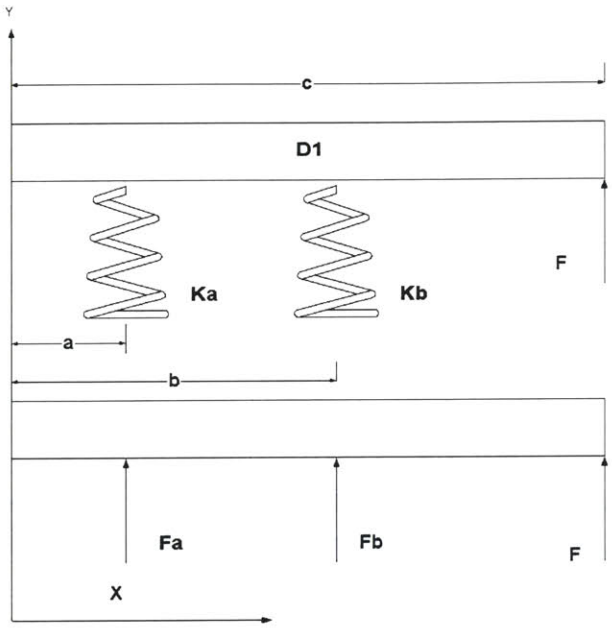

Figure 21: Free body diagram of a constant diameter beam.

Summing the forces in the y direction with up as positive and assuming the forces are all pointing up for ease of calculation, gives the following equation

$$\sum F_y = 0 = F_A + F_B + F \tag{16}$$

Solving for F_B:

$$F_B = -F - F_A \tag{17}$$

Summing the moments around the spring B:

$$\sum M_B = 0 = -(b-a)F_A + (c-b)F \tag{18}$$

Solving for F_A results in

$$F_A = F\frac{c-b}{b-a} \tag{19}$$

Notice how the value of the angle was not needed because it cancels out. To get the value of F_B in terms of F, sub (19) into (17) to get

$$F_B = -F\left(\frac{c-b}{b-a}\right) - F$$

(20)

Factoring out F, F_B becomes

$$F_B = -F\left(\frac{c-a}{b-a}\right)$$

(21)

Elastic Equation

Since the reaction forces are found, the load is determined next. There are two concentrated loads on the beam, F_A and F_B. Using singularity functions and starting the cut from the left-hand side (Figure 21), the load equation can be represented as:

$$q(x) = F_A\langle x-a\rangle_{-1} + F_B\langle x-b\rangle_{-1} + F\langle x-c\rangle_{-1}$$

(22)

Substituting (22) into (6) gives the shear for V(x):

$$V(x) = -\left(F_A\langle x-a\rangle^0 + F_B\langle x-b\rangle^0 + F\langle x_1-c)\rangle^0 + C_1\right)$$

(23)

Notice how the power on the singularity function increased by one because of integration. To find the constant C_1, the boundary condition given by (10) will be used. Subbing in 0 for x and 0 for V(x) gives:

$$C_1 = 0$$

$$C_1 = 0 \qquad (24)$$

The terms in the brackets are negative, so according to the singularity function they are 0. Also one can not have a negative length. Thus the constant of integration drops out and the shear equation becomes

$$V(x) = -(F_A\langle x-a\rangle^0 + F_B\langle x-b\rangle^0 + F\langle x-c\rangle^0)$$

(25)

Integrating (25) to find the bending moment equation, which is done by substituting (25) into (7) reveals:

$$M(x) = F_A\langle x-a\rangle^1 + F_B\langle x-b\rangle^1 + F\langle x-c\rangle^1 + C_2$$

(26)

But the boundary condition given by (11) states there is no bending moment at the end where x is equal to zero. Plugging in these values produces C_2 equal to 0 and (26) becomes

$$M(x) = F_A\langle x-a\rangle^1 + F_B\langle x-b\rangle^1 + F\langle x-c\rangle^1$$

(27)

which is the bending moment equation. The slope of the beam is determined next by substituting (27) into (8):

$$EI\theta(x) = \frac{F_A}{2}\langle x-a\rangle^2 + \frac{F_B}{2}\langle x-b\rangle^2 + \frac{F}{2}\langle x-c\rangle^2 + C_3$$

(28)

Leaving C_3 in the equation and integrating once more to obtain the equation for deflection:

$$EI\delta(x) = \frac{F_A}{6}\langle x-a\rangle^3 + \frac{F_B}{6}\langle x-b\rangle^3 + \frac{F}{6}\langle x-c\rangle^3 + C_3x + C_4$$

(29)

To solve for the two constants C_3 and C_4, we know the deflection at the two supports A and B. That is, the deflection is equal to the force divided by the spring's stiffness. This is boundary condition (12) and (13). Substituting (12) into (29)

$$EI(-\frac{F_A}{K_A}) = \frac{F_A}{6}\langle a-a\rangle^3 + \frac{F_B}{6}\langle a-b\rangle^3 + \frac{F}{6}\langle a-c\rangle^3 + C_3a + C_4$$

(30)

The first term after the equal sign is 0 because the lengths are the same. For the second term, it is 0 also because the value inside the brackets is negative. From the definition of singularity function described above, a negative value is not recognized so the value is 0. The third term is 0 as well because the value of a-c is negative; the value of a cannot be greater than c. Thus, due to the same reasons for the third term, $\langle a\text{-}c\rangle^2$ is 0. Reducing (30) and solving for C_4

$$C_4 = -\left(EI\left(\frac{F_A}{K_A}\right) + C_3a\right)$$

(31)

Going back to (29) and inserting the last boundary condition known, (13), the following equation is obtained

$$EI(-\frac{F_B}{K_B}) = \frac{F_A}{6}\langle b-a\rangle^3 + \frac{F_B}{6}\langle b-b\rangle^3 + \frac{F}{6}\langle b-c\rangle^3 + C_3 b + C_4 \tag{32}$$

The second, third, and fourth terms are 0; lengths cancel out and have negative value in the brackets, respectfully. Angle brackets can be removed and replaced by parentheses because the value of *b-a* is never negative. The first term is not 0 because the value is positive. Substituting (31) into (32) produces

$$EI\left(-\frac{F_B}{K_B}\right) = \frac{F_A}{6}(b-a)^3 + C_3(b) - EI\left(\frac{F_A}{K_A}\right) - C_3 a \tag{33}$$

C_3 can be determined by collecting similar terms and dividing by *b-a*. That is

$$C_3 = \frac{1}{b-a}[EI\left(\frac{F_A}{K_A} - \frac{F_B}{K_B}\right) - \frac{F_A}{6}(b-a)^3] \tag{34}$$

F_1 and F_2 are known from (19) and (20). Thus C_3 is

$$C_3 = \frac{1}{b-a}\left[EI\left(\frac{F}{K_A}\frac{c-b}{b-a} + \frac{F}{K_B}\frac{c-a}{b-a}\right) - \frac{F}{6}\frac{c-b}{b-a}(b-a)^3\right] \tag{35}$$

Factoring out F and EI, (35) from above:

$$C_3 = \frac{FEI}{b-a}\left[\frac{1}{K_A}\frac{c-b}{b-a} + \frac{1}{K_B}\frac{c-a}{b-a} - \frac{1}{6EI}\frac{c-b}{b-a}(b-a)^3\right] \tag{36}$$

The values of F_1 and F_2 can be substituted into C_4. This makes (31) become

$$C_4 = EI\left[-\left(\frac{F}{K_A}\frac{c-b}{b-a}\right)\right] - C_3 a \tag{37}$$

Substituting (36) into (37) gives the value of C_4

$$C_4 = EI\left[-\left(\frac{F}{K_A}\frac{c-b}{b-a}\right)\right]-\frac{FEI}{b-a}\left[\frac{1}{K_A}\frac{c-b}{b-a}+\frac{1}{K_B}\frac{c-a}{b-a}-\frac{1}{6EI}\frac{c-b}{b-a}(b-a)^3\right]a \tag{38}$$

Factoring out *F*, *EI*, and a negative sign produces the following

$$C_4 = FEI\left[-\left(\frac{1}{K_A}\frac{c-b}{b-a}+\frac{a}{b-a}\left[\frac{1}{K_A}\frac{c-b}{b-a}+\frac{1}{K_B}\frac{c-a}{b-a}-\frac{1}{6EI}\frac{c-b}{b-a}(b-a)^3\right]\right)\right] \tag{39}$$

The value of δ(x) can now be determined because the constants are known. Substituting (19), (21), (36), and (39) into (29):

$$\begin{aligned} EI\delta(x) = {} & \frac{F}{6}\frac{c-b}{b-a}\langle x-a\rangle^3-\frac{F}{6}\frac{c-a}{b-a}\langle x-b\rangle^3+\frac{F}{6}\langle x-c\rangle^3+ \\ & \left(\frac{FEI}{b-a}\left[\frac{1}{K_A}\frac{c-b}{b-a}+\frac{1}{K_B}\frac{c-a}{b-a}-\frac{1}{6EI}\frac{c-b}{b-a}(b-a)^3\right]\right)x+ \\ & FEI\left[-\left(\frac{1}{K_A}\frac{c-b}{b-a}+\frac{a}{b-a}\left[\frac{1}{K_A}\frac{c-b}{b-a}+\frac{1}{K_B}\frac{c-a}{b-a}-\frac{1}{6EI}\frac{c-b}{b-a}(b-a)^3\right]\right)\right] \end{aligned} \tag{40}$$

Factoring out F and dividing by the flexural rigidity, the elastic curve equation becomes

$$\delta(x) = F\left\{\begin{array}{l} \frac{1}{EI}\left(\frac{1}{6}\frac{c-b}{b-a}\langle x-a\rangle^3-\frac{1}{6}\frac{c-a}{b-a}\langle x-b\rangle^3+\frac{1}{6}\langle x-c\rangle^3\right)+ \\ \left(\frac{1}{b-a}\left[\frac{1}{K_A}\frac{c-b}{b-a}+\frac{1}{K_B}\frac{c-a}{b-a}-\frac{1}{6EI}\frac{c-b}{b-a}(b-a)^3\right]\right)x+ \\ \left[-\left(\frac{1}{K_A}\frac{c-b}{b-a}+\frac{a}{b-a}\left[\frac{1}{K_A}\frac{c-b}{b-a}+\frac{1}{K_B}\frac{c-a}{b-a}-\frac{1}{6EI}\frac{c-b}{b-a}(b-a)^3\right]\right)\right] \end{array}\right\} \tag{41}$$

4.3.3 Placement of Components

The goal of the above exercise was to find the proper placement of the ball screw-spline nuts in relation to the air bearings. The point of minimal deflection is desired. To find the correct position of the nuts relative to the air bearings, the ratio of deflection at the force end (when *x=0*) to the deflection at the end of the beam (when *x=c*) is compared against the ratio of the length, *b/a*. The deflection when x equals zero is considered δ(0) and the deflection at the opposite end of the beam is considered δ(c). Taking these values

and plotting them, will result in a graph that portrays how much a deflection or error will result at the end opposite of where the force is applied.

Before the graph is made, the equation for δ(0) and δ(c) is found by plugging in the values described above into (41). The following two equations are obtained:

$$\delta(0) = F\left[-\left(\frac{1}{K_A}\frac{c-b}{b-a} + \frac{a}{b-a}\left[\frac{1}{K_A}\frac{c-b}{b-a} + \frac{1}{K_B}\frac{c-a}{b-a} - \frac{1}{6EI}\frac{c-b}{b-a}(b-a)^3\right]\right)\right] \tag{42}$$

$$\delta(c) = F\left\{\begin{array}{l}\frac{1}{EI}\left(\frac{1}{6}\frac{c-b}{b-a}\langle c-a\rangle^3 - \frac{1}{6}\frac{c-a}{b-a}\langle c-b\rangle^3 + \frac{1}{6}\langle c-c\rangle^3\right) + \\ \left(\frac{1}{b-a}\left[\frac{1}{K_A}\frac{c-b}{b-a} + \frac{1}{K_B}\frac{c-a}{b-a} - \frac{1}{6EI}\frac{c-b}{b-a}(b-a)^3\right]\right)c + \\ \left[-\left(\frac{1}{K_A}\frac{c-b}{b-a} + \frac{a}{b-a}\left[\frac{1}{K_A}\frac{c-b}{b-a} + \frac{1}{K_B}\frac{c-a}{b-a} - \frac{1}{6EI}\frac{c-b}{b-a}(b-a)^3\right]\right)\right]\end{array}\right\} \tag{43}$$

But (43) can be reduced further because c-c is 0. Therefore (43) becomes

$$\delta(c) = F\left\{\begin{array}{l}\frac{1}{EI}\left(\frac{1}{6}\frac{c-b}{b-a}\langle c-a\rangle^3 - \frac{1}{6}\frac{c-a}{b-a}\langle c-b\rangle^3\right) + \\ \left(\frac{1}{b-a}\left[\frac{1}{K_A}\frac{c-b}{b-a} + \frac{1}{K_B}\frac{c-a}{b-a} - \frac{1}{6EI}\frac{c-b}{b-a}(b-a)^3\right]\right)c + \\ \left[-\left(\frac{1}{K_A}\frac{c-b}{b-a} + \frac{a}{b-a}\left[\frac{1}{K_A}\frac{c-b}{b-a} + \frac{1}{K_B}\frac{c-a}{b-a} - \frac{1}{6EI}\frac{c-b}{b-a}(b-a)^3\right]\right)\right]\end{array}\right\} \tag{44}$$

F does not need to be known because it cancels out when the ratio *δ(0)/δ(c)* is taken. The ratio looks like this

$$\delta(c)=\frac{\left[-\left(\frac{1}{K_A}\frac{c-b}{b-a}+\frac{a}{b-a}\left[\frac{1}{K_A}\frac{c-b}{b-a}+\frac{1}{K_B}\frac{c-a}{b-a}-\frac{1}{6EI}\frac{c-b}{b-a}(b-a)^3\right]\right)\right]}{\left\{\begin{array}{l}\frac{1}{EI}\left(\frac{1}{6}\frac{c-b}{b-a}\langle c-a\rangle^3-\frac{1}{6}\frac{c-a}{b-a}\langle c-b\rangle^3\right)+\\ \left(\frac{1}{b-a}\left[\frac{1}{K_A}\frac{c-b}{b-a}+\frac{1}{K_B}\frac{c-a}{b-a}-\frac{1}{6EI}\frac{c-b}{b-a}(b-a)^3\right]\right)c+\\ \left[-\left(\frac{1}{K_A}\frac{c-b}{b-a}+\frac{a}{b-a}\left[\frac{1}{K_A}\frac{c-b}{b-a}+\frac{1}{K_B}\frac{c-a}{b-a}-\frac{1}{6EI}\frac{c-b}{b-a}(b-a)^3\right]\right)\right]\end{array}\right\}} \tag{45}$$

Inputting different values for b and a and comparing $\delta(0)/\delta(c)$ versus b/a, the following graph is obtained

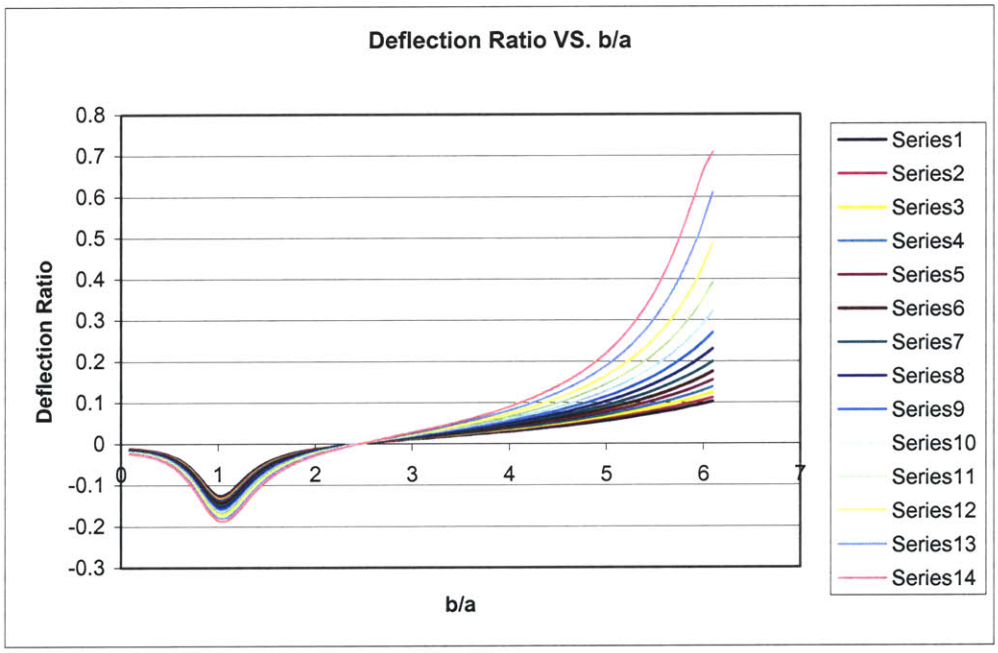

Figure 22: Deflection Ratio for constant shaft

where the value for each number is represented in the following Table.

Table 6: Length values for c and a are in meters

Series	c	a
1	1.14	0.13
2	1.12	0.13
3	1.09	0.13
4	1.07	0.13
5	1.04	0.13
6	1.02	0.13
7	0.99	0.13
8	0.97	0.13
9	0.94	0.13
10	0.91	0.13
11	0.89	0.13
12	0.86	0.13
13	0.84	0.13
14	0.81	0.13

Notice how the graph originally dips down. Then rises through zero and ends in a steep slope. The steep slope is a result of the air bearing being placed past the overall length c. Naturally the equation would go towards infinity if the placement of the bearing were beyond the shaft length. When the bearings are close together, the deflection ratio starts to increase causing one end of the beam to point in one direction while the other end points in the opposite direction. As the distance between the bearings increase, the deflection comes to a point where it levels off and starts to decrease. This represents the bearings obtaining a certain distance that can hold the shaft in a stable position without it tilting. As the graph passes through the x-axis, the two ends of the shaft point in the same direction. This implies there is a point of zero deflection. That is the point, which is most desired.

As a is decreased, the point of zero deflection moves towards the right on the graph. Thus the distance between the air bearings is larger than if a started further in on the shaft. A larger dip in the graph is found when the shaft decreases in length. Figure 23 displays this. Table 7 gives the values of each series.

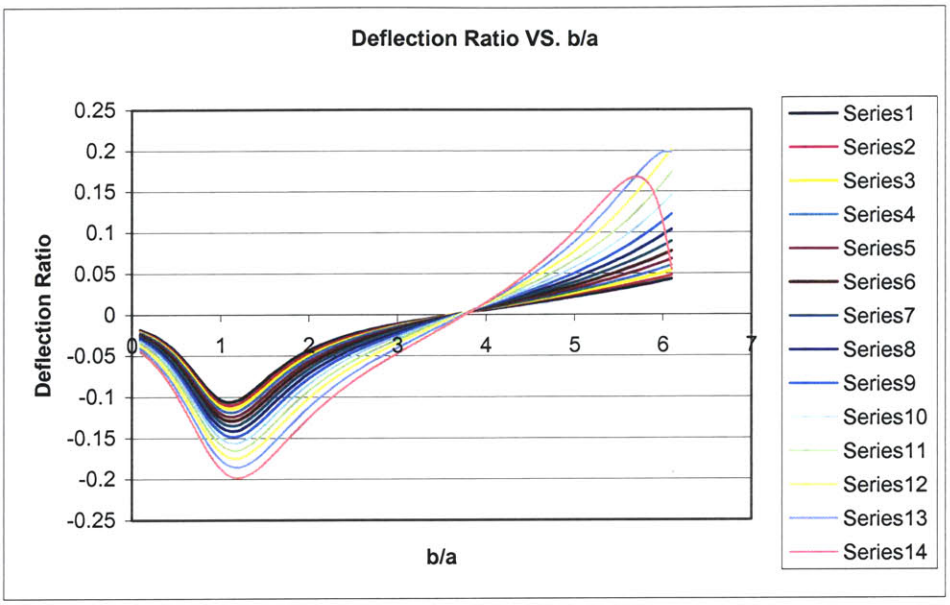

Figure 23: Deflection Ratio for larger c and a

Table 7: Larger values of c and a for deflection figure, units are in meters.

Series	c	a
1	0.81	0.076
2	0.79	0.076
3	0.76	0.076
4	0.74	0.076
5	0.71	0.076
6	0.69	0.076
7	0.66	0.076
8	0.64	0.076
9	0.61	0.076
10	0.58	0.076
11	0.56	0.076
12	0.53	0.076
13	0.51	0.076
14	0.48	0.076

To show how the deflection ratio decreases with the increase of shaft length, Figure 24 was constructed and Table 8 gives the values for each series.

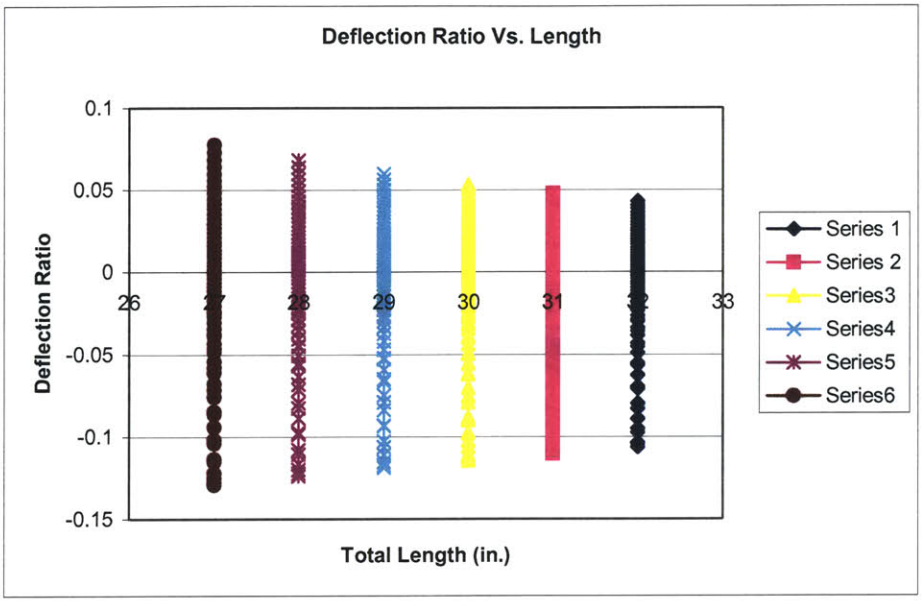

Figure 24: Deflection verses total length of shaft

Table 8: Values for c and a for Figure 24, units are in meters.

Series	c	a
1	0.81	0.076
2	0.79	0.076
3	0.76	0.076
4	0.74	0.076
5	0.71	0.076
6	0.69	0.076

Concluding from these graphs, any length of the shaft can be used because each length crosses the x-axis. What is governing how short the shaft can be is where the first air bearing is placed. Since the air bearing needs to be at least three inches from the tip, the smallest the shaft can be is .38 m with a ratio of 4.3 of b/a. Using this ratio, *a* is placed at .076 m and *b* is at .33 m. According to Abbe's principal, this correlates to his assumption of placing components 3-5 times the shaft diameter away if they are not to have an effect on each other.

A finite element analysis of the constant shaft described above was performed. Figure 25 shows the FEA model. Notice the beam bends at the bearing B (or represented as spring B) and then starts to bend in the opposite direction as the shaft moves to bearing A. The deflection values of the shaft are, the applied force end, 1.1E-5 m, spring B, 3.37E-6 m, spring A, 7.79E-7 m, and at the tip, 3.22E-7 m.

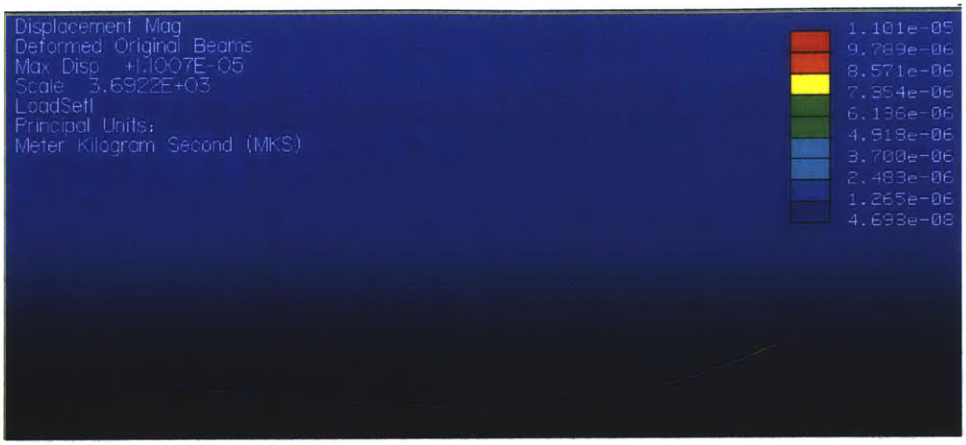

Figure 25: FEA of Constant Shaft.

These above graphs were constructed with a shaft size of 32 mm. The calculations are correct up to the point where the deflection ratio crosses the x-axis. At this point, the FEA shows the ratio to be more of a roundoff error. The effects on deflection as the diameter of the shaft decreases is sought next.

4.3.4 Optimization of Shaft

If the shaft diameter decreases, can the shaft still perform as well as the 32 mm shaft? Decreasing the shaft diameter to standard sizes of 25, 20, 16, 10, and 8 mm, the following graphs were obtained.

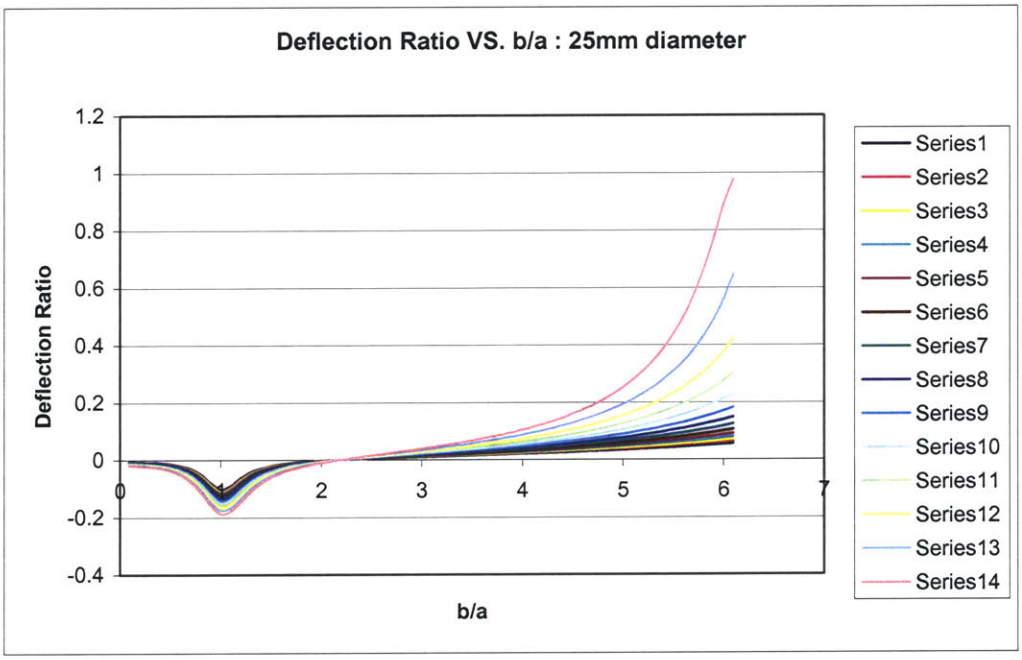

Figure 26: 25 mm shaft diameter

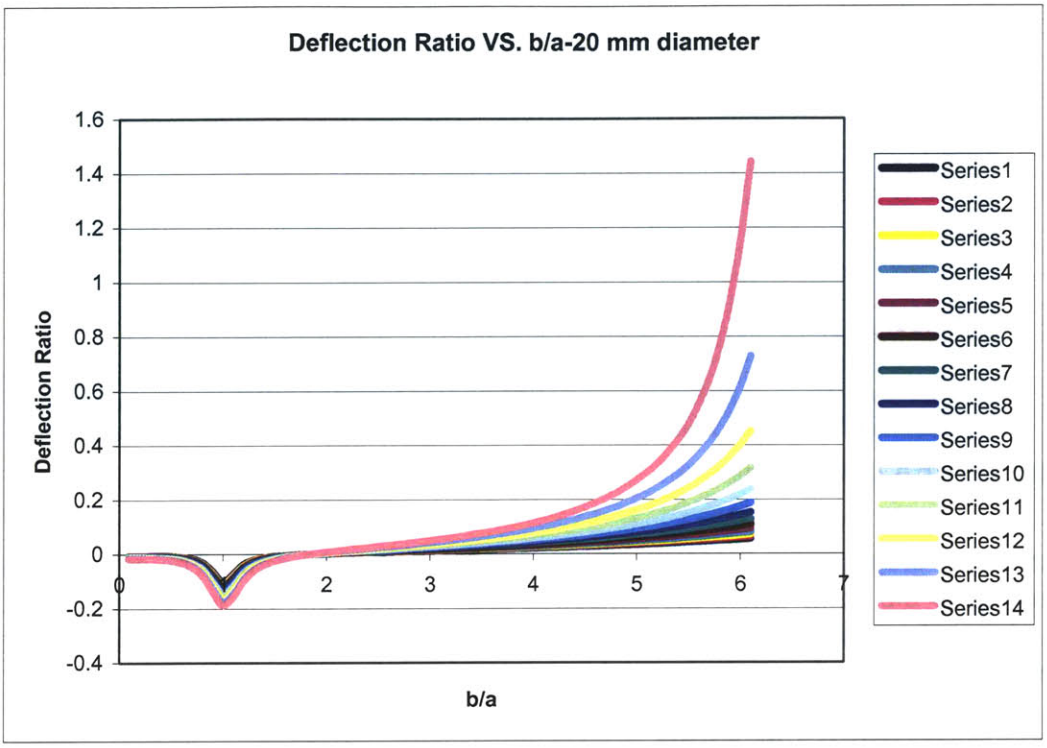

Figure 27: 20 mm shaft diameter

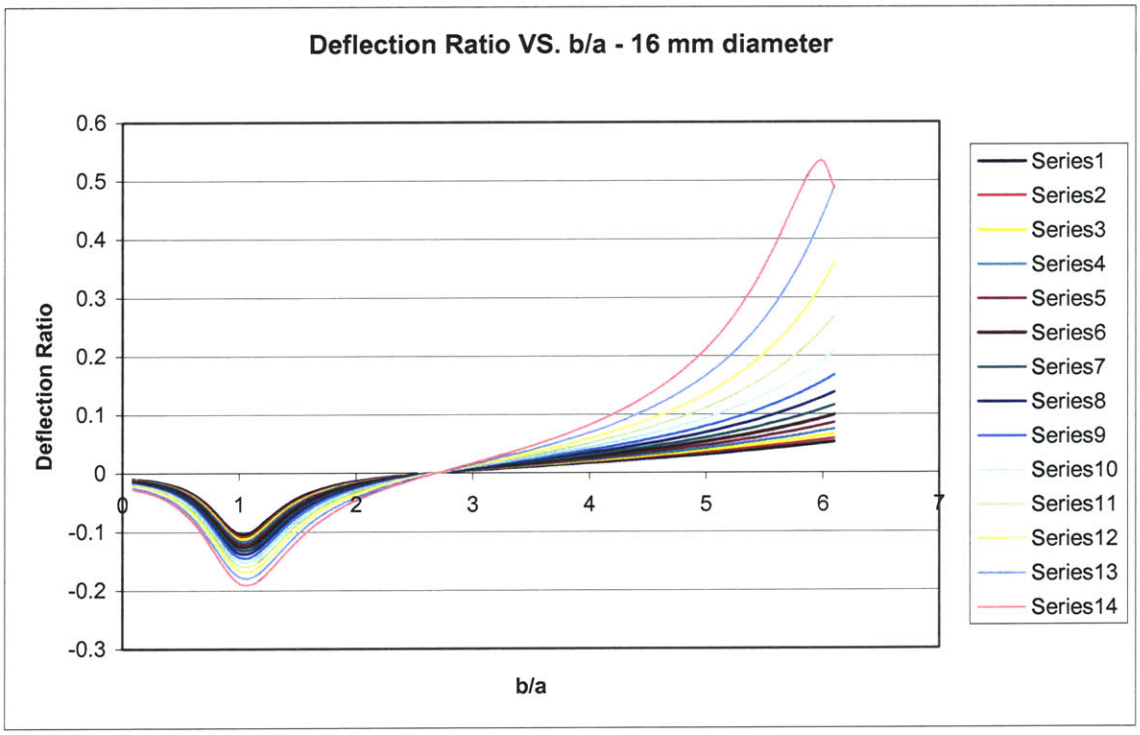

Figure 28: 16 mm shaft diameter

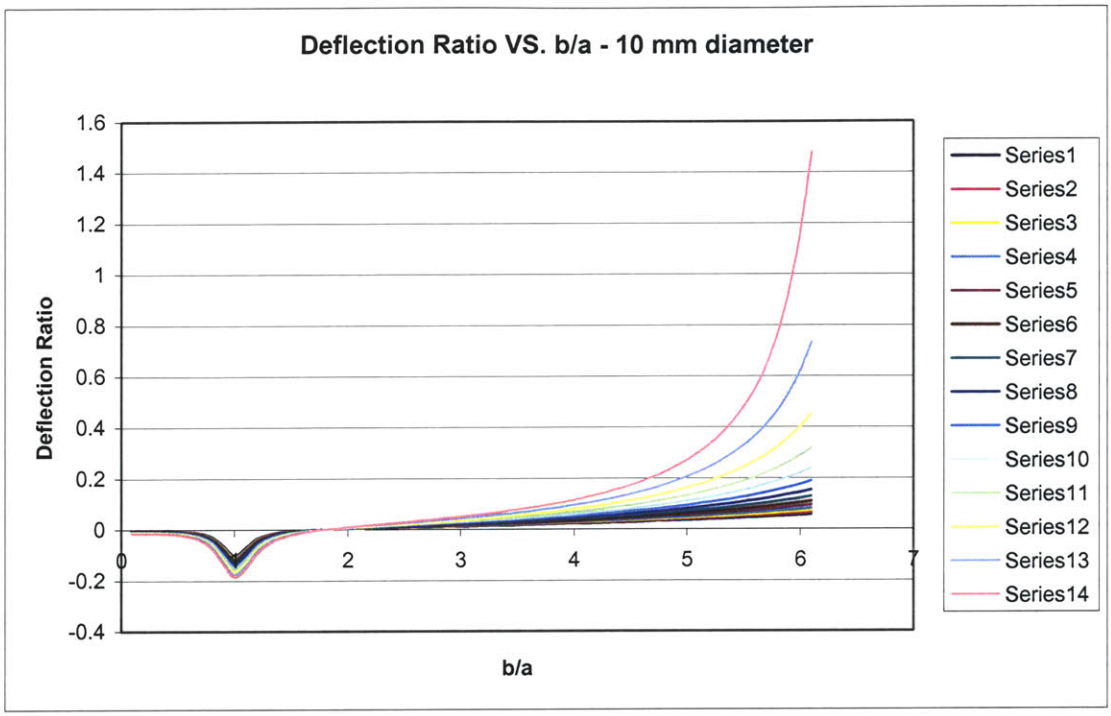

Figure 29: 10 mm shaft diameter

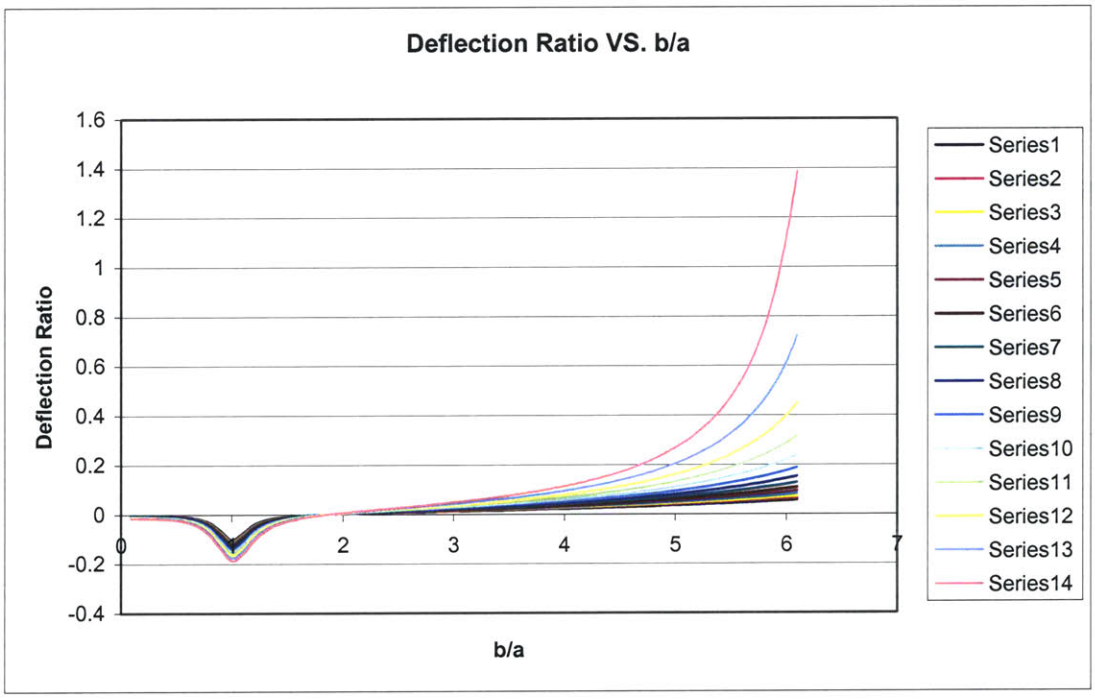

Figure 30: 8 mm shaft diameter

The above five figures used the following table to construct each series.

Table 9: Values for comparison of the five different diameter shafts, units are in meters.

Series	c	a
1	0.81	0.076
2	0.79	0.076
3	0.76	0.076
4	0.74	0.076
5	0.71	0.076
6	0.69	0.076
7	0.66	0.076
8	0.64	0.076
9	0.61	0.076
10	0.58	0.076
11	0.56	0.076
12	0.53	0.076
13	0.51	0.076
14	0.48	0.076

As the diameter of the shaft decreases, the air bearing stiffness decreases as well. This is noticeable in the deflection ratio of the above figures. For an 8 mm shaft diameter, the deflection ratio can become as high as 1.4 where for a 25 mm shaft diameter, the ratio is 1. The figures are similar in that they dip down around a b/a ratio of 1 and cross at the x-axis between 2-3. Thus a smaller diameter would work, but the deflection ratio increases at a faster rate than the 32 mm diameter does.

These calculations display an understanding of how a constant shaft diameter works, but the shaft that models the ballscrew-spline is one of two diameters. The next section investigates this.

4.3.5 Variable shaft diameter

The true shaft will have a sleeve on the opposite end of where the ball screw-spline nuts reside. This will make the shaft have a variable cross section. The representation is presented in Figure 31.

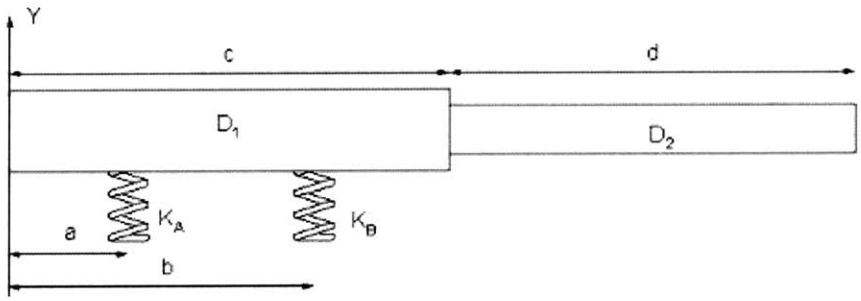

Figure 31: Variable shaft diameter

Splitting the shaft into two sections, one beam with diameter D_1 and a smaller beam with diameter D_2, the overall deflection can be found. It is found by adding the deflection

from the first section with that of the second. Since the slope is continuous through the shaft, both section slopes add. Therefore the over all deflection is

$$\delta_{tot} = \delta_{D\_1} + \delta_{D\_2} + (d)\alpha_{D\_1} \tag{46}$$

The free body diagram is shown in Figure 32.

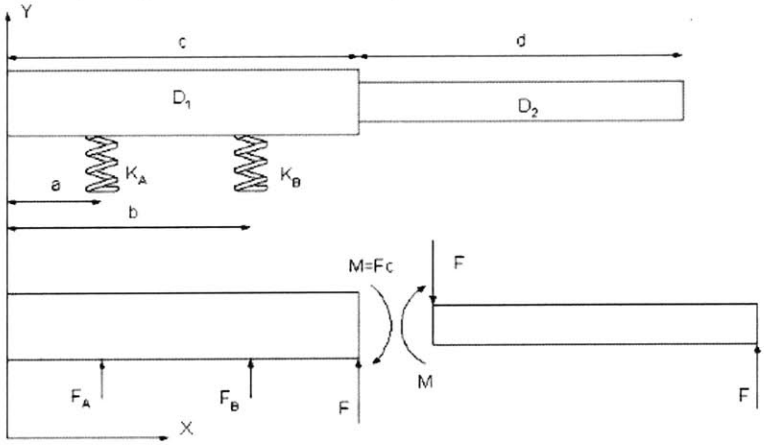

Figure 32: Variable shaft free body diagram

Summing the forces in the y direction with up as positive and assuming the forces are all pointing up for ease of calculation, gives the following equation

$$\sum F_y = 0 = F_A + F_B + F \tag{47}$$

Solving for F_B:

$$F_B = -F - F_A \tag{48}$$

Now summing the moments around the spring B:

$$\sum M_B = 0 = -(b-a)F_A + (c-b+d)F \tag{49}$$

Solving for F_A results in

$$F_A = F\frac{c-b+d}{b-a} \tag{50}$$

Notice how the value of the angle was not needed because it cancels out. To get the value of F_B in terms of F, sub (50) into (48):

$$F_B = -F\left(\frac{c+d-a}{b-a}\right) \tag{51}$$

Summing the moments to find M

$$M = (c-a)F_A + (c-b)F_B \tag{52}$$

Elastic Equation

Since the reaction forces are found, the load is determined next. There are two concentrated loads on the beam, F_A and F_B. Using singularity functions and starting the cut from the lefthand side (Figure 32), the load equation can be represented as:

$$q(x) = F_A\langle x-a\rangle_{-1} + F_B\langle x-b\rangle_{-1} + F\langle x-c\rangle_{-1} + M\langle x-c\rangle_{-2} \tag{53}$$

Substituting (53) into (6) gives the shear for V(x):

$$V(x) = -\left(F_A\langle x-a\rangle^0 + F_B\langle x-b\rangle^0 + F\langle x_1-c)\rangle^0 + M\langle x-c\rangle_{-1} + C_1\right) \tag{54}$$

To find the constant C_1, the boundary condition given by (10) will be used. Subbing in 0 for x and 0 for V(x) produces:

$$C_1 = 0$$

$$C_1 = 0 \tag{55}$$

The terms in the brackets are negative. According to the singularity function they are 0, since one cannot have a negative length. Thus the constant of integration drops out and the shear equation looks like

$$V(x) = -(F_A\langle x-a\rangle^0 + F_B\langle x-b\rangle^0 + F\langle x-c\rangle^0 + M\langle x-c\rangle_{-1}) \tag{56}$$

Integrating (56) to find the bending moment equation, which is done by substituting (56) into (7) reveals:

$$M(x) = F_A\langle x-a\rangle^1 + F_B\langle x-b\rangle^1 + F\langle x-c\rangle^1 + M\langle x-c\rangle^0 + C_2$$

(57)

But the boundary condition given by (11) states there is no bending moment at the end where x is equal to zero. Plugging in these values produces C_2 equal to 0 and (57) becomes

$$M(x) = F_A\langle x-a\rangle^1 + F_B\langle x-b\rangle^1 + F\langle x-c\rangle^1 + M\langle x-c\rangle^0$$

(58)

which is the bending moment equation. The slope of the beam is determined next by substituting (58) into (8):

$$EI\theta(x) = \frac{F_A}{2}\langle x-a\rangle^2 + \frac{F_B}{2}\langle x-b\rangle^2 + \frac{F}{2}\langle x-c\rangle^2 + M\langle x-c\rangle^1 + C_3$$

(59)

Leaving C_3 in the equation and integrating once more to obtain the equation for deflection,

$$EI\delta(x) = \frac{F_A}{6}\langle x-a\rangle^3 + \frac{F_B}{6}\langle x-b\rangle^3 + \frac{F}{6}\langle x-c\rangle^3 + \frac{M}{2}\langle x-c\rangle^2 + C_3x + C_4$$

(60)

To solve for the two constants C_3 and C_4, we know the deflection at the two supports *A* and *B*. That is, the deflection is equal to the force divided by the spring's stiffness. This is boundary condition (12) and (13). Substituting (12) into (60)

$$EI(-\frac{F_A}{K_A}) = \frac{F_A}{6}\langle a-a\rangle^3 + \frac{F_B}{6}\langle a-b\rangle^3 + \frac{F}{6}\langle a-c\rangle^3 + \frac{M}{2}\langle a-c\rangle^2 + C_3a + C_4$$

(61)

The first term after the equal sign is 0 because the lengths are the same. For the second term, it is 0 also because the value inside the brackets, after a cancel out, is negative. From the definition of singularity function described above, a negative value is not recognized so the value is 0. The third term is also 0 because the value of *a-c* is negative; the value of *a* can not be greater than *c*. Thus, due to the same reasons for the third term, $< a\text{-}c>^2$ is 0. Reducing (61) and solving for C_4

$$C_4 = -\left(EI\left(\frac{F_A}{K_A} \right) + C_3 a \right)$$

(62)

Going back to (60) and inserting the last boundary condition known, (13), the following equation is obtained

$$EI(-\frac{F_B}{K_B}) = \frac{F_A}{6}\langle b-a\rangle^3 + \frac{F_B}{6}\langle b-b\rangle^3 + \frac{F}{6}\langle b-c\rangle^3 + \frac{M}{2}(b-c)^2 + C_3 b + C_4$$

(63)

The second, third, and fourth terms are 0. Angle brackets can be removed and replaced by parentheses because the value of *b-a* is never negative. Substituting (62) into (63) produces

$$EI\left(-\frac{F_B}{K_B} \right) = \frac{F_A}{6}(b-a)^3 + C_3(b) - EI\left(\frac{F_A}{K_A} \right) - C_3 a$$

(64)

C_3 can be determined by collecting like terms and dividing by *b-a*. That is

$$C_3 = \frac{1}{b-a}[EI\left(\frac{F_A}{K_A} - \frac{F_B}{K_B} \right) - \frac{F_A}{6}(b-a)^3]$$

(65)

F_1 and F_2 are know from (50) and (51). Thus C_3 is

$$C_3 = \frac{1}{b-a}\left[EI\left(\frac{F}{K_A}\frac{c-b+d}{b-a} + \frac{F}{K_B}\frac{c+d-a}{b-a} \right) - \frac{F}{6}\frac{c-b+d}{b-a}(b-a)^3 \right]$$

(66)

Factoring out *F* and *EI*, (66) becomes

$$C_3 = \frac{FEI}{b-a}\left[\frac{1}{K_A}\frac{c-b+d}{b-a} + \frac{1}{K_B}\frac{c+d-a}{b-a} - \frac{1}{6EI}\frac{c-b+d}{b-a}(b-a)^3 \right]$$

(67)

The values of F_1 and F_2 can be substituted into C_4. This makes (62) become

$$C_4 = EI\left[-\left(\frac{F}{K_A}\frac{c-b+d}{b-a}\right)\right] - C_3 a \tag{68}$$

Substituting (67) into (68) gives the value of C_4

$$C_4 = EI\left[-\left(\frac{F}{K_A}\frac{c-b+d}{b-a}\right)\right] - \frac{FEI}{b-a}\left[\frac{1}{K_A}\frac{c-b+d}{b-a} + \frac{1}{K_B}\frac{c+d-a}{b-a} - \frac{1}{6EI}\frac{c-b+d}{b-a}(b-a)^3\right]a \tag{69}$$

Factoring out F, EI, and a negative sign results in the following

$$C_4 = FEI\left[-\left(\frac{1}{K_A}\frac{c-b+d}{b-a} + \frac{a}{b-a}\left[\frac{1}{K_A}\frac{c-b+d}{b-a} + \frac{1}{K_B}\frac{c+d-a}{b-a} - \frac{1}{6EI}\frac{c-b+d}{b-a}(b-a)^3\right]\right)\right] \tag{70}$$

The value of $\delta(x)$ can now be determined because the constants are known. Substituting (50), (52), (67), (70) into (60), one obtains

$$\begin{aligned} EI\delta(x) = {} & \frac{F}{6}\frac{c-b+d}{b-a}\langle x-a\rangle^3 - \frac{F}{6}\frac{c+d-a}{b-a}\langle x-b\rangle^3 + \frac{F}{6}\langle x-c\rangle^3 + \\ & \frac{F}{2}\left((c-a)\frac{c-b+d}{b-a} + (c-b)\frac{c+d-a}{b-a}\right)\langle x-c\rangle^2 + \\ & \left(\frac{FEI}{b-a}\left[\frac{1}{K_A}\frac{c-b+d}{b-a} + \frac{1}{K_B}\frac{c+d-a}{b-a} - \frac{1}{6EI}\frac{c-b+d}{b-a}(b-a)^3\right]\right)x + \\ & FEI\left[-\left(\frac{1}{K_A}\frac{c-b+d}{b-a} + \frac{a}{b-a}\left[\frac{1}{K_A}\frac{c-b+d}{b-a} + \frac{1}{K_B}\frac{c+d-a}{b-a} - \frac{1}{6EI}\frac{c-b+d}{b-a}(b-a)^3\right]\right)\right] \end{aligned} \tag{71}$$

Factoring out F and dividing by the flexural rigidity, the elastic curve equation reduces to

$$\delta(x) = F\left\{\begin{array}{l}\dfrac{1}{EI}\left(\begin{array}{l}\dfrac{1}{6}\dfrac{c-b+d}{b-a}\langle x-a\rangle^3 - \dfrac{1}{6}\dfrac{c+d-a}{b-a}\langle x-b\rangle^3 + \dfrac{1}{6}\langle x-c\rangle^3 + \\ \dfrac{1}{2}\left((c-a)\dfrac{c-b+d}{b-a} + (c-b)\dfrac{c+d-a}{b-a}\right)\langle x-c\rangle^2\end{array}\right) + \\ \left(\dfrac{1}{b-a}\left[\dfrac{1}{K_A}\dfrac{c-b+d}{b-a} + \dfrac{1}{K_B}\dfrac{c+d-a}{b-a} - \dfrac{1}{6EI}\dfrac{c-b+d}{b-a}(b-a)^3\right]\right)x + \\ \left[-\left(\dfrac{1}{K_A}\dfrac{c-b+d}{b-a} + \dfrac{a}{b-a}\left[\dfrac{1}{K_A}\dfrac{c-b+d}{b-a} + \dfrac{1}{K_B}\dfrac{c+d-a}{b-a} - \dfrac{1}{6EI}\dfrac{c-b+d}{b-a}(b-a)^3\right]\right)\right]\end{array}\right\} \quad (72)$$

4.3.6 Placement of components for variable shaft

As in the constant shaft diameter section, the proper placement of the air bearings and length of the shaft was determined. The defection ratio of $\delta(0)/\delta(c+d)$ was graphed against the length ratio of c/d. Figure 33 was constructed for 50 mm and 32 mm shaft diameters.

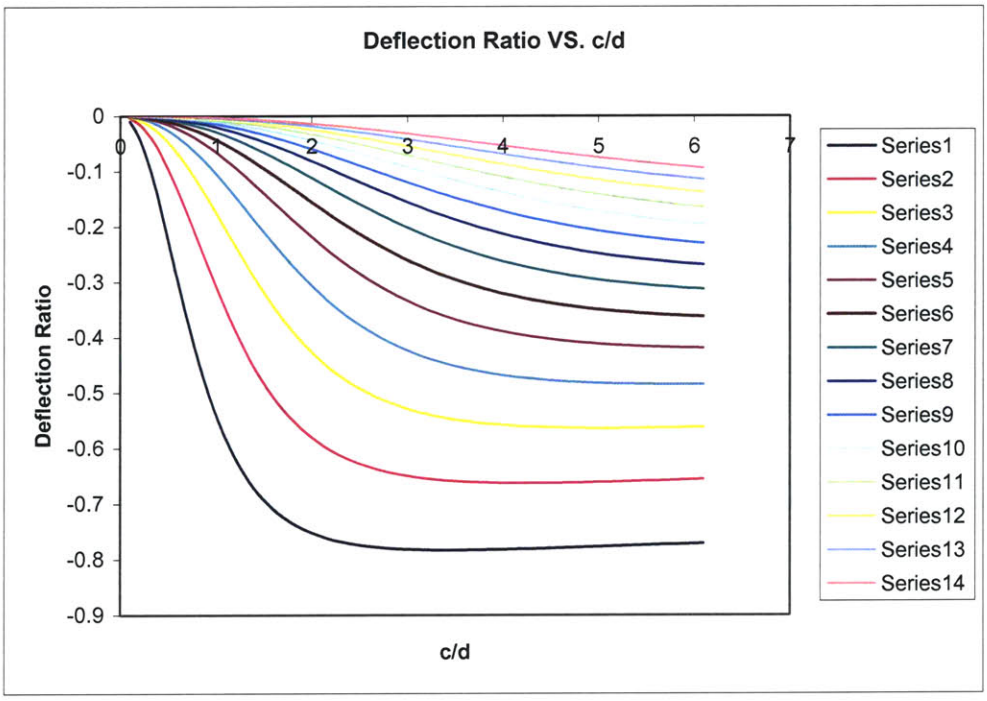

Figure 33: Deflection Ratio for variable shaft

Table 10: C and a values for deflection graph of variable shaft, units in meters

Series	c	a
1	0.13	0.038
2	0.15	0.038
3	0.18	0.038
4	0.20	0.038
5	0.23	0.038
6	0.25	0.038
7	0.28	0.038
8	0.3	0.038
9	0.33	0.038
10	0.36	0.038
11	0.38	0.038
12	0.41	0.038
13	0.43	0.038
14	0.46	0.038

As the length of c increases, the deflection ratio increases at a slower rate and levels off to a constant ratio faster than a smaller value of *c*. Unlike *c*, as the curve moves away from the x-axis, the length of d decreases. Thus a large *c* and *d* is needed. The largest the shaft can be is 914 mm and the shortest is 406 mm.

The deflection in the variable shaft described above, is portrayed in the finite element analysis figure below. The deflection at the point force is 1.9 mm. After the step to the smaller shaft, the deflection decreases by 100 times. The deflection at the step is 0.085 mm. As one passes through the bearing or spring B, the deflection decreases even more to 5.19 microns. Bearing *A* (spring *A*) has the smallest deflection of 2.5 microns. The tip of the shaft has an increase in deflection to 24 microns. When comparing the deflection to the constant shaft, the constant shaft deflects more in the middle to give it a half moon shape where the variable shaft looks more like a tail because at this step, the deflections are absorbed or reduced. The deflection in the stepped shaft is larger than the constant, but as the distance between the tip and Bearing *A* decreases, the deflection decreases as well. In addition, if bearing B is moved from 0.356 m to 0.203 m from the tip of the shaft, then the deflection at the tip decreases to 5.02E-6 m. This is almost 10 times as small as the constant shaft. Thus the deflection depends greatly where the components are placed.

When comparing the FEA analysis and the calculations performed above, they match with a 0.0001 round off error.

Figure 34: FEA of Variable Shaft

4.3.7 Optimization of the shaft

As the two shafts decrease in size, the deflection ratio tends to 0 faster than the 50 mm and 32 mm shaft diameters. Figure 35 displays this

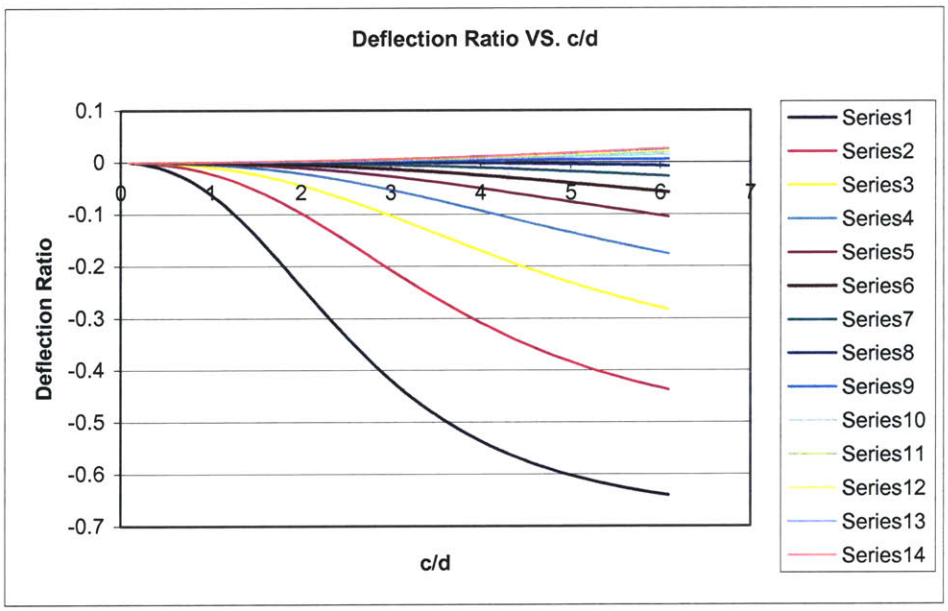

Figure 35: c=1" diameter and d=0.5" diameter for the variable shaft

Thus a smaller diameter shaft could be used but given that the deflection ratio decreases with decreasing diameter, the stiffness decreases as well. The overall torsional stiffness of the machine has to be greater than what is required to machine the part. Even though the deflection is smaller, the larger diameter is desirable because the stiffness is larger.

4.3.8 Making a two piece shaft

Many options were considered when making a shaft with two different diameters. Part of the 32 mm shaft could be turned down to a 25.4 mm section; the larger shaft could be heated while the smaller shaft frozen and then both press fitted together through a pilot hole on the larger shaft; or they could be connected by a coupling, with stiffness in the axial direction.

Modeling the variable shaft in ProMechanica helped determine which mechanism to use. First the use of the deflection ratio graphs determined the proper length of the shaft. Then the stepped shafts were modeled in ProMechanica. The dimensions were 280 mm for the 50 mm diameter shaft and 228 mm for the 32 mm diameter shaft. There is a large amount of deflection at the tip of the shaft when it is turned down to a smaller diameter. On the other hand when a force was produced between the bushings, it was noticed the error was absorbed at the coupling of the shaft and little movement was noticed at the tip. The length of the shaft stays the same but when a coupling is introduced it rids the motion at the bushings by 100 times.

The coupling was designed as two steps in the shaft. The following derivation was used to find the proportionality between the size of the step and overall length of the shaft.

The shaft has a diameter of 25 mm and the coupling connectors have a diameter of 6.35 mm and a length of 12.7 mm. Since this is small there is no need to buy a coupling. The shaft can be fabricated to have the multiple steps in it. The length is still long about 585 – 610 mm with the added coupling. Without the coupling the placement of components uses 457 mm of the shaft. The deflection curve for the 25.4 mm shaft is presented in Figure 36. The deflection at the nuts end is 3.249E-3 m and the deflection at the spindle tip is -3.048E-6 m. That is three orders of magnitude difference. If the connector is increased to 12.7 mm diameter, then the deflection at the nuts decreases to 4.748E-4 m but the deflection at the spindle end remains the same, -3.048377E-6 m. The coupling connector substantially makes a difference.

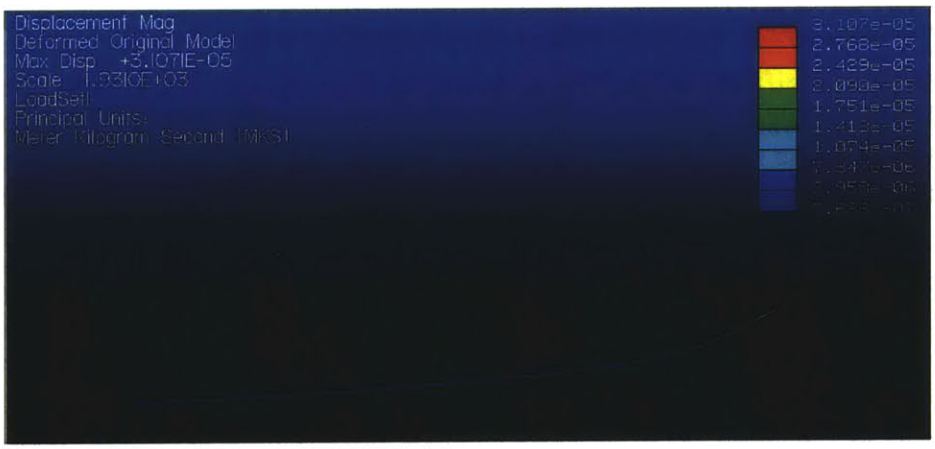

Figure 36: ProMechanica FEA of variable shaft

Since the longest part of the shaft is where the air bearings reside and the largest deflection is 0.7 microns, the air bearing section of the shaft could be removed. This would make the machine more compact given the amount of error in the system. It was decided to test the amount of deflection by building the machine without the air bearings only the nuts section. See Chapter 6 for the results.

4.4 Natural Frequency of System

The natural frequency is important to know because it should not be excited when the spindle is cutting. When this frequency is excited, vibrations occur and cause further error when machining the part. When determining the natural frequency of the system, each component's stiffness and inertia has to be calculated. The inertia can be calculated from any dynamics book [23]. The inertia depends on the geometry of the component but is the integral of the area to the neutral axis. After it is found, then it is translated to the neutral axis of the machine. That is

$$I = \bar{I} + md^2 \tag{73}$$

where $\bar{I}$ is the inertia of the original component, m is the mass of the component and d is the distance from the components neutral axis to the neutral axis of the machine. Table 11 gives the inertia of the components

Table 11: Inertia of Mesomill Components

Component	Inertia (kg/m^2)
Ball screw-spline shaft	1.4E-4
Shaft bushing	4.7E-4
Spindle	6.9E-2
Spindle linear motor	8.7E-2
Structure to support spindle and linear motor	1.7E-2

These components were assumed using a 32 mm diameter ball-screw spline shaft.

Next the torsional stiffness of the ball screw-spline shaft and belt drive motor were determined. Given the length of the shaft which was determined from the beam bending equation, and its diameter, the inertia and stiffness is found. Starting with a shaft diameter of 8 mm and increasing to 32 mm, the inertia for a circle is found with the following equation and units of m^4.

$$I = \frac{\pi d^4}{32} \tag{74}$$

Torsional stiffness requires inertia, shear modulus of elasticity, and length of shaft.

$$\phi = \frac{TL}{GJ} \tag{75}$$

Rearranging the above equation to produce torque over the angle of twist gives the torsional stiffness

$$K_{torsional} = \frac{GI}{L} \tag{76}$$

Natural frequency is a function of inertia and torsional stiffness:

$$\omega = 2\pi\sqrt{\frac{K}{J}} \tag{77}$$

The highest natural frequency calculated is 13 Hz for a 32 mm ball screw-spline shaft when using a belt drive. The belt stiffness can be looked up in a table or calculated by

$$K_{total} = \frac{1}{\frac{1}{K_{belt}} + \frac{1}{K_{shaft}}} \tag{78}$$

Where K_{belt} and K_{shaft} are the stiffness of the belt drive and shaft respectfully.

4.5 Motor Determination

There were two transmissions considered for the MesoMill. They were a cable capstan drive and a dual pinion. Since the cable capstan was chosen as the transmission due to its high stiffness and relatively antibacklash, the dual pinion will be described in Appendix A. The capstan drive is discussed below.

4.5.1 Capstan drive

Wire capstan drives are used as rotary transmission elements for their very low (nominally zero) backlash and high stiffness properties. To obtain high stiffness, the cable is typically wrapped around the input and output drum in a figure-eight pattern multiple times. The torsional stiffness can be determined by analyzing the amount of deformation between the cable and the drums using the classic capstan analysis approach and the free cable length between the drum. A test stand was built and used to validate the model.

4.5.1.1 Capstan Engagement Angle

A wire capstan drive is composed of an output drum, with diameter D_{output}, and an input drum, with diameter D_{input}, and a connecting cable. The cable can be wrapped multiple times between the input and output transmission drums in a figure-eight pattern. Figure 37 shows the basic representation of this drive.

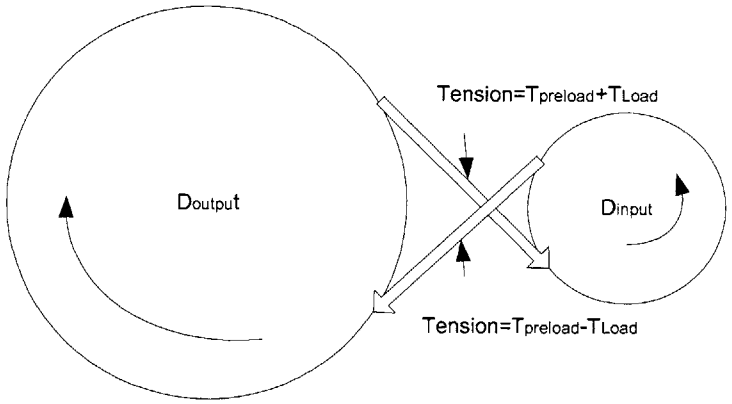

Figure 37: Representation of Capstan drive where arrows represent direction of drum and cable motion.

Initially tension exists in the cable which is the preload force, $T_{preload}$. If an external torque, Γ_{drum}, is applied to the input drum D_{input}, part of the cable extends due to increased tension, while the other part contracts due to tension being relieved. For example if the input drum is rotated counter-clockwise in Figure 37, a reasonable assumption is the tension in one cable will increase by some amount ΔT, which will be called T_{Load}, and the tension in the other cable will be reduced by some amount T_{Load}. For illustrative purposes, this can be demonstrated with a rubber band encircling a cylinder (soda can). Inserting a finger under the rubber band, twisting, and pulling outward creates a device that looks like a capstan drive. As the cylinder is rotated counterclockwise, the rubber band only stretches on the right hand side. Coloring the portion of the rubber band on the upper and lower surface of the cylinder helps with visualization. This extension and contraction of the rubber band is due to friction between the band and the cylinder.

As shown in Figure 38, the active tractive region of interest, where cable extension on the drum dynamically occurs, can be defined as acting over an angle θ_{slip} which is the section of the cable where some slip can occur while the cable is loaded. This angle is the angle one would derive from the classic capstan equation as being required to hold the applied load, given a differential tension in the cable. As shown in Figure 38, $\theta_{slip1} + \theta_{no\text{-}slip} + \theta_{slip2}$ are equal to θ_{wrap}. For a robust design $\theta_{no\text{-}slip}$ must be greater than zero and if θ_{wrap} is greater than 2π, it indicates that there are multiple wraps on a drum.

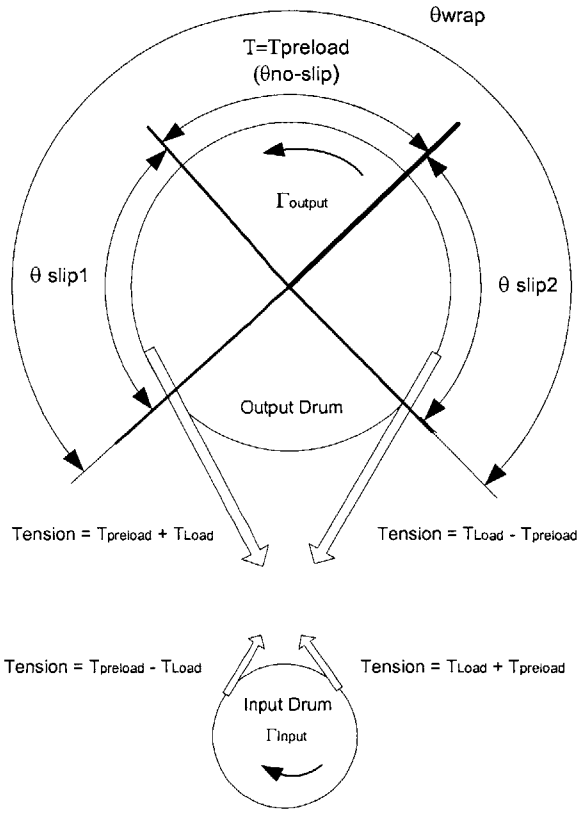

Figure 38: Nomenclature for the two models of the stiffness derivation.

From a torque balance, T_{load} can be determined.

$$\Gamma_{drum} = \left(T_{preload} + T_{Load} - (T_{preload} - T_{Load})\right) r_{drum}$$

$$\Rightarrow T_{load} = \frac{\Gamma_{drum}}{2r_{drum}} \tag{79}$$

The input and output drum torques create an elongation in the cable. Note the cable was already slightly extended from the initial cable length due to the preload force. Since the system is in equilibrium with the preload force, its current length will be considered the initial length and any additional extension is what is of interest with respect to determining the stiffness. Figure 39 shows the free body diagram of a small segment, dL, of the stretched cable in traction with the drum. The small segment of the cable dL is equivalent to rdθ. .

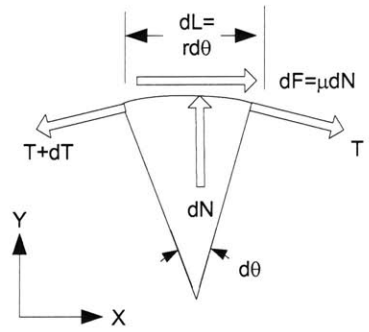

Figure 39: Differential cable element.

dF represents the traction force that is seen by the segment dL due to friction between the cable and the drum and dN is the normal force from the cable in contact with the drum. Summing the forces in the x and y direction:

$$\sum F_X = T\cos(\frac{d\theta}{2}) + \mu dN - (T + dT)\cos(\frac{d\theta}{2}) = 0 \tag{80}$$

$$\sum F_Y = dN - T\sin(\frac{d\theta}{2}) - (T + dT)\sin(\frac{d\theta}{2}) = 0 \tag{81}$$

Since dθ is infinitesimally small:

$$\frac{dT}{T} = \mu d\theta \tag{82}$$

Integrating from 0 to a tension T and 0 to θ, where θ is the angle-of-slip, not the angle of entire contact, as defined in Figure 38, produces the following results

$$\int_{T(\theta)}^{T} \frac{dT}{T} = \mu \int_0^{\theta_{slip}} d\theta \tag{83}$$

The tension T experienced by a segment of the cable is

$$T(\theta) = Te^{-\mu\theta_{slip}} \tag{84}$$

Expression (82) is the classic capstan equation and valid only for that section of the cable that is needed to withstand the torque. Interpreting the above equation into the system

presented in Figure 38 produces the following two results for the two regions θ_{slip1} and θ_{slip2}:

$$\theta_{slip1} = \frac{1}{\mu} \ln\left(\frac{T_{preload} + T_{Load}}{T_{preload}}\right) \tag{85}$$

$$\theta_{slip2} = \frac{1}{\mu} \ln\left(\frac{T_{preload} - T_{Load}}{T_{preload}}\right) \tag{86}$$

4.5.1.2 Cable Deformation

From Hooke's Law, the term Æ for the cable is defined as the product of the modulus of elasticity and the effective area since the cross sectional area of a cable is difficult to define:

$$\varepsilon = \frac{T}{Æ} \tag{87}$$

The load strain can also be stated as the amount of deflection divided by the unstretched length of the segment under consideration

$$\varepsilon = \frac{d\delta}{dL} = \frac{d\delta}{r_{drum} d\theta} \tag{88}$$

Setting equation (87) and (88) equal and solving for $d\delta$ produces the following

$$d\delta = \frac{Tr_{drum}}{Æ} d\theta \tag{89}$$

where $d\delta$ is the elongation in the small segment dL under average tension T at that point. Equation (89) is the change in deflection due to the preload and load force. The deflection of interest is the extension due to just the load. Thus the preload force must be subtracted out.

$$d\delta = d\delta_{Tpreload+Tload} - d\delta_{Tpreload} = \frac{Tr_{drum}}{Æ} d\theta - \frac{T_{preload} r\theta_{slip}}{Æ} \tag{90}$$

4.5.1.3 Cable deformation on slip side 1

The relation between the deflection in the cable, tension, drum radius, effective modulus, angle-of-slip, and equations (85) and (89), produces the elongation of the cable on slip side 1 of the drum:

$$\int_0^{\delta} d\delta = \int_0^{\theta_{slip1}} \frac{\left(T_{preload} + T_{Load}\right) r_{drum}}{Æ} e^{-\mu\theta} d\theta - \frac{T_{preload} r_{drum} \theta_{slip}}{Æ}$$

(91)

Following through with integration produces the basic form of the elongation of the cable:

$$\delta = \frac{r_{drum}\left(T_{preload} + T_{Load}\right)}{Æ\mu}\left(1 - e^{-\mu\theta_{slip1}}\right) - \frac{T_{preload} r_{drum} \theta_{slip}}{Æ}$$

(92)

where δ is the elongation of the cable for the region of θ_{slip1} and represents the extension in the cable due to the external torque on slip side 1 of the drum. Combining like terms, the deflection is determined as a function of T_{load}, cross-sectional area of the cable, modulus of elasticity, coefficient of friction, and radius of the drum:

$$\delta = \frac{r_{drum}\left(T_{preload} + T_{Load}\right)}{Æ\mu}\left(1 - \frac{T_{preload}}{T_{preload} + T_{Load}}\right) - \frac{T_{preload} r_{drum}}{Æ}\frac{1}{\mu}\ln\left(\frac{T_{preload} + T_{Load}}{T_{preload}}\right)$$

(93)

$$\delta = \frac{r_{drum}}{Æ\mu}\left(T_{Load} - T_{preload}\ln\left(\frac{T_{preload} + T_{Load}}{T_{preload}}\right)\right)$$

(94)

Next the stiffness is determined by taking the inverse of the partial derivative with respect to T_{load}, $\frac{1}{K} = compliance = \frac{d\delta}{dT_{load}}$:

$$K_{o\_slip1} = 2\frac{\mu AE}{D_{output}}\frac{T_{preload} + T_{load}}{T_{load}}$$

(95)

Likewise for the input drum the stiffness is:

$$K_{i\_slip1} = 2\frac{\mu Æ}{D_{input}}\frac{T_{preload}+T_{load}}{T_{load}}$$

(96)

4.5.1.4 Cable deformation on slip side 2

Calculating the deflection on slip side 2 of the drum considers equation **(89)**:

$$\int_0^{\delta} d\delta = \int_0^{\theta_{slip2}} \frac{\left(T_{preload}-T_{Load}\right)r_{drum}}{Æ}e^{-\mu\theta}d\theta - \frac{T_{preload}r_{drum}\theta_{slip2}}{Æ}$$

(97)

Following through with integration produces the basic form of the elongation of the cable:

$$\delta = \frac{r_{drum}\left(T_{preload}-T_{Load}\right)}{Æ\mu}(1-e^{-\mu\theta_{slip2}}) - \frac{T_{preload}r_{drum}\theta_{slip2}}{Æ}$$

(98)

where δ is the elongation of the cable for the region of θ_{slip2} and represents the extension in the cable due to the external torque on slip side 2 of the drum. Combining like terms, the deflection is determined as a function of T_{Load}, cross-sectional area of the cable, modulus of elasticity, coefficient of friction, and radius of the drum:

$$\delta = \frac{r_{drum}\left(T_{preload}-T_{Load}\right)}{Æ\mu}(1-\frac{T_{preload}}{T_{preload}-T_{Load}}) - \frac{T_{preload}r_{drum}}{Æ}\frac{1}{\mu}\ln\left(\frac{T_{preload}-T_{Load}}{T_{preload}}\right)$$

(99)

$$\delta = -\frac{r_{drum}}{Æ\mu}\left(T_{Load}+T_{preload}\ln\left(\frac{T_{preload}-T_{Load}}{T_{preload}}\right)\right)$$

(100)

The stiffness is determined by taking the inverse of the partial derivative with respect to T_{load}, $\frac{1}{K} = compliance = \frac{d\delta}{dT_{Load}}$:

$$K_{0\_slip2} = 2\frac{\mu Æ}{D_{output}}\frac{T_{preload}-T_{Load}}{T_{load}}$$

(101)

Likewise for the input drum the stiffness is:

$$K_{i\_slip2} = 2\frac{\mu Æ}{D_{input}}\frac{T_{preload} - T_{Load}}{T_{load}}$$

(102)

Equations (95) and (101) are the limits of the total deflection on the output drum due to the extension in the cable from the external torque and preload and equations (96) and (102) are the limits of the total deflection due to the extension in the cable from the external torque and preload on the input drum.

4.5.1.5 Cable deformation in free length section

The free length deflection of the cable is determined from Hooke's law and is

$$\Delta l = \frac{TL_{free}}{Æ}$$

(103)

Taking the inverse of the compliance produces the stiffness of the cable that is not in contact with the drum. Note that the stiffness of each free length is

$$K_{free} = \frac{Æ}{L_{free}}$$

(104)

An expression for L_{free} can be obtained from the capstan's geometry shown in Figure 40. The distance between the input and output drum, radius of the two drums and distance between the two drums gives L_{free}:

$$L_{free} = \sqrt{{L_{cd}}^2 - {r_{output}}^2 - {r_{input}}^2 + 2\frac{r_{input}}{r_{output}}L_{output}(1-\sec\theta)}$$

(105)

Which is difficult to solve. According to M.F. Spotts [24], the center distance L_{CD} can be determined using the equation:

$${L_{free}}^2 = {L_{CD}}^2 + \left(r_{output} - r_{input}\right)^2$$

(106)

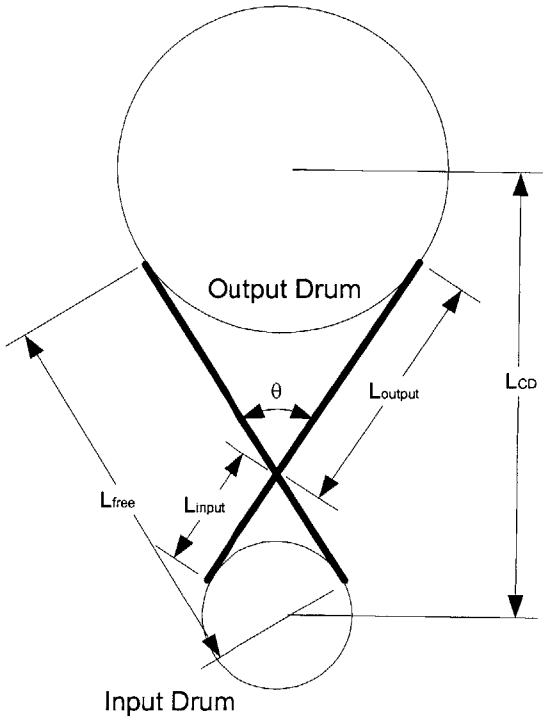

Figure 40: Nomenclature for determining the free length L_{free} of the cable.

4.5.1.6 Net Output Torsional Stiffness

The stiffness of the output drum can be modeled as effectively having three springs on either side as shown in Figure 41 and Figure 42. These springs represent each section of the cable for each of the two sides of the drums: a section on the output drum, the free-length section between the drum, and a section on the input drum. K_{o_slip2} and K_{o_slip1} are the stiffness associated with cable on the output drum over regimes θ_{slip1} and θ_{slip2} where some deformations can occur. K_{free} is the stiffness of the cable between drums. K_{i_slip1} and K_{i_slip2} are the stiffnesses associated with cable on the input drum over region θ_{slip1} and θ_{slip2} respectively.

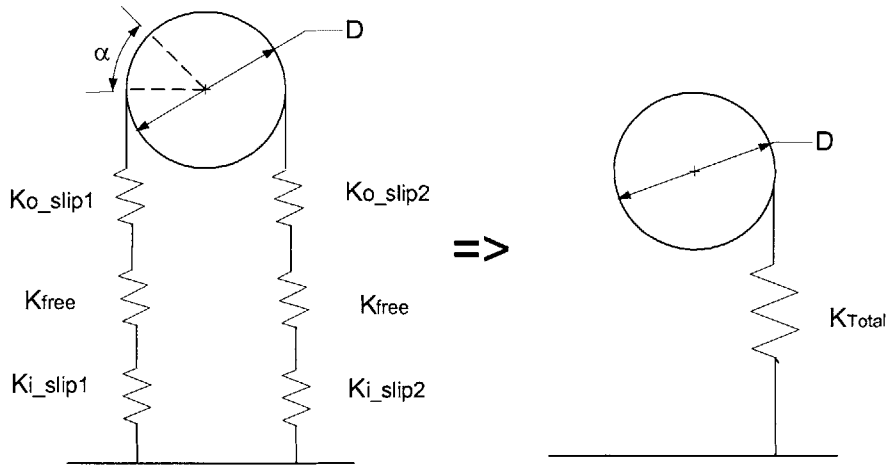

Figure 41: Spring model of capstan drive output drum.

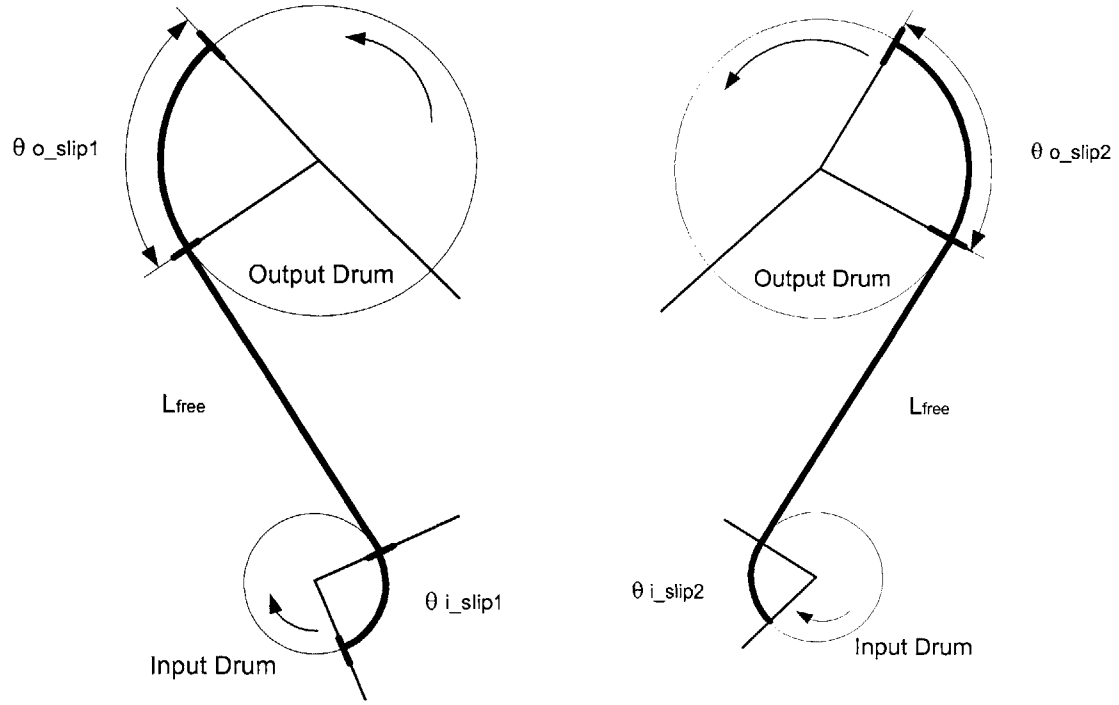

Figure 42: Partition of cable.

Determining the stiffness on each side of the drum produces the first and second side of the stiffness, respectively.

$$K_1 = \frac{1}{\frac{1}{K_{o\_slip1}} + \frac{1}{K_{free}} + \frac{1}{K_{i\_slip1}}} = \frac{K_{o\_slip1}K_{free}K_{i\_slip1}}{K_{o\_slip1}K_{free} + K_{o\_slip1}K_{i\_slip1} + K_{free}K_{i\_slip1}}$$

(107)

$$K_2 = \frac{1}{\frac{1}{K_{o\_slip2}} + \frac{1}{K_{free}} + \frac{1}{K_{i\_slip2}}} = \frac{K_{o\_slip2}K_{free}K_{i\_slip2}}{K_{o\_slip2}K_{free} + K_{o\_slip2}K_{i\_slip2} + K_{free}K_{i\_slip2}}$$

(108)

The two sides act in parallel thus the cable's total longitudinal stiffness is the addition of these two springs in parallel. Adding the two sides together produces:

$$K_{Total} = K_2 + K_1$$

(109)

The torsional stiffness of the output drum is determined from Figure 41 where:

$$\delta = \frac{\Gamma_{drum}}{r_{drum}K_{total}}$$

(110)

$$\alpha = \frac{\delta}{D_{drum}/2} \Rightarrow \frac{4\Gamma}{D_{drum}^{\ 2}K_{total}}$$

(111)

Since $\Gamma_{drum} = K_{Torsion}\alpha$, the torsional stiffness of the output drum $K_{Torsion}$ has the value:

$$K_{Torsion} = \frac{D_{drum}^{\ 2}K_{total}}{4}$$

(112)

4.5.2 Motor Sizing

Given the stiffness of the dual pinion and capstan drive, the later has the highest and ease of manufacture. In addition, the capstan has no backlash and is less expensive to make. Thus the capstan drive was used instead of the dual pinion.

The size of the motor was determined through the process presented by George Newton [25]. It is only required to know 6 variables about your system, the sixth variable being an initial guess. They are: load moment of inertia (J_L), load torque (T_L), move distance (S_L), move time, (t_m), dwell time (t_d), and established motor time constant

(tau_m). The established motor time constant is guessed initially. Then after the first iteration, it is changed with the new value from the motor, refer to Table 12.

The iteration starts off with a guessed value for the time constant. Then the load power rate, least permissible motor power rate, minimum rated power rate, average armature power dissipation, and allowable dissipation is calculated with the known information. These new found parameters are then looked up in a motor manufactures handout to see which motor closely matches these values. Once found, the listed motor moment of inertia and motor peak speed is used to find the gear ratio which in turn calculates the peak motor torque. If the peak motor torque is twice as large as the rated torque, then the motor can be used, if not, a different time constant is picked from the literature and the iteration is repeated.

The capstan drive acts like a gear reducer in that the input drum is the pinion and the output drum is the gear. The value for the size of the drum is determined by the size of the stiffness wanted and how much room is available to accommodate the drum.

The inertia, torque and velocity profile produced by the capstan, spindle holder and spindle itself were determined. The inertia of the rotary motion is 0.1356 kg-m^2 and the linear inertiais 0.1384 kg. Notice the inertia for the linear capstan is larger due to a thicker drum; the drum rotates 540 degrees where the rotary drum rotates 180 degrees. The output diameter is 280 mm and the input is 50.8 mm.

The torque due to the linear movement is calculated from:

$$Torque = a \cdot m \cdot F_{cut} \cdot F_{friction} \tag{113}$$

where a is the linear acceleration, m is the mass in motion, F_{cut} is cutting force, and F_{friction} is the bearing friction force. The rotary torque was determined by the given equation

$$Torque_{acceleration} = \alpha \cdot I \cdot \Gamma_{static} \tag{114}$$

where α is the angular acceleration, I the total rotating moment of inertia and G_{static} is the static torque due to gravity. These values are: linear 0.195 N-m/rad; rotary: 0.4276 N-m/rad.

A trapezoidal velocity trajectory with equal time intervals for the acceleration, constant velocity, and deceleration, is considered in this case. The optimum velocity profile of a parabola will not be considered due to the difficulty in achieving this profile. Since the trapezoidal trajectory interval is one-third the total move time, this profile requires less power per move because the load is moved at equal intervals instead of an instant peak in acceleration like in a triangle trajectory [26]. Lastly the trapezoidal trajectory was chosen because its efficiency is 89% in applications where the triangular profile is 75%.

These values were inputted into George Newtons formulas and the following chart was produced:

Table 12: Motor determination using George Newtons method

Given Variables:		
Load moment of inertia, J_L	0.1355	kg*m^2
Load Torque, T_L	0.4	N-m
Move distance, S_L	0.0254	m
Move time, t_m	1	sec
Dwell time t_d	1	sec
Est. motor time constant, tau_m	0.01329	sec
After iteration:		
Gear ratio after iteration, R_1	5.5	
Motor peak input power expression, P_m	1.023	Watts
Rated Power rate , P_dot_mr	6.50E+02	watts/sec
Rated Torque, T_mr	3.40E+00	N-m

Outputs:		
Peak load acceleration, A_L	0.0254	m/sec^2
Load power rate, P_dot_L	0.010247419	Watts/sec
Least permissible motor power rate, P_m1	0.330818026	Watts/sec
Minimum rated power rate, P_mr	162.5	Watts/sec
Parameters for the average power dissipation		
alpha	0.166666667	
delta	0.5	
rho	0.991469152	
Average armature power dissipation, P_a	0.00159127	Watts
Allowable dissipation, P_aa	8.6385	Watts
If above is acceptable:		
Motor moment of inertia, J_m	0.017784615	kg-m^2
Gear ratio normalization, R_go	29.88486481	
R_g1	164.3667565	
Motor peak speed, V_m	1.391638538	rad/sec
	13.28916914	Rev/min
Peak motor torque, T_m	0.07670379	N-m
Is this above 2*rated torque (T_mr)	yes	
Is this above 4*rated torque (T_mr)	yes	
	yes	

Given these numbers, multiple companies, like Kollmorgen or Pacific Scientific, were researched to find a motor that has the same inertia and has a continuous torque larger than what is needed. The ideal case is to find a motor with the same inertia. No gearbox would be needed because the capstan acts like a gearbox in that it gives a 11:2 reduction. This makes the reflected load inertia to be

$$J_{\text{Re flected}L} = \frac{J_L}{GR^2} \tag{115}$$

which is 0.0045 for rotary and linear inertia. Thus the ratio of the load inertia to the motor inertia is 2.38 when a motor inertia of 0.00192 is chosen. This is not ideal because the overshoot in the system to reach its target would be around 40%. Fortunately with the proper tuning, stability will be met and will give 0% overshoot. Given the above calculations the PMA53Q was chosen for the motor of the rotary and linear drive system.

The following figures display the rotary and linear trapezoidal trajectory and speed profiles.

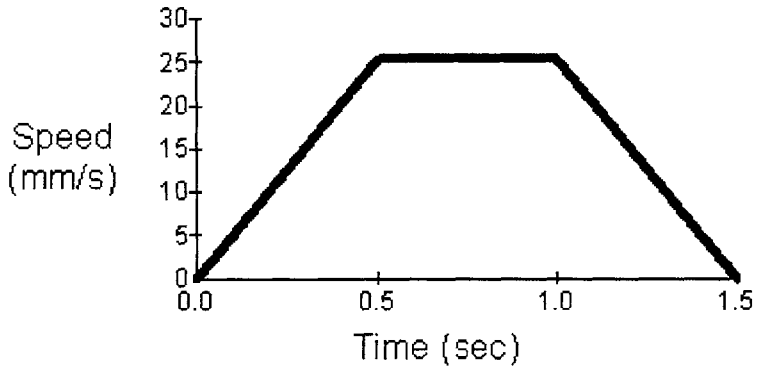

Figure 43: Ball-screw spline's rotary trapezoidal trajectory[7]

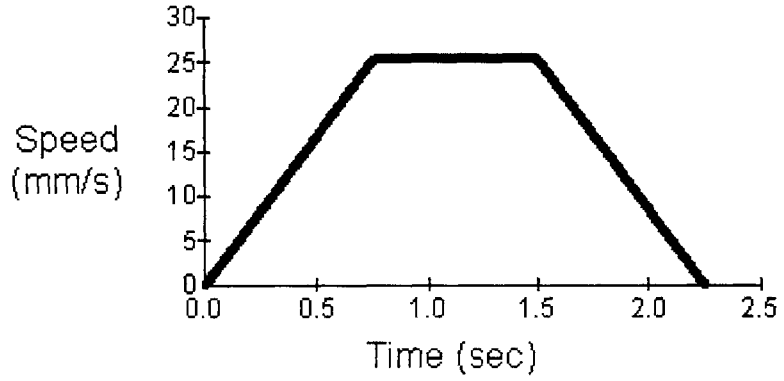

Figure 44: Linear Trapezoidal Trajectory for the Ball-screw spline.

[7] Figure 43 - Figure 46 were created using a program from motion engineering and can be found at Kollmorgen motors http://www.motionvillage.com/

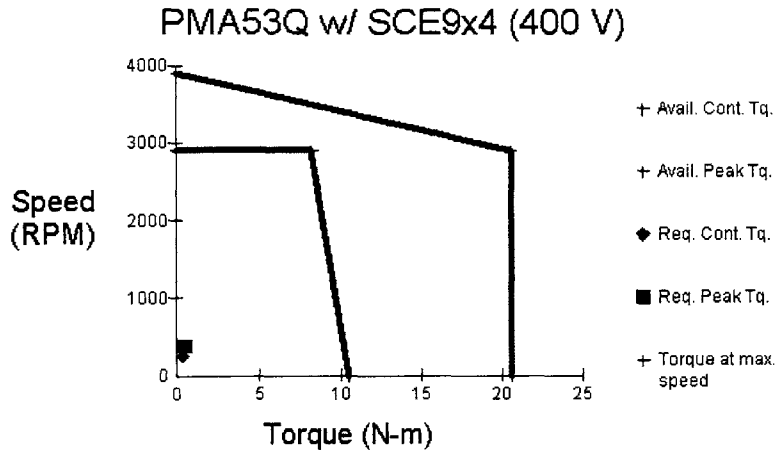

Figure 45: Rotary Speed Profile for the PMA53Q motor.

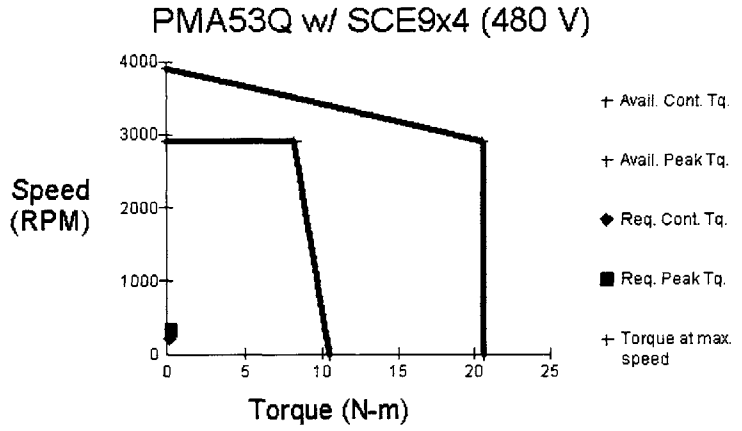

Figure 46: Linear Speed Profile for the PMA53Q motor.

4.6 ESI Aerostatic spindle errors

The aerostatic spindle donated from ESI was measured at NIST to determine the error motion of the axes of rotation. Error motion is defined as the relative displacement between the sensitive directions of the tool to the work piece [27]. These error motions cause degradation of performance, limit surface finish and roundness capability. The sensitive direction in the aerostatic spindle is classified as the rotating sensitive direction because the work piece is fixed and the point of machining rotates with the spindle. The error motion that is normal to the axis of rotation is called radial motion. This is the type of motion that is of interest.

From here the errors can be classified as synchronous or asynchronous and are described below and can be found in references [27] - [29].

4.6.1 Average and asynchronous errors in an aerostatic spindle

Errors synchronized with the spindle rotation are called average or synchronous. According to the ANSI/ASME B89.3.4M-1985, "Axes of Rotation, Methods for Specifying and Testing," The term "synchronous error motion" is a nonpreferred term for average error motion since the latter can actually include asynchronous error motions, which do not necessarily average out to zero. So average error motion is used instead, but in this thesis, the two are interchangeable. Many factors can cause the average error motions. For example, out-of-round bearing races or seats, imbalance, non-uniform stiffness in a spindle or machine structure, and resonance in the spindle or machine structure, are all contributing factors. The errors not synchronized with the spindle rotation are called asynchronous. Like the average error motion, they can be caused by many factors. Such as, imperfections in rolling element bearings, contaminated lubricant, structural vibrations, and floor vibrations. This causes surface finish degradation and premature tool wear.

Data was collected in two forms, polar plots and least squares circle (LSC). The polar plots show the target position at successive angular locations on successive rotations. It is similar to the roundness plots of a machined part. The least-squares circle is used in calculations of rotational error motions and defines the ideal and actual motion of a rotating spindle. In the calculation of some error motions, relative to the LSC, other circles are drawn. The relationship of their radii describes the error motion value. The radius of the LSC is generated by the intentional eccentricity of the target and is used to adjust the plot and establish the plots center called the polar chart center (PC). This is all done in Lion Precision's software, "Spindle Error Analyzer" (SEA) [28].

Lion Precision software collects the data through capacitance probes. The capacitance probes were calibrated because they ideally read off flat surfaces which is at least 30% larger than the sensor area. The one-eighth inch diameter cylindrical drill shank does not fit into this category. With a correction factor of .7, the capacitance probes will give acceptable values.

4.6.2 Error motion calculations performed on the ESI spindle

Many calculations can be conducted using the polar plots. Listed below are the different calculations performed using Lion Precision's software SEA [27][28][29].

4.6.2.1 Total error motion in the aerostatic spindle

Total error motion is the combination of all the error motions in the spindle. This number gives an initial assumption of the capability of the machine tool to produce parts. A LSC is calculated from the data and drawn on a plot. The center of the LSC is at the center of the graph, or PC. In other words, this represents the center of the rotating spindle. Two more circles are drawn with the same center. One circle called the *maximum inscribed circle* (MIC) is the largest circle that can be inscribed within the error motion polar plot. The other circle is called the minimum circumscribed circle (MCC). It is the smallest

circle that will just contain the error motion polar plot. The difference between these two radii is the total error motion value.

4.6.2.2 Asynchronous error motion in the aerostatic spindle

The fuzziness in the polar plot is due to the asynchronous error motion. The target varies significantly with each revolution. This is because, they are not time related to the rotational frequency of the spindle and it is the non-repeating position at each angular location that causes the fuzziness. The *asynchronous error motion* value is calculated by subtracting the minimum data range by the maximum for each angular location. After comparing the ranges and the largest range is selected, then this value is the asynchronous error motion value.

4.6.2.3 Synchronous Error Motion (Average Error Motion) in the aerostatic spindle

Synchronous errors are related to the rotational frequency of the spindle. The plot of a completely synchronous error motion would have a pattern with the same value at each angular location on each successive rotation. This is the ideal case and in the real world the synchronous error has to be extracted from the asynchronous data. To extract the synchronous error value, the values at each angular location of the synchronous and asynchronous error, are averaged. Then they are plotted and show the average position at each angular position. This is why the Synchronous error motion is also called the average error motion. To calculate the synchronous error motion, draw two circles like in the total error and take the difference between the two radii of the circles.

4.6.2.4 Fundamental error motion (axial only) of aerostatic spindle

The error that occurs exactly once per revolution is the fundamental error motion. This appears like the eccentricity motion in radial measurements. Since there is no eccentricity in this axis, it represents the actual error motion. The best-fit curve determines the amplitude of once per revolution movement. The amplitude of this calculation is the *fundamental error motion*.

4.6.2.5 Residual error motion (axial only) of aerostatic spindle

After the fundamental error is removed, the *residual error motion* is what remains. It is the error motion that occurs at multiples of the rotational frequency but not at the rotational frequency. To calculate this value, subtract the fundamental error from the collected data. The data that remains includes the residual error motion and the asynchronous error motion. Just like the calculation for the radial synchronous error, the data at each angular location is averaged and plotted on the chart. The residual error motion is the difference in the radii of the two concentric circles that just contain the averaged data.

The above errors are attributed to finite stiffness of the spindle and imbalance. They also affect the resonant frequencies of the machine making them unfavorable.

4.6.3 Implementing calculations with tests

4.6.3.1 Rotating Sensitive Radial test

Positioning two probes 90 degrees to each other measuring the X and Y displacement of the axis of rotation generates a polar plot. The method of Tlusty [30] as described in *Systems and Methods of Testing Machine Tools* is used to produce the polar plot. The equation used to display the error motion polar plot is given below

$$r(\theta) = r_O + \Delta X(\theta)\cos\theta + \Delta Y(\theta)\sin\theta \tag{116}$$

where θ is the angle of rotation of the spindle, $\Delta X(\theta)$ and $\Delta Y(\theta)$ are the outputs of the gage oriented with the x axis and y axis respectfully, and r_o is the value of the radius set by the alignment of the artifact.

This test is valid for processes such as milling, boring, and drilling.

4.6.3.2 Fixed Sensitive Radial test

In a polar plot, the data from the displacement in the X direction relative to angular position is displayed in the *fixed sensitive radial tests*. This test is valid for processes such as grinding and turning where the part is rotating in the spindle. It is also valid if the point of contact between the grinding wheel and part are at a fixed position like in surface grinding. This plot is used by SEA to determine the error in the spindle relative to the target. The SEA program to determine this is called Target Reversal.

4.6.3.3 Target Reversal test

Used with Fixed radial tests, the *target reversal test*, allows data from two test runs to be combined in a way that errors in the target are separated from the synchronous error motion of the spindle.

5 Experimentation

5.1 Beam bending experimental procedure

To experimentally prove the beam bending equation that was presented in Chapter 4, experiments were performed. How long the shaft should be, should it be variable or constant, and if air bearings are truly needed were the questions answered. The first experiment was done with a constant 25 mm diameter by 914 mm long shaft that had two linear bearings representing the air bearings. A force was inputted where the ball-screw spline nuts would be. The test was then repeated for the variable shaft, 25 mm diameter by 457 mm long which represented the sleeve and 12 mm diameter by 50 mm long which represented the ball-screw spline shaft. The two shafts were press fit together, the larger diameter was heated and the smaller one dipped in liquid nitrogen. The overall length of the shaft was 1000 mm. The second experiment was similar to the first but the linear bearings were replaced with air bearings.

5.1.1 Process Plan

Below is the process plan followed in determining the stiffness of the bearings and deflection in the two shafts, constant and variable. See reference [22] for a further investigation. Refer to Figure 47- Figure 52.

Align Components

1. Mount bearings onto bearing spacer blocks and screw blocks into table loosely. Instert shaft through bearings to align and tighten bearings down.

2. Install measuring blocks on shaft; align them first by resting them on a flat surface. Use precision shims to give enough clearance for the pillow blocks.

3. Align cap probe mount blocks by inserting a percision spacer between them and the measuring blocks on the shaft.

4. Mount cap probes in holders. Make sure measuring surfaces are perpendicular to the cap probes, set the cap probes to read zero volts, and tighten.

5. When moving bearing blocks around, use cap probe measurements to check for alignment of the shaft with the cap probes. An alternative method is to use a straight edge to align the sides of the bearing spacer blocks.

Measuring Bearing Stiffness

1. Mount and align components as follows: two bearings with one cap probe in between them, with a measuring block on the shaft at that point. The cap probe should be mounted opposite the black, uncut side.

2. Rotate table so that it rests on its back side. Tie a string to the shaft so that it attaches at either side of the block and hangs down. Use this string to hang weights.

3. Measure the stiffness of the bearings by varying the weight that hangs from the shaft and noting displacement.

Measure Shaft Deflection

1. Set up and align components with the micrometer at the rear with the rear cap probe nearby, and the two-linear/air bearings a specified distance apart. Mount the front cap probe in the front most two holes.

2. Take data; at least 15 points and at least 15 microns total deflection, but best number and resolution of data points is yet to be determined.

3. Take data while increasing and decreasing displacement to test for any hysteresis effects.

4. Set up at least 3-5 curves; move either the front bearing to change the distance in the bearings without affecting the distance to the rear cap probe, or move the rear bearing to change bearing spacing without affecting shaft length.

5. Do at least one curve twice to test the repeatability of the device.

5.1.2 NIST Experimental Procedures for Beam Bending

The following experiments were performed at the National Institute of Standards and Technology (NIST): straightness errors and radial runout on the constant and variable shaft.

5.1.2.1 Straightness error setup for constant and variable shaft:

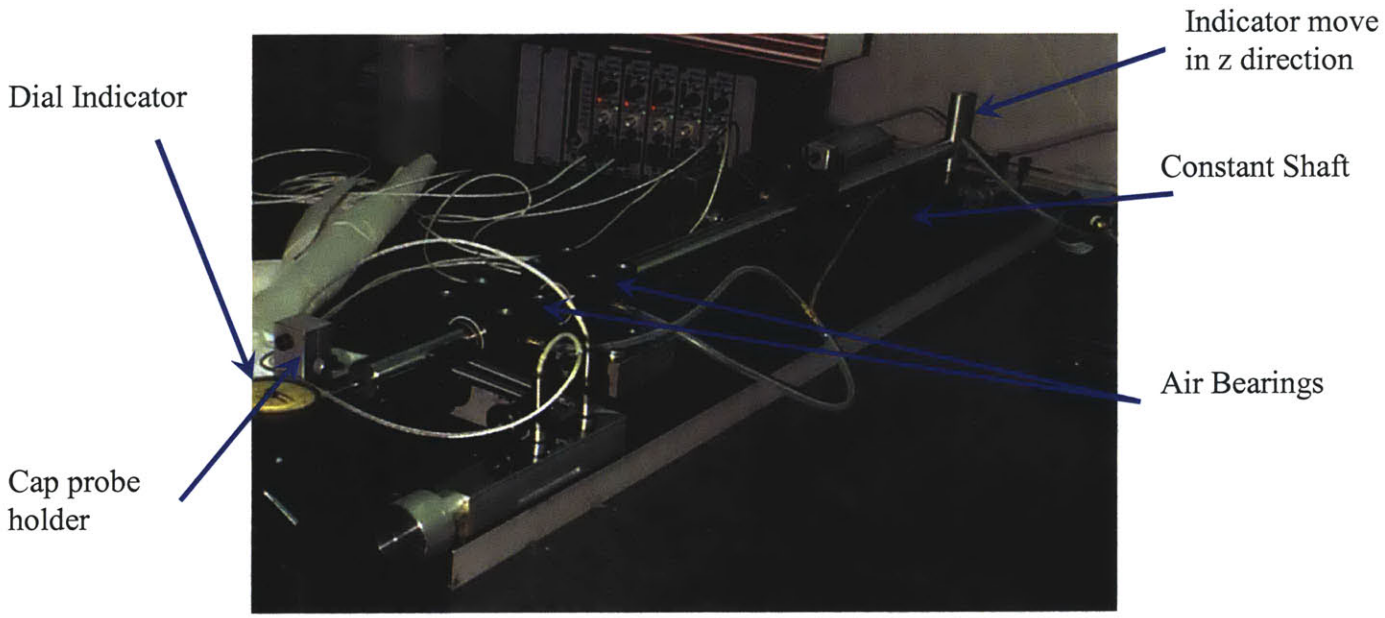

Figure 47: Overall set up of straightness error measurement.

1) Shaft through two air bearings currently set up with 60 psi running through the bearings.
2) Two capacitance probes 50 mm apart read a surface that is 1 in 10,000 smooth with a Ra value of 1 μm. This can be setup in two configurations
    a. Horizontal (Figure 48)
    b. Vertical (Figure 49)

    For the Horizontal direction the cap probes are placed to point down. This measures the yaw errors. For the Vertical direction, the cap probes are placed in a horizontal position. This position of the cap probes determines the pitch errors.

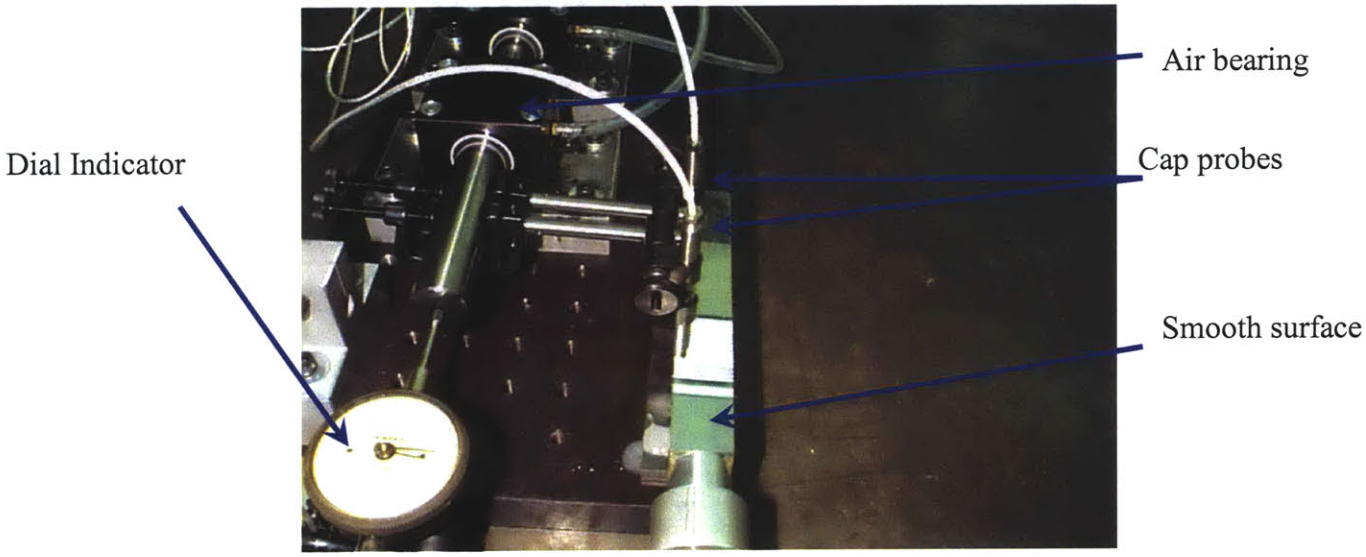

Figure 48: Horizontal straightness set up with cap probes in the vertical position.

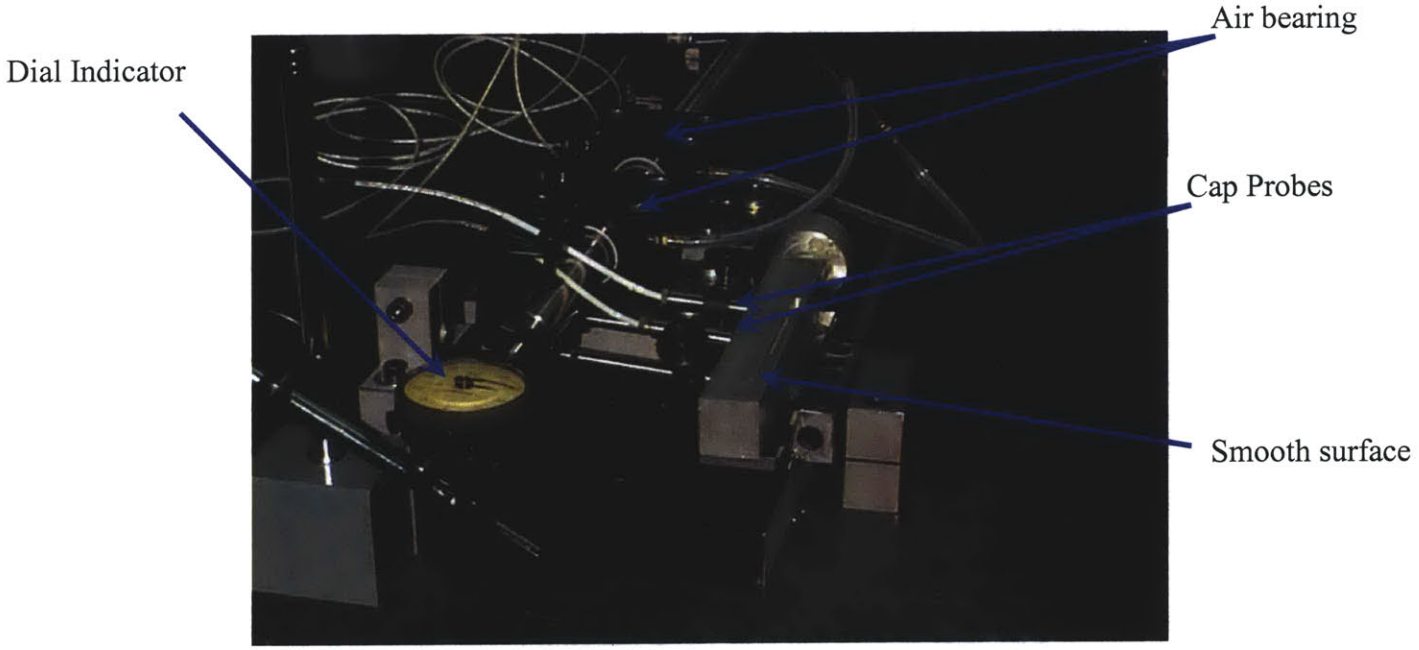

Figure 49: Vertical Straightness setup with cap probes in the horizontal position.

3) Run the cap probes up and down the surface to see if they can constantly read voltage within the cap probes range.
4) Once the cap probes can read the smooth surface, epoxy the surface down. 123 blocks were used to get the smooth surface to the height of the cap probes.
5) As a counter balance, because the cap probes were suspended like a lever on one side, two 123 blocks with a parallel bar between them was used as a guide when the shaft moved. This was done to keep the shaft from rotating and the cap probes horizontal or vertical (Figure 50)

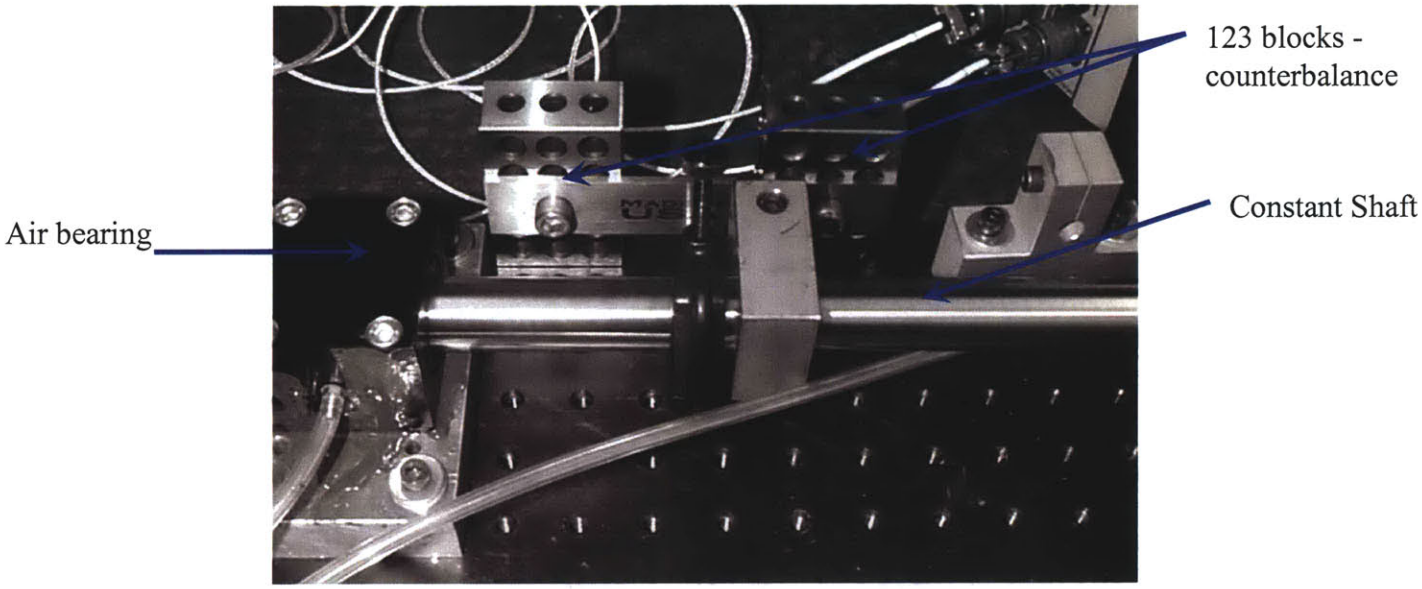

Figure 50: 123 Blocks help with counterbalance

6) Epoxy the 123 blocks down.
7) An indicator is set up at the end of the shaft and has a spring-loaded return. The indicators tip is positioned at the center of the shaft diameter. The total distance is 25 mm movement. (Figure 51)

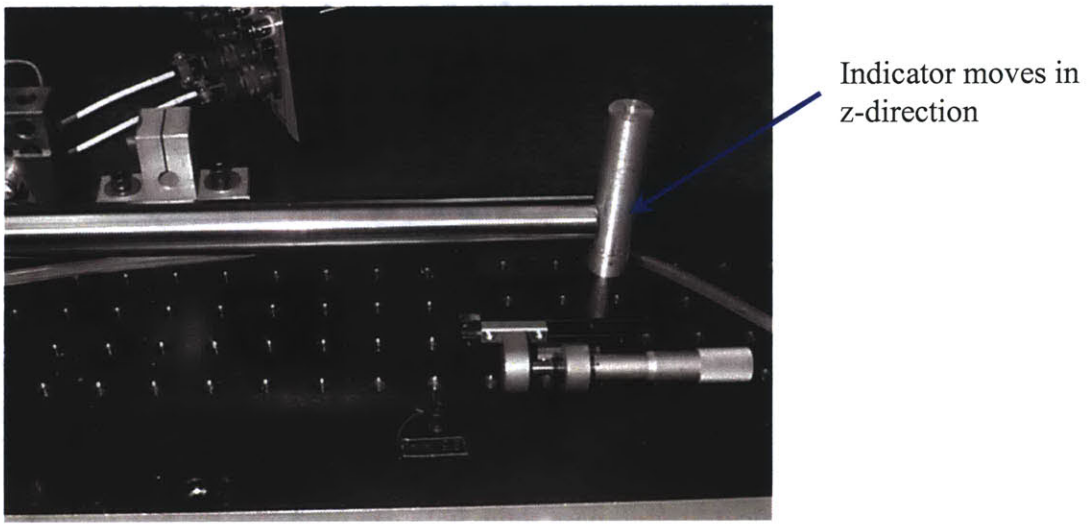

Figure 51: Indicator moves the shaft 25 mm in the z-direction.

8) Vary the spacing of the air bearings by 100, 150, 200, 250, and 300 mm. (Figure 52)

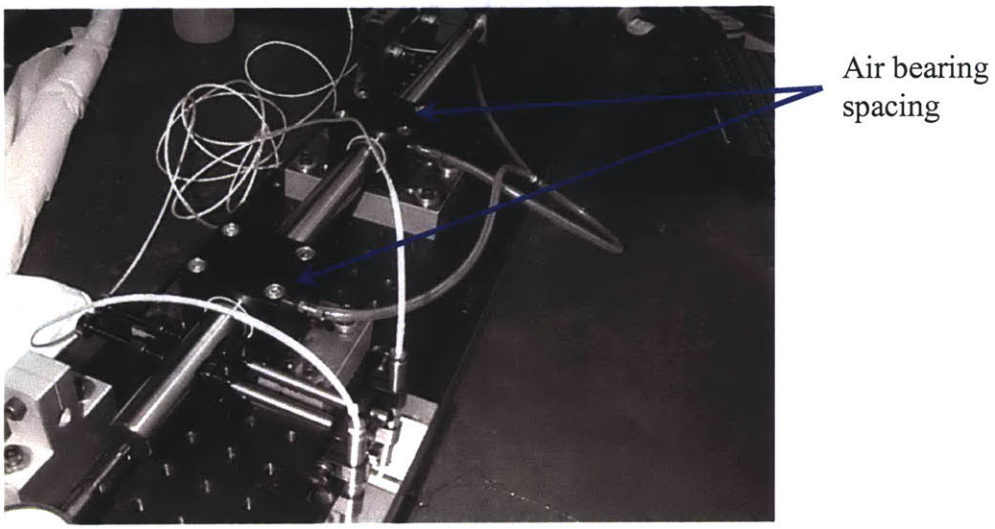

Figure 52: Air bearing spacing is varied in 50 mm increments

9) Record the results. Cap_probe.VI was used for this, Figure 53.

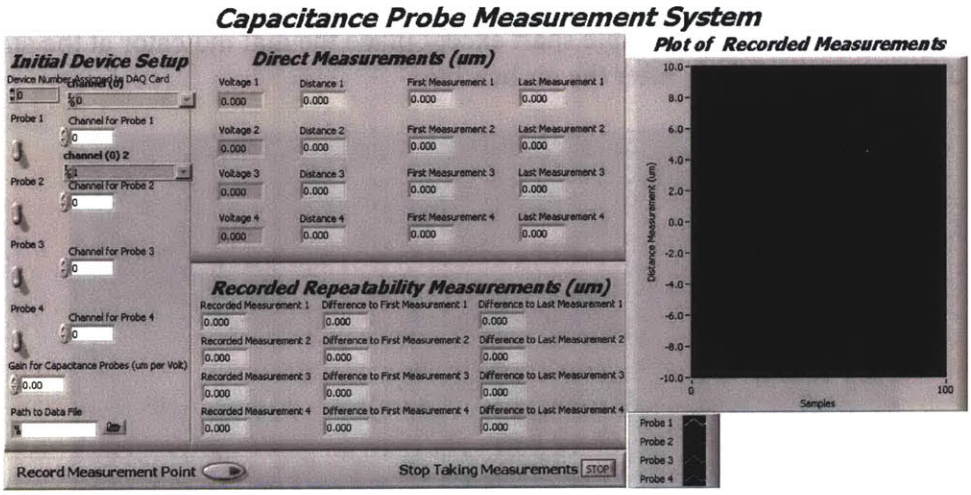

Figure 53: Snap-shot of what the VI looked like to record the voltage from the cap probes

10) Repeat the run three times before going to the next spacing.

5.1.2.2 Radial runout setup for constant and variable shaft

1) Align bearings so shaft runs smoothly.
2) Place a dial indicator along the shaft's center diameter, Figure 54.

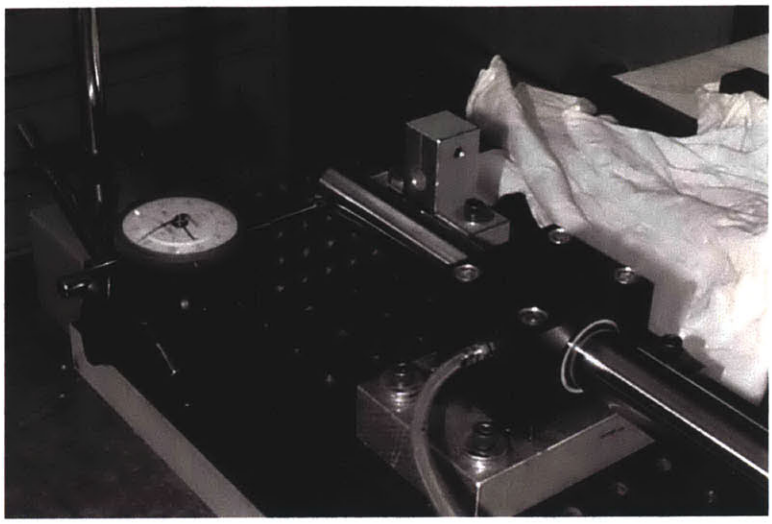

Figure 54: Constant shaft radial runnout

3) Put two blocks on both ends of the shaft to keep it from drifting while rotating the shaft.
4) Rotate the shaft to read the run out.
5) Vary the spacing between the air bearings by 100, 150, 200, 250, and 300 mm.
6) Record the readings.
7) Repeat procedure for variable shaft except place the dial indicator at the small diameter part of shaft, after the air bearing.

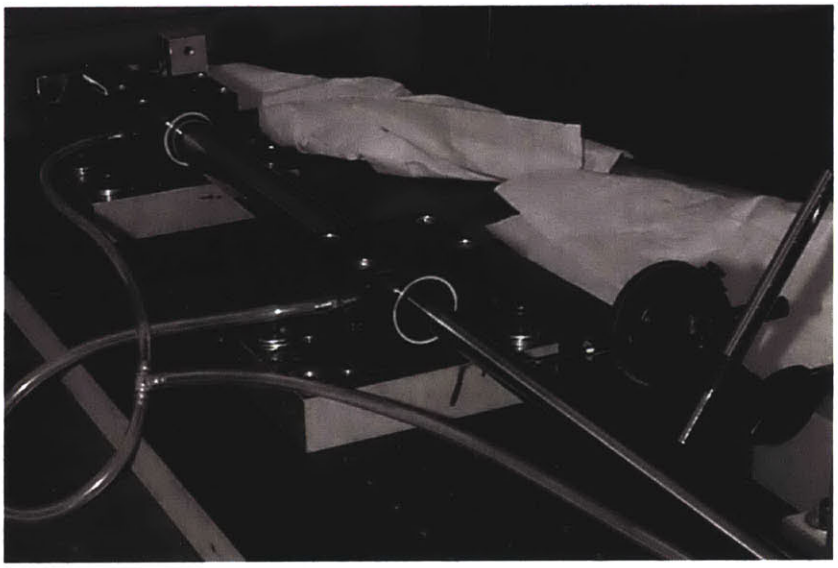

Figure 55: Variable shaft radial runnout

5.2 Capstan Experiments

Three experiments were conducted, determination of AE of the cable, cable to drum friction, and the torsional stiffness of the capstan drive. Each experiment will be discussed below.

5.2.1 AE value

Determining the effective modulus, Æ, of the steel cable entailed a section of cable, according to ASTM, was mounted and pulled to failure in an Instron™ tensile test machine. Refer to Figure 56 and for the procedure see ASTM's "Standard Tests Methods for Tension Testing of Metallic Material". Once testing was complete, the stress strain curve was produced and the effective modulus was calculated.

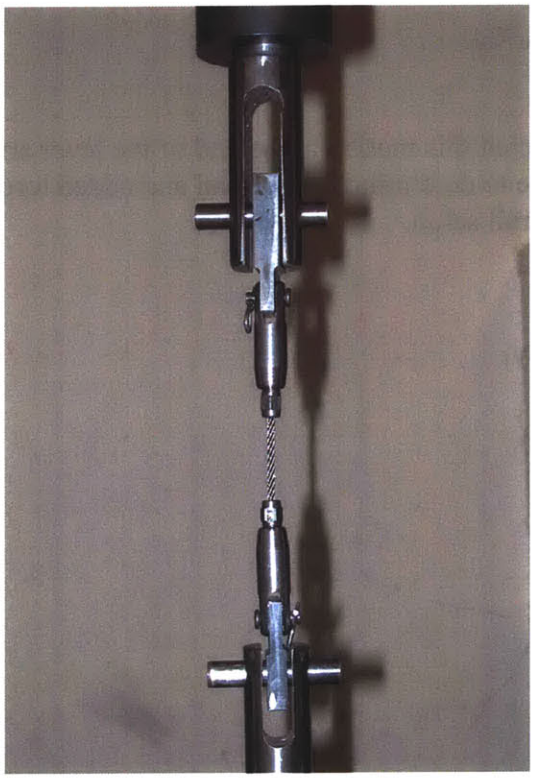

Figure 56: Cable segment in Instron™ tensile test machine.

5.2.2 Cable to drum friction

Calculation of the coefficient of friction between the steel cable and the aluminum drum was determined by cutting a piece of rope and sticking it to a plastic sheet. An aluminum plate was placed on top of the cable so as the plastic sheet was tilted, the angle was recorded until the aluminum sheet began to slip. This slip angle is equal to the coefficient of friction:

$$\mu = \arctan(\theta)$$

(117)

5.2.3 Torsional stiffness

The experimental system for determining the torsional stiffness of a capstan drive consisted of a 1.5 mm steel cable wrapped in a figure-eight pattern around two drums with diameters of 50 mm and 280 mm. The input drum was fixed as would be the case if a motor servo was loaded in position. Torque was applied to the output drum to simulate a load being applied. The rotation of the input and output drum were measured and the difference is due to the transmission compliance. To measure this rotation, a lever arm was attached to each drum's axis. As torque was applied to the output drum, any rotation encountered in the input drum was subtracted to give the net deflection of the cable.

$$\delta = \theta_{cable\_encoder} r_{output} - \theta_{lever} r_{input}$$

(118)

Capacitance probes detected this motion at the end of the lever arm. A load cell was spliced between the cable to determine the preload and added torque in the system. Figure 57 shows the overall setup.

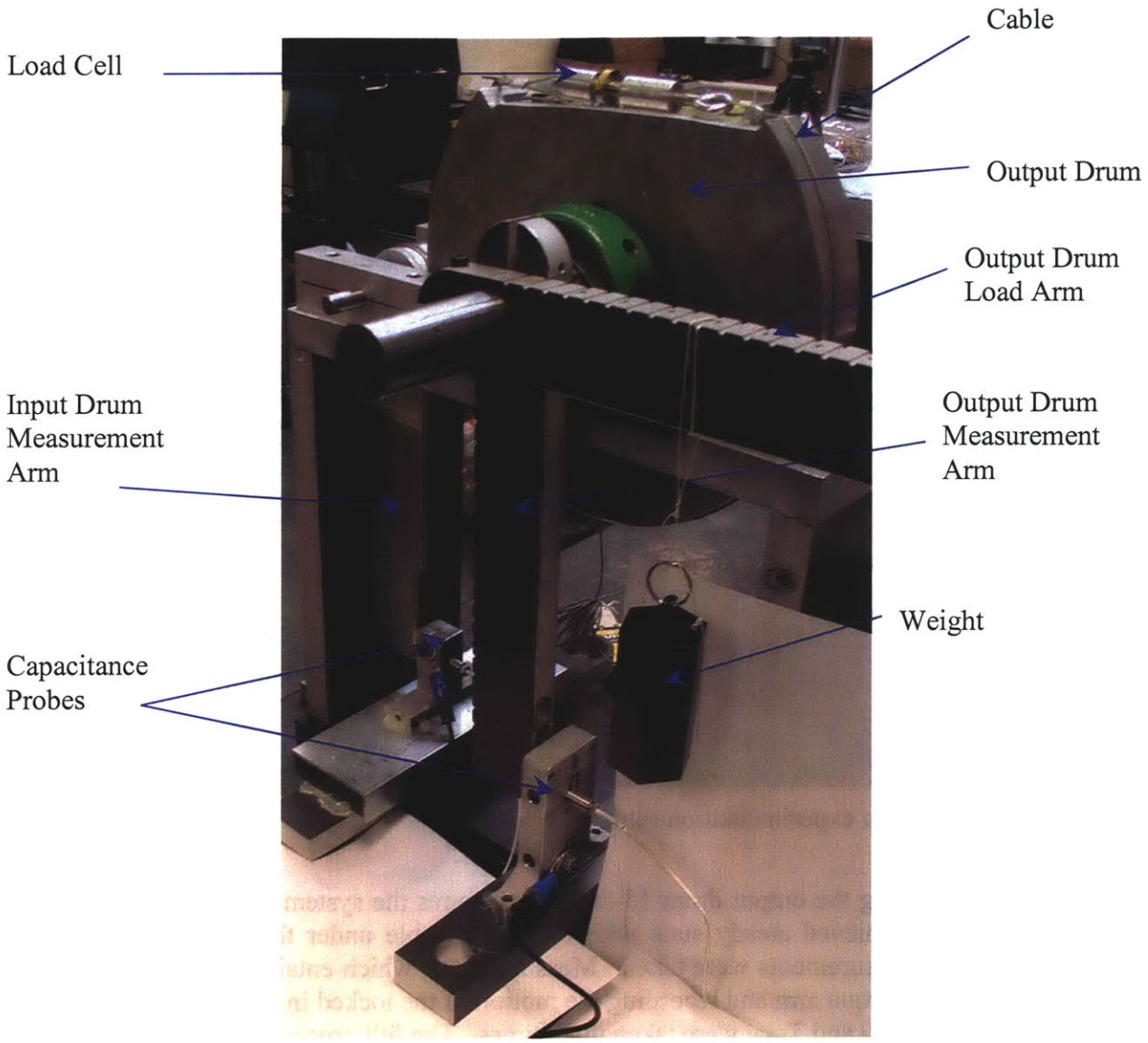

Figure 57: Configuration of the Capstan experimentation.

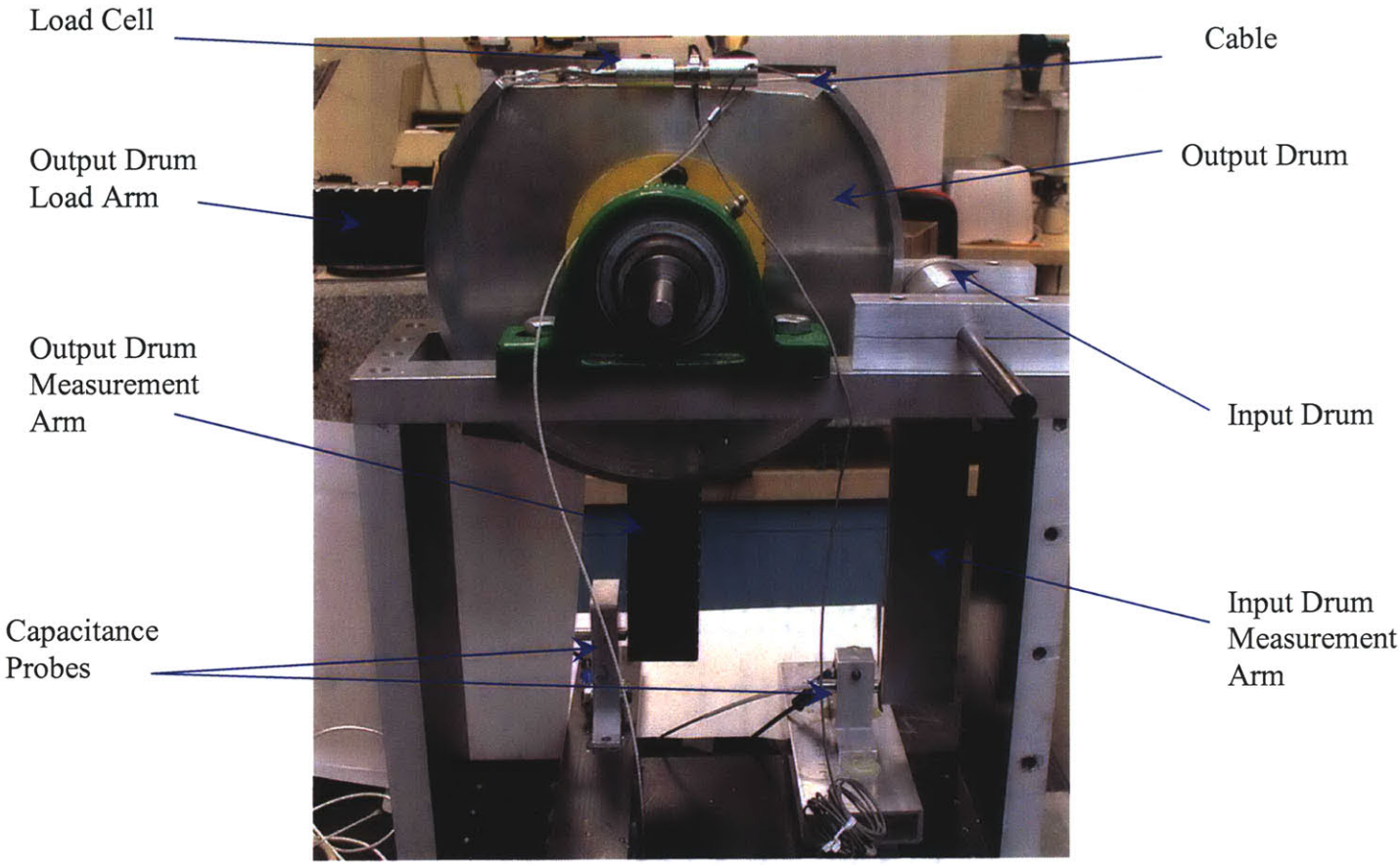

Figure 58: Capstan experimentation setup with load cell.

Once setup, rotating the output drum 15-20 times ensures the system runs smoothly and the system has achieved steady state with the entire cable under the preload tension, $T_{preload}$, before measurements were taken. Measurements, which entailed adding weights to the end of the torque arm and recording the motion of the locked input and output shaft and values of $T_{preload}$ and T_{load}, were taken three times. The full procedure was:

1. Wrap cable in a figure-eight pattern once around the input and output drums. Tighten the cable so there is a slight preload.
2. Rotate output drum back and forth 15-20 times.
3. Record initial reading of capacitance probes and load cell with no preload.
4. Tighten cable to desired preload and record readings from capacitance probes and load cell.
5. Add weight to the torque arm in increments of 1kg until cable starts to slip.
6. Record data from both capacitance probes for every 1 kg added and load cell.
7. Repeat two more times.
8. After third run, increase cable preload and repeat procedure starting from step 2.

5.3 Aerostatic Spindle Experiments

The spindle is capable of speeds up to 110,000 rpm and is designed to self clamp the tool [31] at speeds above 40,000 rpm. However, the capacitance probes can detect the speed of the spindle correctly up to 30,000 rpm given a 20 kHz DAQ card and 20 samples per

revolution. The rotation speed of the artifact above 30,000 rpm was determined by an oscilloscope since the spindle produces a pulse six times per revolution. The SEA program that was discussed in Chapter 3 was not used due to the limit of the DAQ card. Thus by finding the frequency from peak-to-peak of the impulses, the speed of the spindle was found. Even this method was crude in determining the error motion of the spindle because the tolerance of the sensor that gives off the 6 pulses per revolution is within two krpm Nevertheless, to obtain a preliminary performance indication, tests were run.

6 Results

The result from each calculation is described below. If the calculations only needed one value, that value was given in the Chapter 4.

6.1 Beam Bending Calculations

6.1.1 Straightness results of constant shaft

Horizontal direction

As the bearing spacing increased by 50 mm, the average straightness error decreased until a spacing of 200 mm was reached. After this spacing, the straightness error started to increase again. Table 13 shows the values and Figure 59 shows the graph.

Table 13: Horizontal straightness error

Spacing between air bearings (mm)	Cap Probe 1 straightness error (μm)	Cap Probe 2 straightness error (μm)
100	3.0	3.0
150	2.3	2.4
200	0.43	0.43
250	1.5	1.5
300	1.9	2.3

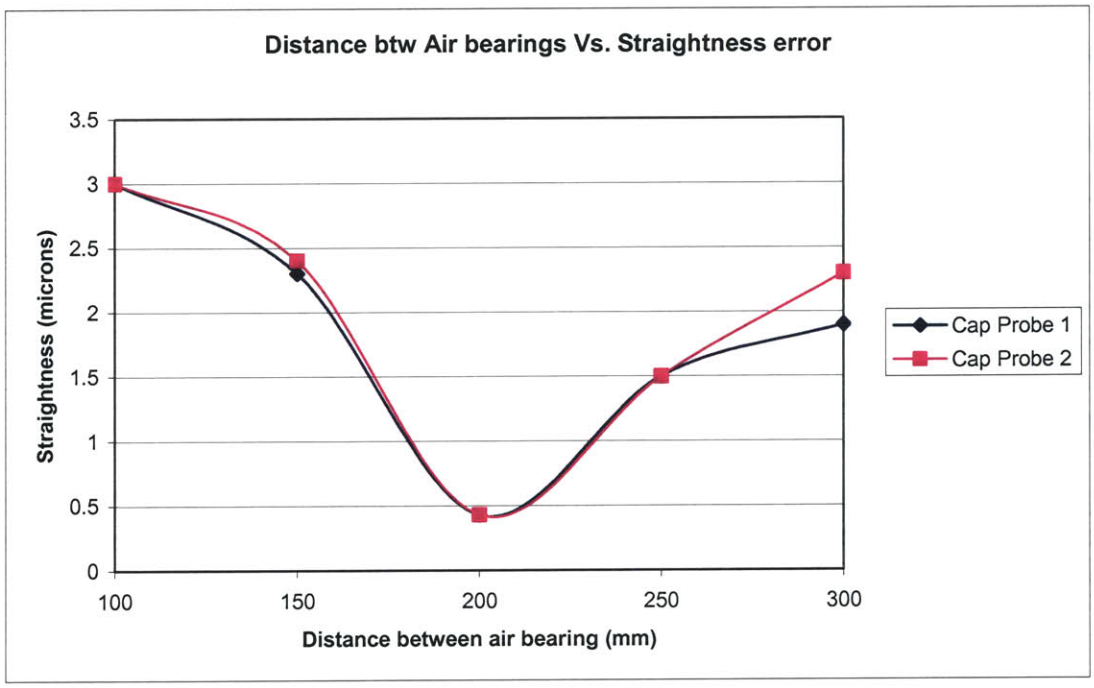

Figure 59: Horizontal spacing of air bearings vs. straightness error for 25 mm shaft.

Notice how the values read by each cap probe correlates to the same number. The standard deviation for each spacing is given in Table 14.

Table 14: Horizontal direction standard deviation

Spacing between air bearings (mm)	Cap Probe 1 standard deviation	Cap Probe 2 Standard deviation
100	1.0	1.0
150	0.97	0.75
200	0.09	0.08
250	0.19	0.18
300	0.56	0.32

When comparing Table 13 and Table 14, as the straightness error increases, the standard deviation increases as well. This implies the values of each measurement had low repeatability. Repeatability is the error in trying to obtain the same result over and over again. Thus there must have been other factors affecting the measurement. These factors are due mostly to the alignment of the air bearings. Without proper alignment the shaft will not move as smoothly. In addition when the air bearings are not aligned, a torque is produced on the end of one bearing from the force induced by pushing the shaft through the off-center air bearing. Thus the cap probe tilts and is closer to the surface than supposed to be. Thus each cap probe is rotated to a different position than before. These are the angular errors and they are given in Table 15.

The alignment with the 200 mm spacing has good repeatability and small straightness errors associated with it. This can also imply the 200 mm spacing is optimal for this configuration.

Table 15: Horizontal Radial error

Spacing between air bearings (mm)	Cap Probe 1 radial error (rad)	Cap Probe 2 radial error (rad)
100	2.7e-4	3.7e-4
150	1.2e-4	1.9e-4
200	1.3e-4	2.17e-4
250	1.6e-4	2.2e-4
300	1.8e-4	1.7e-4

Figure 60 shows the radial error verses the spacing between the air bearings. Notice how the two cap probes have similar curves. The difference in the curves is present between spacing 150 - 300 mm because the air bearings were not aligned properly.

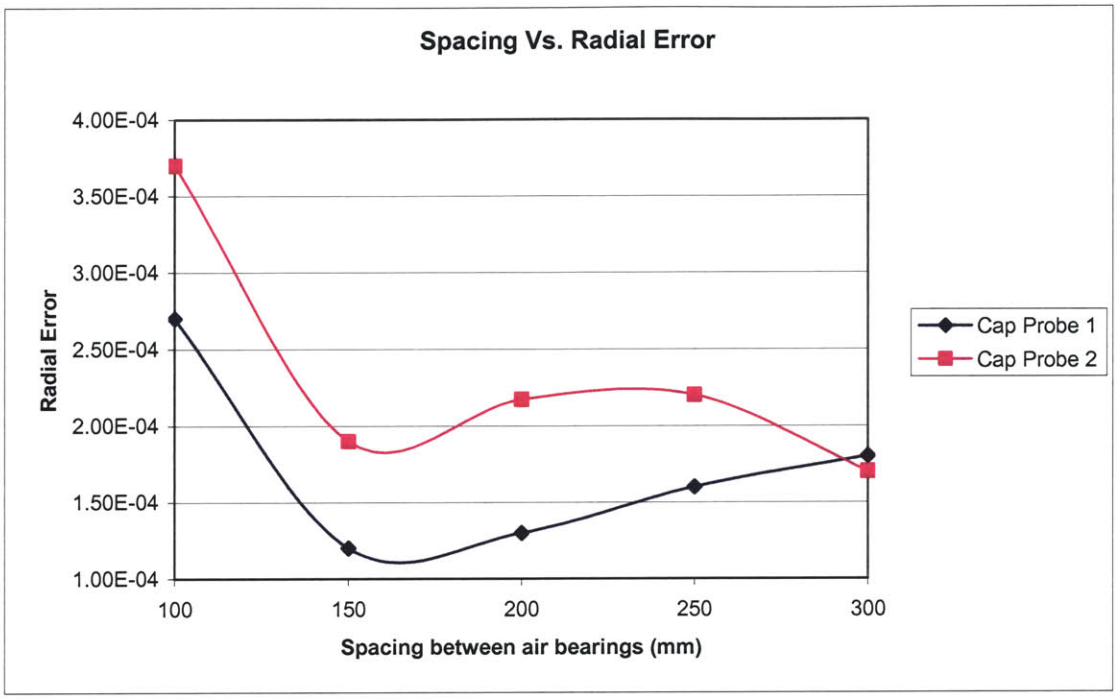

Figure 60: Horizontal Spacing vs. error in the radial direction.

Vertical Direction

The vertical direction produced smaller Straightness errors, on the order of .1 microns. Table 16 gives the straightness error for cap probes 1 and 2 and Figure 61 gives the plot of the air bearing spacing versus the straightness error.

Table 16: Vertial straightness error.

Spacing between air bearings (mm)	Cap Probe 1 straightness error (μm)	Cap Probe 2 straightness error (μm)
100	0.057	0.15
150	0.14	0.12
200	0.027	0.0039
250	0.026	0.010
300	0.028	0.0064

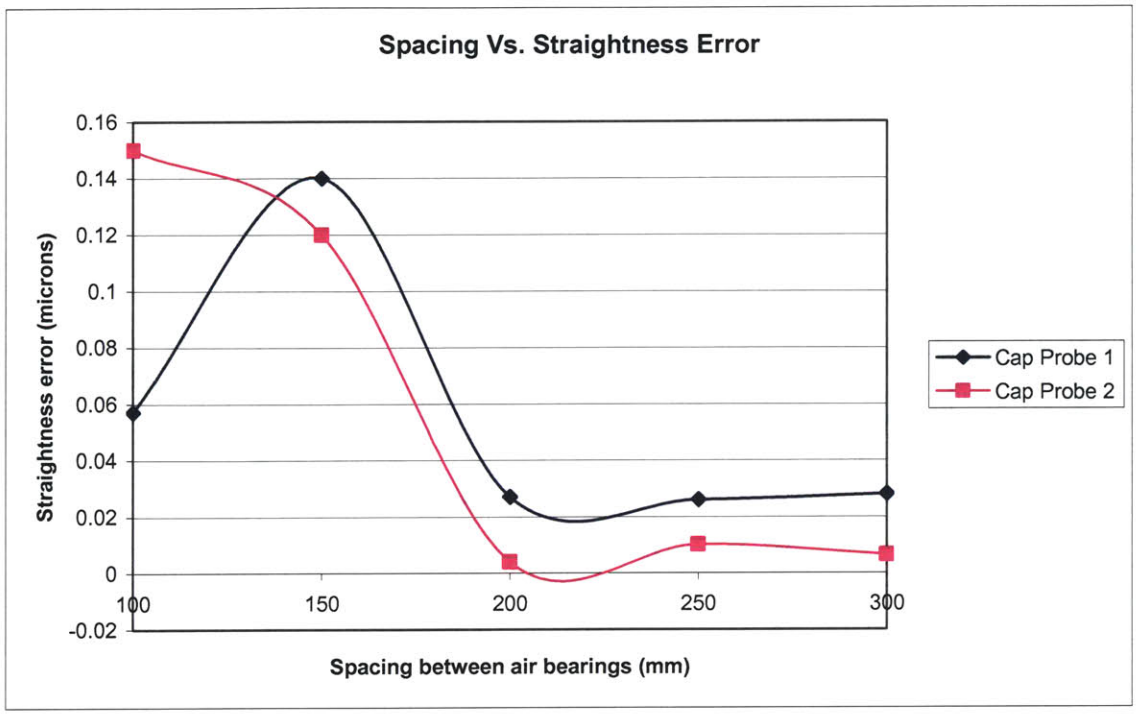

Figure 61: Vertical Spacing vs. Straightness Error

Notice the two cap probes start at two different straightness errors for a spacing of 100 mm. Reasons for this error are improper alignment of the air bearings and/or mirror had dirt particles on it.

The straightness error is smaller in the vertical direction but cap probes 1 and 2 do not give the same result in each spacing like in the horizontal case. There is an 85 % difference in the case where the distance between the air bearings is 200 mm. Looking at the radial errors accounts for part of the difference.

The repeatability of each run is higher than that of the horizontal direction. Table 17 gives the standard deviation for the vertical direction. Notice how each cap probe for the same spacing has a similar standard deviation.

Table 17: Vertical Standard deviation

Spacing between air bearings (mm)	Cap Probe 1 standard deviation	Cap Probe 2 Standard deviation
100	0.18	0.12
150	0.21	0.23
200	0.33	0.34
250	0.080	0.078
300	0.018	0.027

Table 18: Vertical Radial error.

Spacing between air bearings (mm)	Cap Probe 1 radial error (rad)	Cap Probe 2 radial error (rad)
100	2.0e-4	1.7e-4
150	9.5e-5	2.8e-4
200	2.0e-4	3.3e-4
250	1.9e-4	4.2e-4
300	2.4e-4	4.7e-4

The radial error for each bearing spacing is given in Table 18. Overall the error is small. Figure 62 shows the plot of spacing between the air bearings versus radial error.

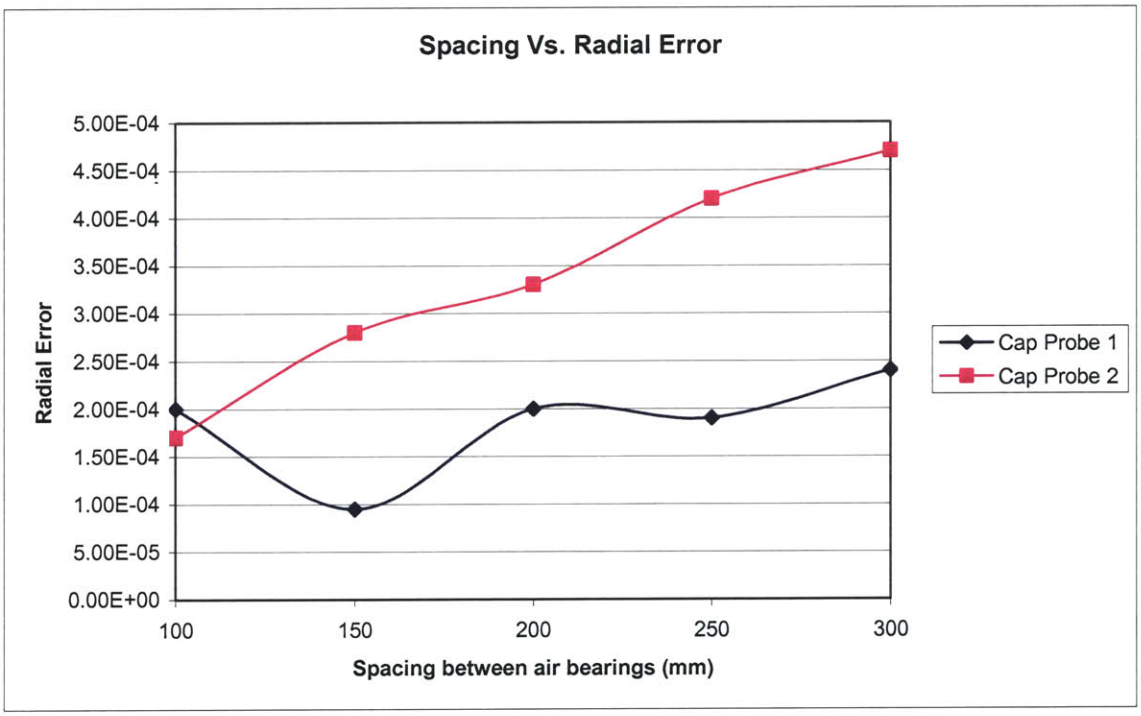

Figure 62: Vertical Spacing vs. Radial Error

Both curves increase as the air bearing spacing increases, except for spacings of 150 and 250 mm. This is probably due to improper alignment of the air bearings.

6.1.2 Radial Runout for constant and variable shaft

Constant shaft Diameter

The radial runout values are given in Table 19. Each bearing spacing was consistent. The average value was 40 μm.

Table 19: Constant Shaft Radial Runnout.

Spacing between air bearings	Radial runout (μm)
100	40
150	40
200	40
250	40
300	40

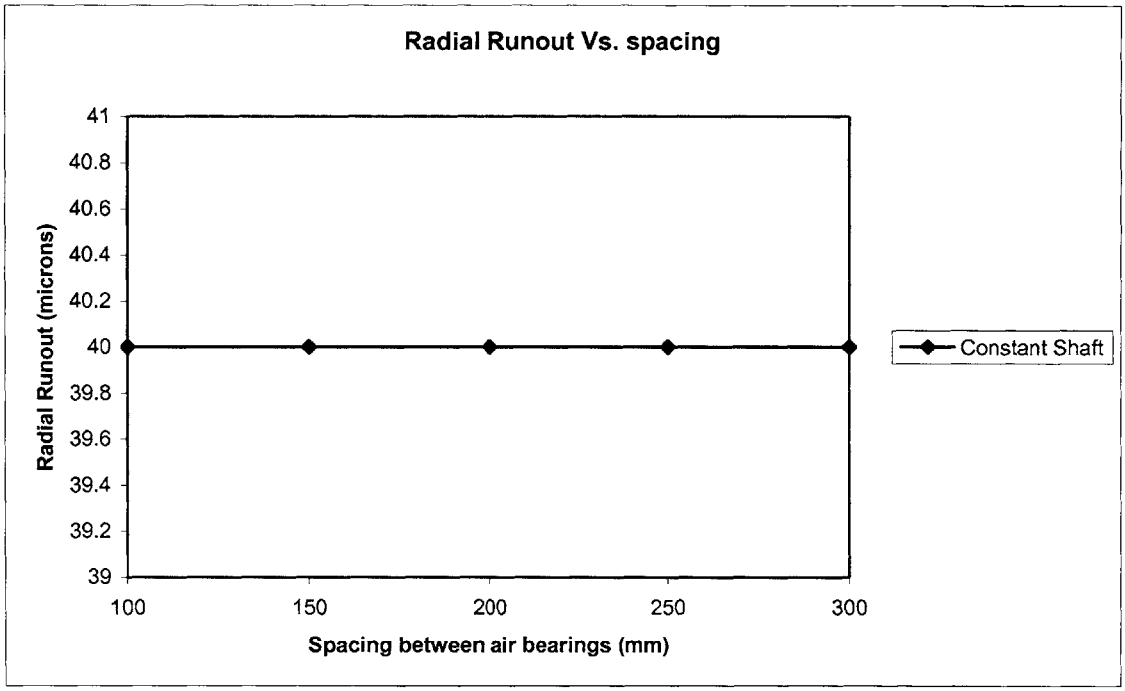

Figure 63: Constant Shaft Radial Runnout vs. Spacing.

Figure 63 shows the plot of the radial runout versus the spacing of the air bearings. There was no change in the plot because the radial runout remained at 40 microns for each spacing. Thus the runout has little dependence on the air bearing spacing.

Variable Shaft Diameter

The radial runout for the variable shaft was different from the constant shaft by 91%. This dramatic increase was due to the fabrication of the shaft; there was a slight bow in it. The radial runout is given in Table 20.

Table 20: Variable Shaft Radial Runnout.

Spacing between air bearings (mm)	Radial runout (μm)
100	444
150	400
200	400
250	400
300	300

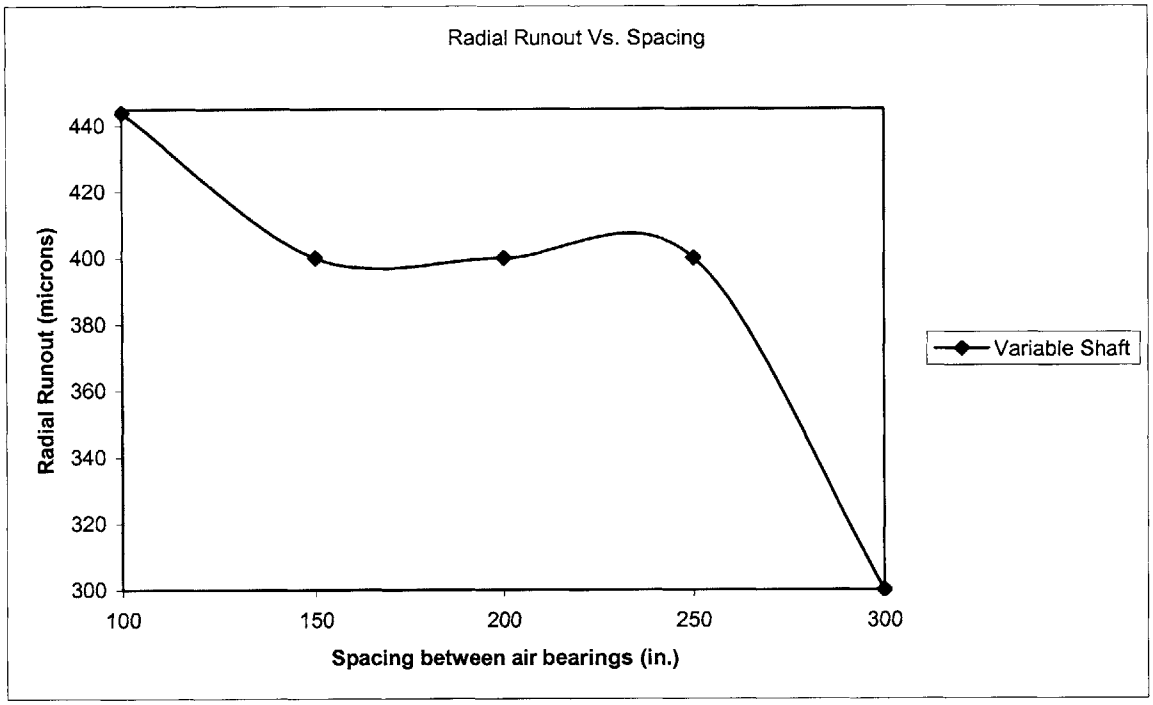

Figure 64: Variable Shaft Radial Run out vs. Spacing.

In conclusion from Figure 64, as the spacing between the air bearings increase, the wobble or radial run out will decrease. This is due to as the distance between the air bearings increases, the support becomes closer to the wobble and dampens it out.

6.1.3 Conclusion of beam error experiments

The air bearings, with proper placement, decrease errors, but the alignment of the bearings is crucial. Without proper alignment, the air bearings can add additional error into the system. Even if the air bearings are properly aligned, the error is still large if the shaft is improperly manufactured so the variable shaft has a slight bow in it, as was experienced in our case.

The experiments do correlate with the beam bending theory given in chapter 4. As the results and theory show, the optimal distance between the air bearings to reduce errors

and allow proper alignment of them is 200 mm. However, the added cost, complexity, and size outweigh the modest potential performance increase.

6.1.4 Bow in variable shaft in beam bending experiments

If air bearings were to be used to support the shaft, a coupling is modeled between it and the ballscrew-spline shaft. This coupling action could be obtained by using a small shaft.

How the coupling was determined:

The torsional and axial stiffness are used to obtain equations of the smaller shaft that would act as the coupling. The equation of torsional stiffness and axial stiffness is given below

$$K_{Torsion} = \frac{DI}{L}$$

$$K_{Axial} = \frac{AE}{L} \tag{119}$$

Equating the above equation to a rod with smaller diameter and length, then solving for its length and diameter, produces a rod of diameter of 6 mm and length of 13.4 mm.

Not only does the coupling take out the wobble due to the bow, but also the error reduction is substantial because the coupling allows for the deflection to be expended in the smaller section of the shaft. Thus the deflection is greatest at the coupling and not the tip of the shaft. The following ProMechanica deflection analysis graph portrays this.

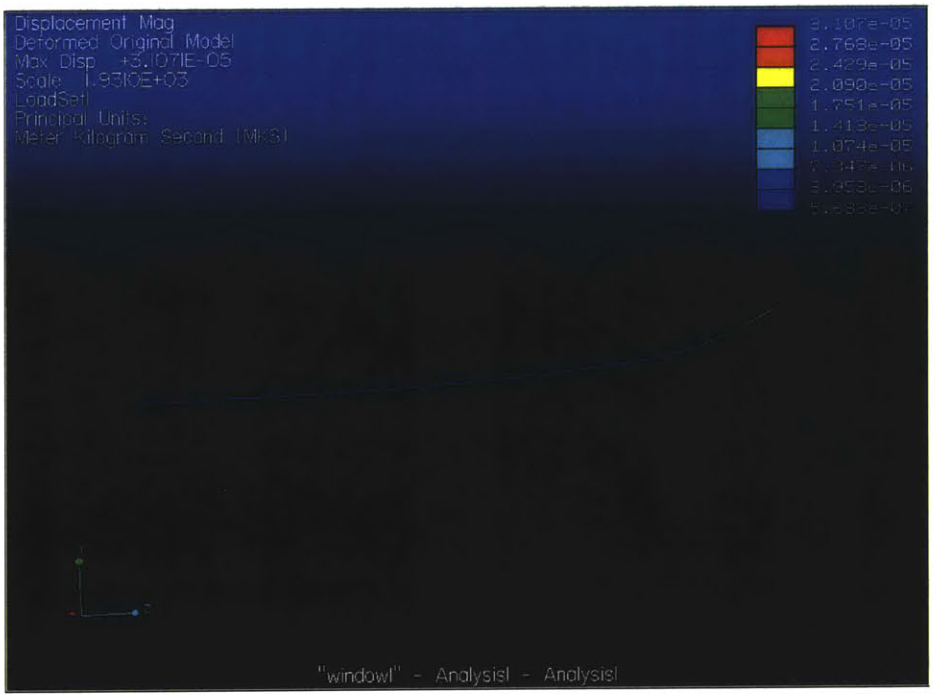

Figure 65: ProMechanica Model of shaft deflection.

The deflection where the bushings reside is 3.25E-3 m and the deflection at the spindle tip is -3.05E-6 m. That is three orders of magnitude difference. If the connector is increased to 12 mm diameter, then the deflection at the bushing decreases to 4.75E-4 m but the deflection at the spindle end remains the same, -3.048E-6 m. Thus the coupling connector makes a difference by 1000 times. Therefore, this coupling reduces the deflection more than the constant and variable shaft.

In conclusion since the shaft is already small, the air bearings were taken out and only the shaft was used which made the design compact and reduce cost. .

6.2 System Natural Frequency

Since the belt drive only gives a 13 Hz natural frequency, two different drive mechanisms were looked into, the capstan drive and dual pinion. To see the calculations on the stiffness, see the section on Motor determination in Chapter 3. These two stiffnesses were on the order of 10^4 for both the capstan and dual pinion. This increases the natural frequency to 46 Hz, which is better than the belt drive.

A low natural frequency is not desirable because of ease of excitation. The 46 Hz is acceptable because the spindle reaches excitations higher than this.

6.3 Capstan Drive

6.3.1 Effective modulus

The effective cable modulus, Æ, is determined by loading the cable to 25% of its rated tensile strength and noting the displacement of the load.

$$F = \frac{Æ}{L}\delta$$

$$\Rightarrow Æ = \frac{FL}{\delta} \tag{120}$$

where L is the original length of the testing sample.

6.3.2 Cable Seasoning

The cable has two values for Æ, one before proofloading and one after. Proofloading is the process of stretching the cable beyond the cable void. Figure 66 shows these two areas. Proofloading the cable is necessary to remove the constructional stretch in the cable, so that when Æ is found, only the actual stretch of the wire is seen. The different regions in the cable, before and after proofloading, are found by pulling a cable until failure and recording the stress and strain of the specimen refer to Figure 66. After the proofloading value is found the cable is then stretched and cycled to this desired force. A test sample of 467 mm long was cycled 10 times to 1kN which determined if proofloading is beneficial as shown in Figure 67. The figure concluded proofloading removes the stretch and determined Æ of the 1.5mm cable to be 2.4×10^5 N.

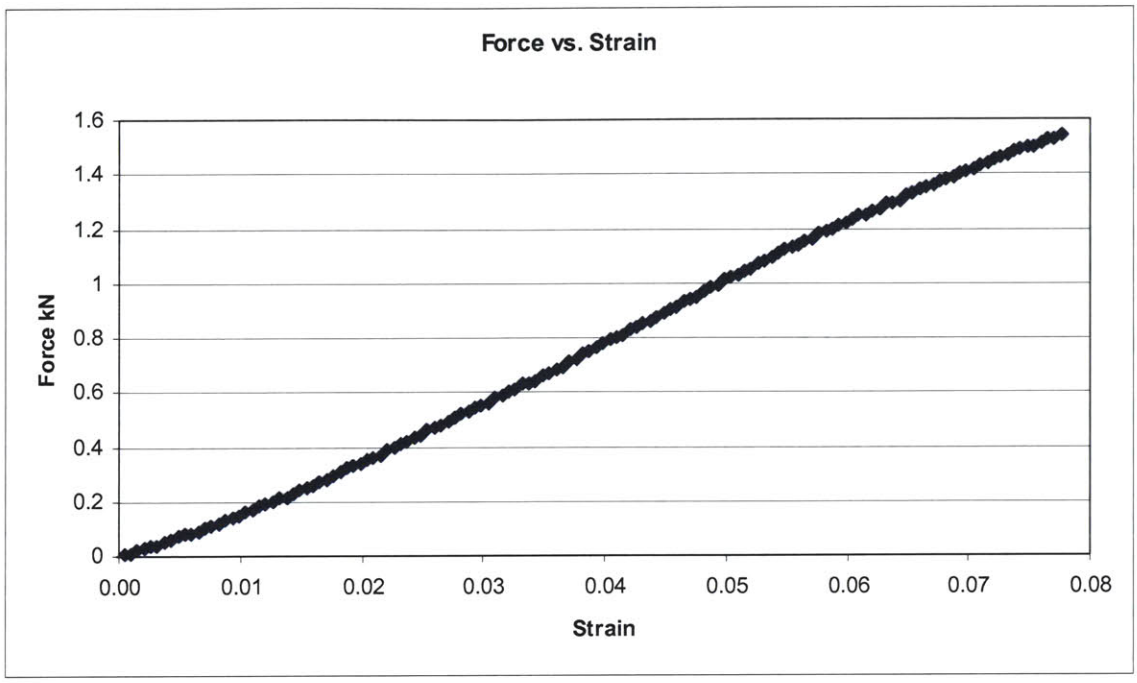

Figure 66: Applied force versus strain, displacement divided by original length, for the 1.5 mm diameter cable.

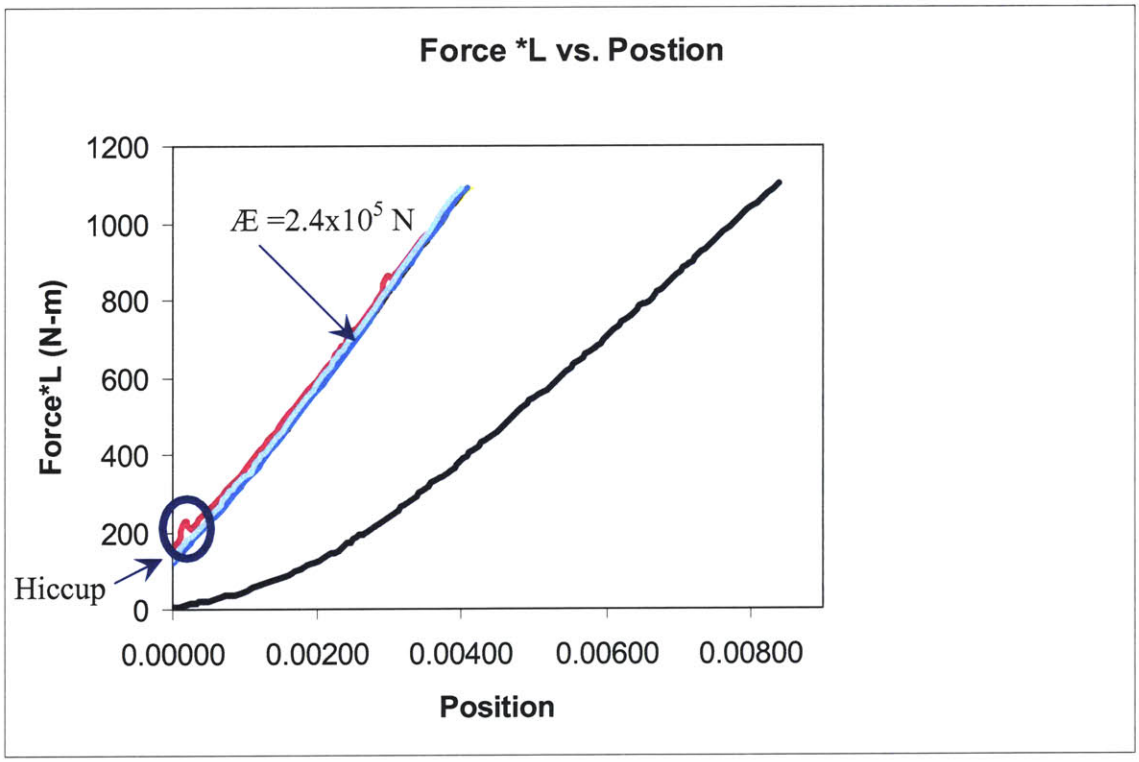

Figure 67: Cycling of a 15mm cable to a value of 1 kN results in a Æ value of 2.4×10^5 N.

In Figure 67, the cycling goes from 175 N – 1000N and not from 0 N because an initial preload was decided to remain in the cable. Lastly the hiccup on the pink line was due to the cable adjusting itself on the Instron™ machine and was not saw after the second cycle.

6.3.3 Cable to drum friction

The coefficient of friction was determined to be 0.22 given the angle the aluminum sheet started to slip at was 13 deg.

6.3.4 Torsional Stiffness

Measurements were run with Æ equal to $2.4x10^5$ N for a 1.5 mm cable. Initial results gave the torsional stiffness of the capstan drive as $4.0x10^4$ N-m/rad for a $T_{preload}$ of 44 N and $5.8x10^5$ N for a $T_{preload}$ of 111 N. Theoretically the torsional stiffness matched with the experimental values differing by 77%. This is due to an improper determination of the coefficient of friction and error in the value of Æ. Figure 68 - Figure 71 displays different preload and the accompanying torsional stiffness for theory and measured values. If μ is decreased to .05, theory and experimental values agree within 10%. Further investigation of cable to drum friction is recommended.

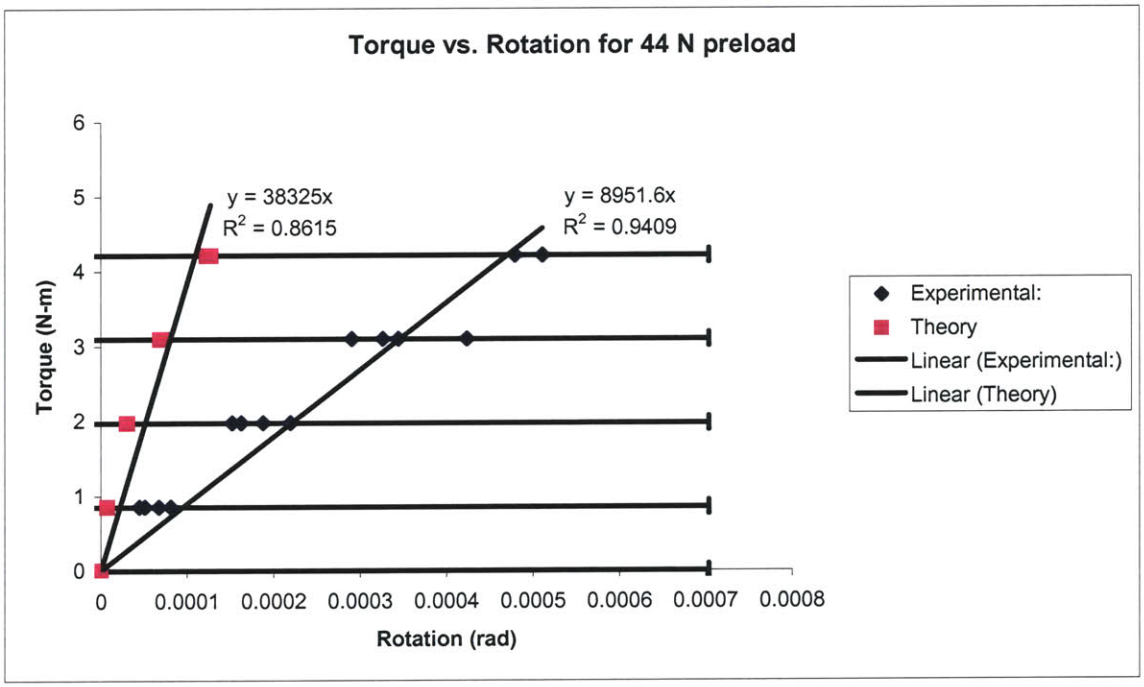

Figure 68: Torque vs. Rotation for a 44 N preload.

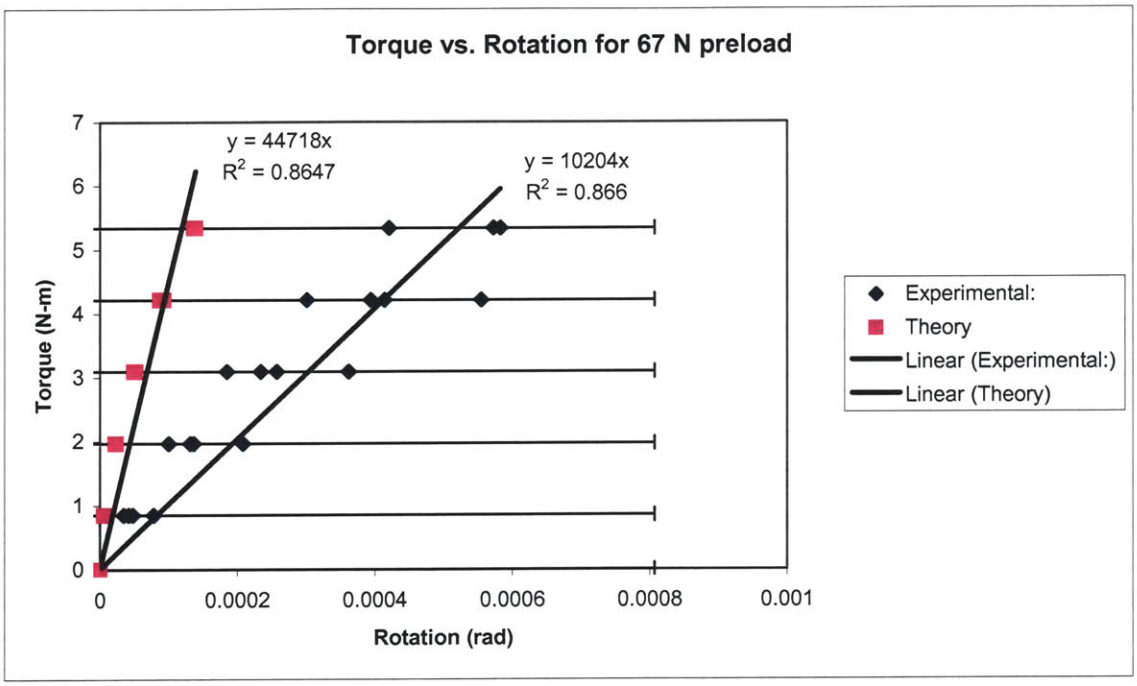

Figure 69: Torque vs. Rotation for a 67 N preload

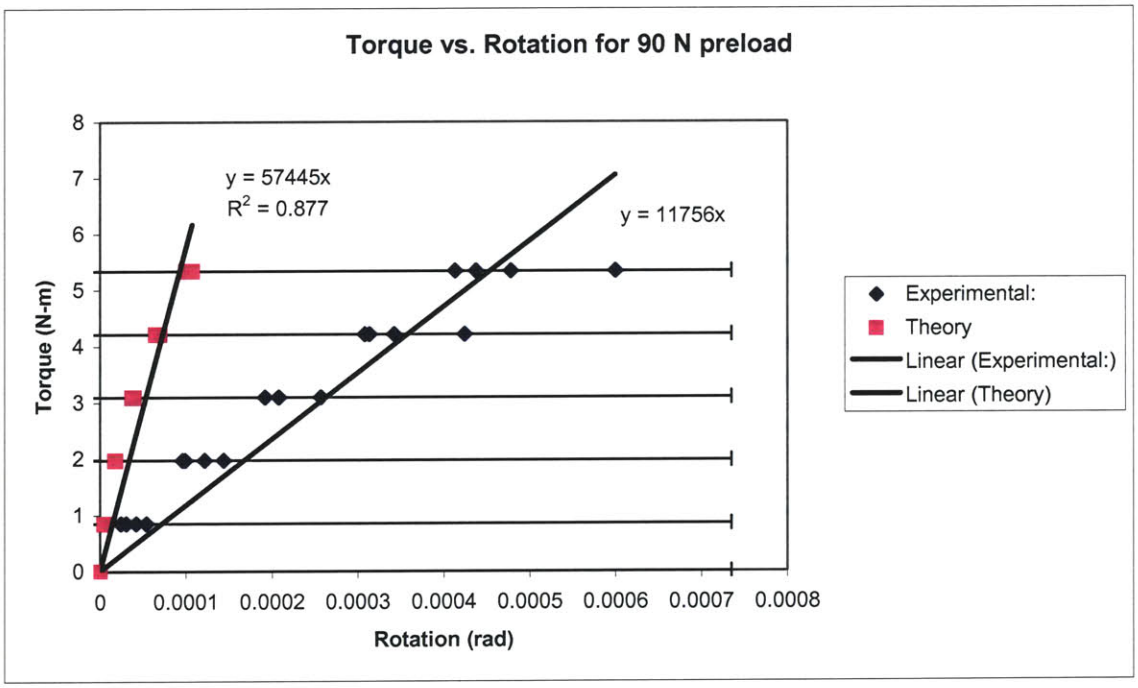

Figure 70: Torque vs. Rotation for 90 N preload

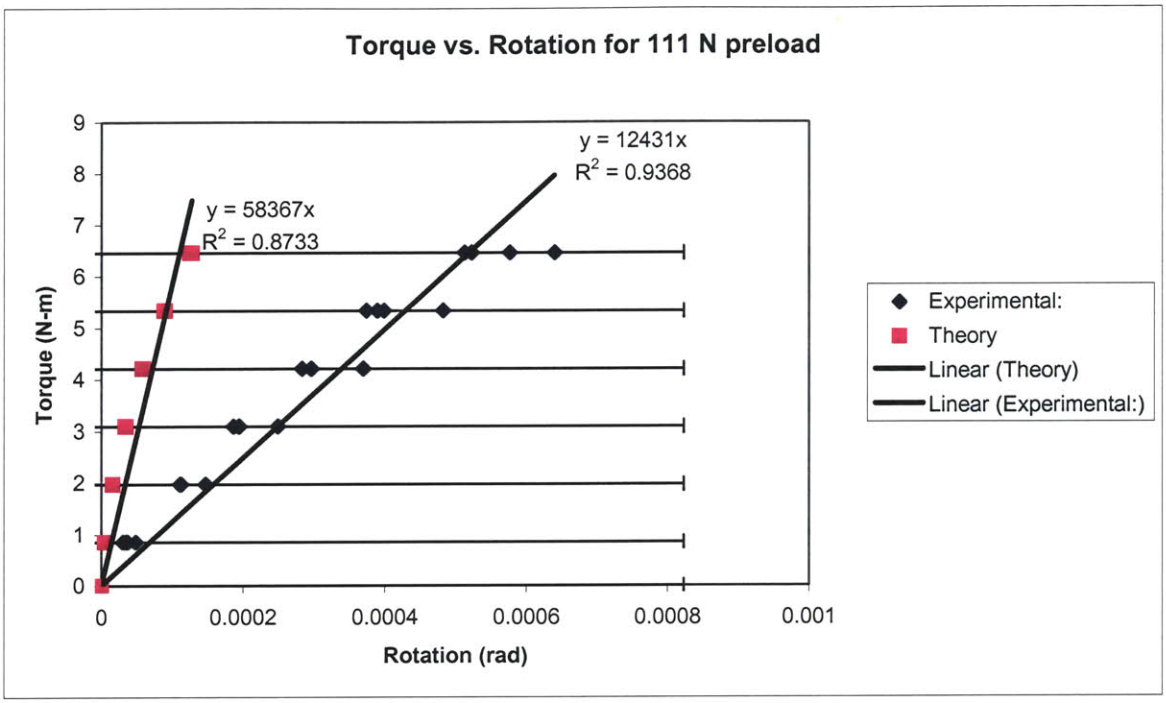

Figure 71: Torque vs. Rotation for 111 N preload.

Data from the 1.5 mm cable diameter was compared to the 3mm diameter. The same experiments were run on a 7x19 stranded 3 mm diameter cable with the Instron™ machine and stiffness measurement as for the 1.5 mm diameter cable. This determined Æ and torsional stiffness of the cable. The goal was to find the correlation between two different sized cables. Unfortunately the 3 mm cable did not produce relatable results because according to the Machinery's handbook, the maximum cable diameter of the drum must be 40-45 times the cable diameter [32]. For the 1.5 mm diameter cable the input drum fits into this range but the 3 mm cable does not. A drum diameter of 135 mm should be used. Further investigation is recommended.

Based on these experiments, the recommended design equation for the torsional stiffness is:

$$K_{Torsion} = \frac{D_{output}^{\ 2} K_{total}}{4} \tag{121}$$

where K_{total} is given in equations (107) - (109).

6.3.4.1 Sensitive parameters

Four cases will be discussed in determining the sensitive parameters to the torsional stiffness equation of a capstan drive. As K_{total} is replaced by its value, the overall equation is:

$$K_{Torsion} := \mu \cdot A \cdot E \cdot D_o^2 \cdot \frac{\left(T_{preload} \cdot D_o \cdot T_{Load} + 2 \cdot L_{free} \cdot \mu \cdot T_{preload}^2 + T_{preload} \cdot D_i \cdot T_{Load} - 2 \cdot L_{free} \cdot \mu \cdot T_{Load}^2\right)}{\left[\left(D_o \cdot T_{Load} + 2 \cdot L_{free} \cdot \mu \cdot T_{preload} + 2 \cdot L_{free} \cdot \mu \cdot T_{Load} + D_i \cdot T_{Load}\right) \cdot \left(D_o \cdot T_{Load} + 2 \cdot L_{free} \cdot \mu \cdot T_{preload} - 2 \cdot L_{free} \cdot \mu \cdot T_{Load} + D_i \cdot T_{Load}\right)\right]} \quad (122)$$

Taking the partial derivative with respect to $T_{preload}$, T_{load}, μ, D_{output} (Do in the above equation), and L_{free} will be discussed below.

Sensitivity of $T_{preload}$

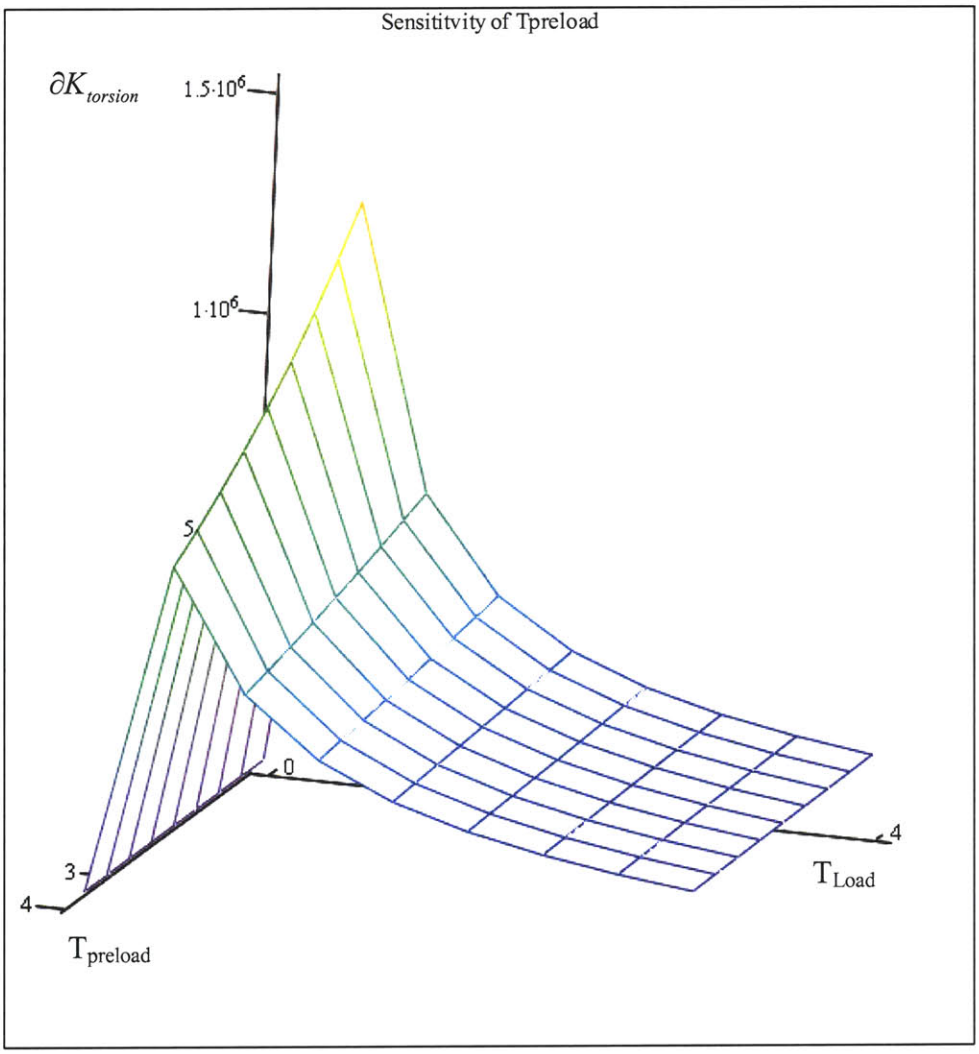

K_p

Figure 72: Sensitivity with respect to $T_{preload}$

Preload is sensitive around zero and has a higher stiffness at that point as well. As the preload is increased, the stiffness decreases linearly. As preload and the load increase the torsional stiffness decreases exponentially. Thus $T_{preload}$ is a sensitive parameter.

Sensitivity of T_{load}

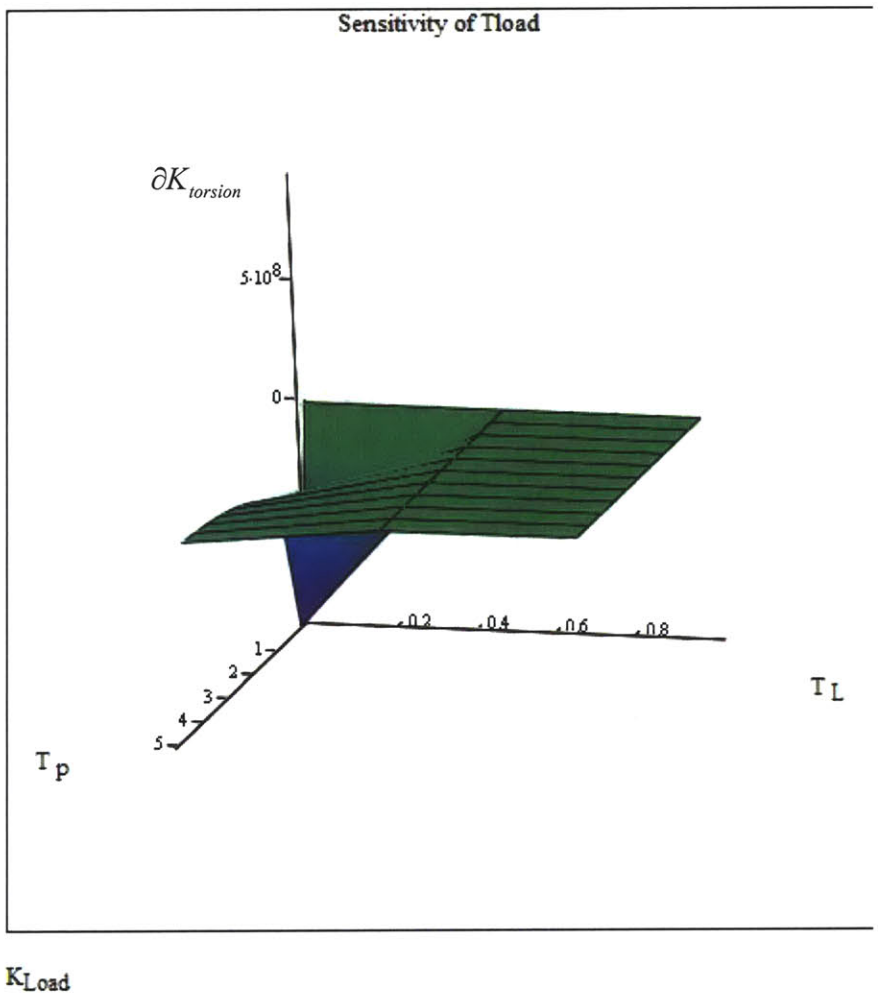

Figure 73: Sensitivity of T_{load}.

T_{load} is constant with the partial of $K_{torsion}$, but $T_{preload}$ is changing. Figure 73 displays the only term that greatly has an affect of $\partial K_{torsion}$ is $T_{preload}$.

Sensitivity of μ

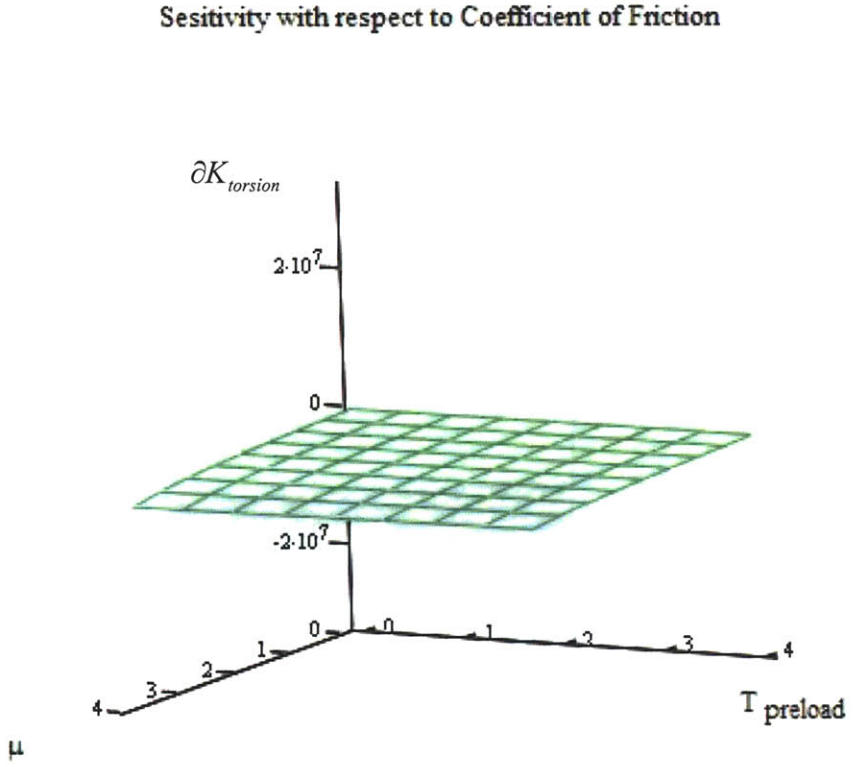

Figure 74: Sensitivity of torsional stiffness equation with respect to the coefficient of friction.

Figure 74 displays as the coefficient of friction and preload increase, the torsional stiffness of the drum has no affect given a value of 50 N for the T_{load}.

Sensitivity of D_{output}

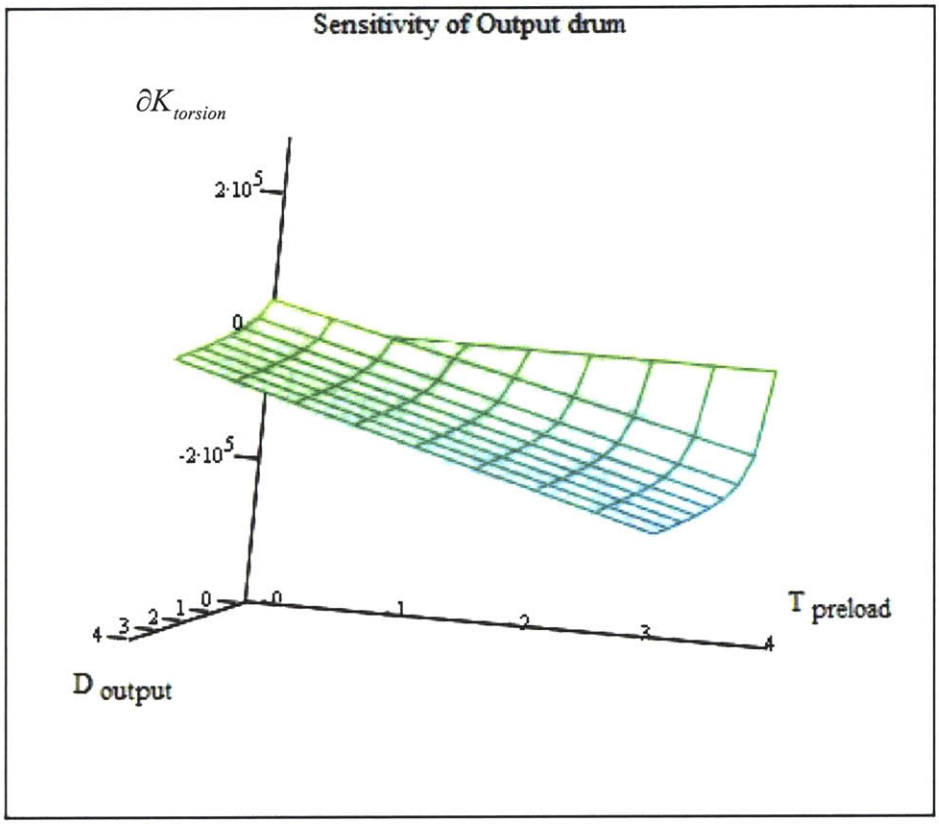

Figure 75: Sensitivity of D_{output} in the torsional stiffness equation.

As the output drum increases, the partial of the torsional stiffness remains constant as does the $T_{preload}$ term for a given T_{load} = 50N. When both of those values, $T_{preload}$ and D_{output} increase the partial of the torsional stiffness decreases which means $T_{preload}$ and D_{output} affect torsional stiffness, but not as much as $T_{preload}$ alone as shown in Figure 72.

Sensitivity of L_{free}

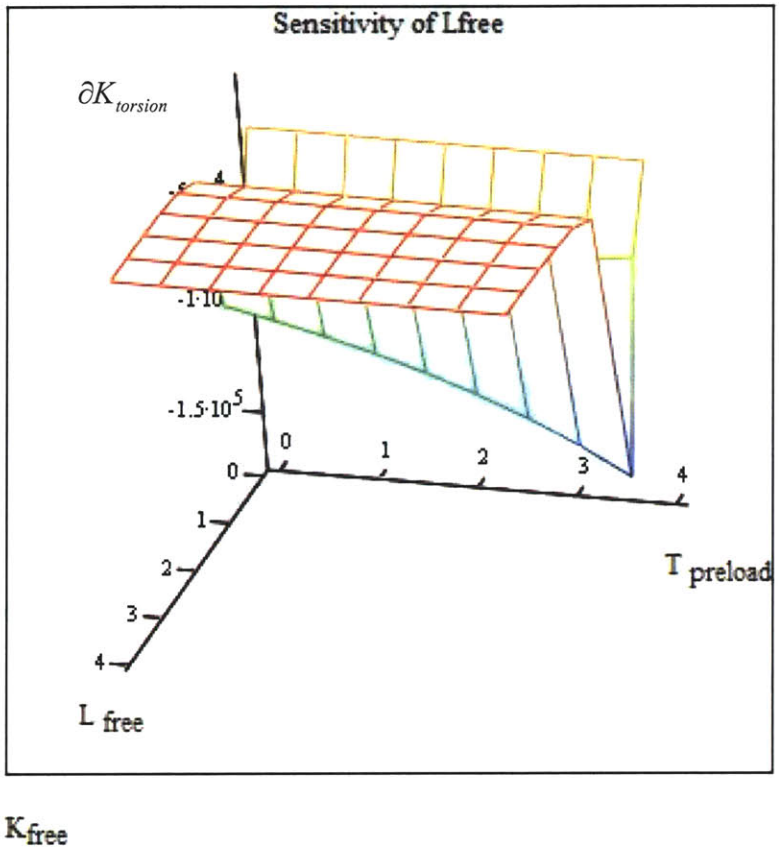

Figure 76: Sensitivity of L_{free} with respect to the partial of the torsional stiffness.

L_{free} is constant, except when it is 0, a point of irregularity. Tpreload behaves as described above, but it does not increase as much as in Figure 72 because T_{load} is given as 50 N.

6.4 Aerostatic Spindle Results

The results from these measurements, setup shown in Figure 77, display as the speed of the spindle nears 62,000 rpm a structural resonance occurs. This is evident by the excess error motion detected by the capacitance probes. As stated above, even though they do not give the exact value after 30,000 RPM, the capacitance probes were used to see if the distance from the spindle increased, decreased, or remained the same. After these two speeds are reached, the capacitance probes became off center and needed to be recalibrated. From this, it is apparent a structural resonance occurred and this speed should be avoided when machining.

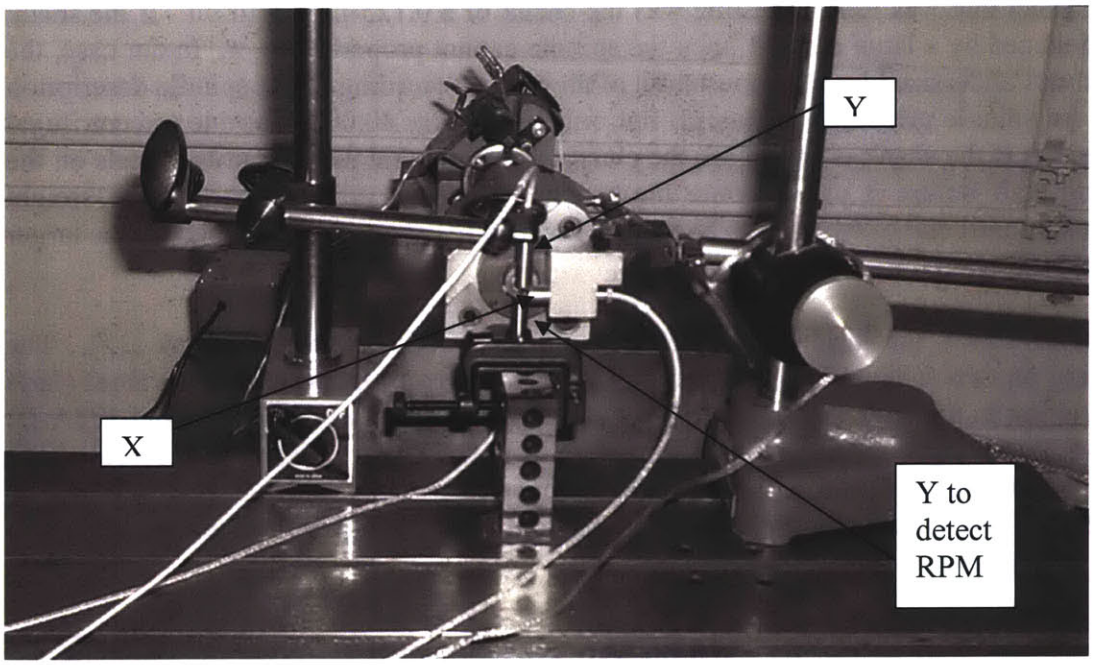

Figure 77: Aerostatic test setup showing placement of capacitance probes: X, Y, and speed of spindle up to 30,000 rpm. Spindle was mounted on grinder base.

The clamping mechanism of the artifact introduces some error in the measurement if it is not to size. The artifact itself of the spindle must be $0.125^{-0.0001}_{-0.0003}$ inch. If not, the artifact will become off-center when rotated. See Figure 78 for an example polar plot, but the large error is due to the spindle not gripping properly onto the artifact.

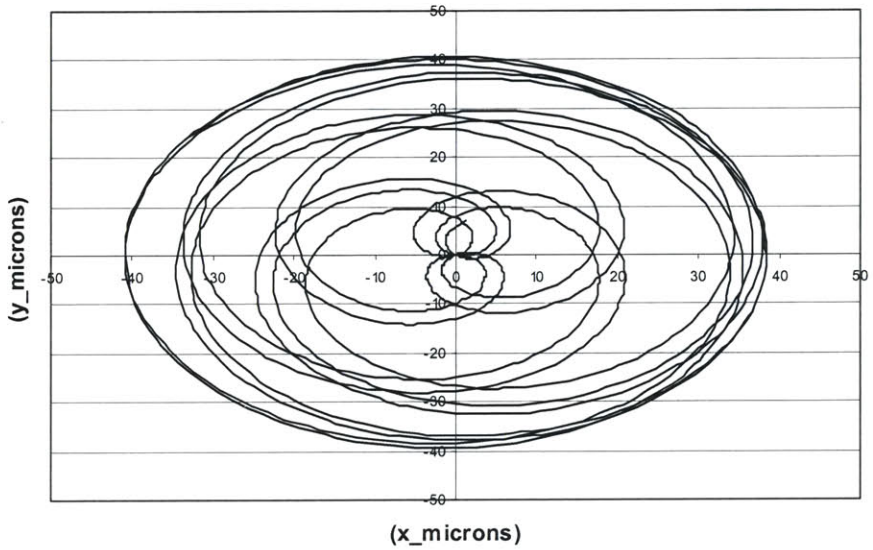

Figure 78: 1000 RPM polar of an off-center artifact.

The artifact that was used in testing was the shank of a 0.125-inch drill bit. If the shank is undersized by a large amount, then the spindle cannot properly grip it. In our case, the shank was undersized by one thousandth of an inch. According to the spindle description [31], the spindle gripping mechanism not only grips after 40,000 rpm due to centrifugal forces, but if the shank is too small, the clamping weight that moves outward rests on the bearing wall before it clamps onto the shank. Thus the gripping part of the weight recedes in until one of two things happen: it rests on the shank or is stopped by the larger weight resting on the bearing wall.

Figure 79 shows the location of the weights (162A-D, 172A-D) and shank (12). The gripping part (160 and 170) clamps onto the shank in two places, one in the front (160) and another in the back (170). Each grip is separated by flexures (164A-D and 174A-D) and has four weights. As the weights are spun, it is exposed to a centrifugal force, pivots about a ring flexure (165 and 175), and is moved outwards which makes the gripers which are lighter, clamp onto the shank. This is what gives the drill bit enough torque to machine material.

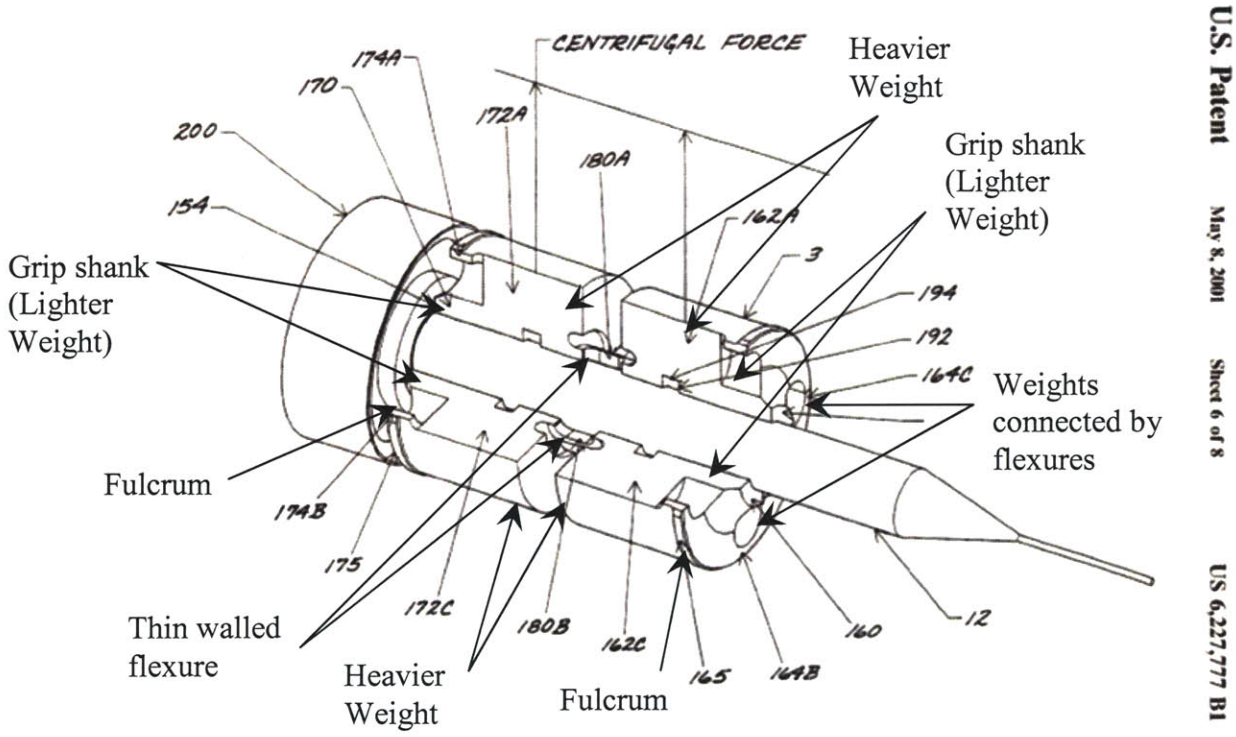

Figure 79: Centrifugal chuck of the aerostatic spindle [31].

6.5 Overall machine[8]

The performance characterization of the prototype MesoMill included: assessment of the geometric errors associated with the linear motion of the spindle and the rotary and linear motion of the ball-screw spline transmission mechanism (at the workpiece), as well as errors in the critical alignment between the axes, refer to Figure 80. The results from measuring the horizontal straightness, the vertical straightness, the pitch and yaw errors of the ball-screw spline motion are shown in Figure 81 - Figure 84. The measurements were performed using two capacitance probes offset by 25 mm in a holder attached at the location of the work piece. The machine was programmed to move 60 mm forward, then reverse 60 mm, while the capacitance probes measure deviations with respect to a straight edge. After the straight edge artifact error is determined by the reversal method, the artifact error is subtracted from the measured results. Using two offset probes, one can measure an angular error while simultaneously measuring the straightness error. The pitch error is measured with the vertical straightness and the yaw error is measured with the horizontal straightness.

The output of the analog capacitance probe is digitized by the motion control board. By using this interface, the motors shaft position and the capacitance probe outputs are simultaneously sampled. This eliminates the problems of synchronizing data collection on multiple instruments with the motor shaft position.

Table 21: Error results from the MesoMill experimentation setup.

	Error	Measurement uncertainty	Coverage factor, k
Vertical Straightness	0.30 μm	0.030 μm	2
Horizontal Straightness	0.54 μm	0.030 μm	2
Yaw	0.62 arc-seconds	0.2 arc-seconds	2
Pitch	1.8 arc-seconds	0.2 arc-seconds	2

[8] Adapted from the paper by Damazo, B., Donmez, A., and et al. *Performance Evaluation of a Prototype Machine Tool for Machining Meso-scaled Parts.* Published in the Proceedings of the 18th American society for Precision engineering Annual Meeting. Portland, OR, 2003.

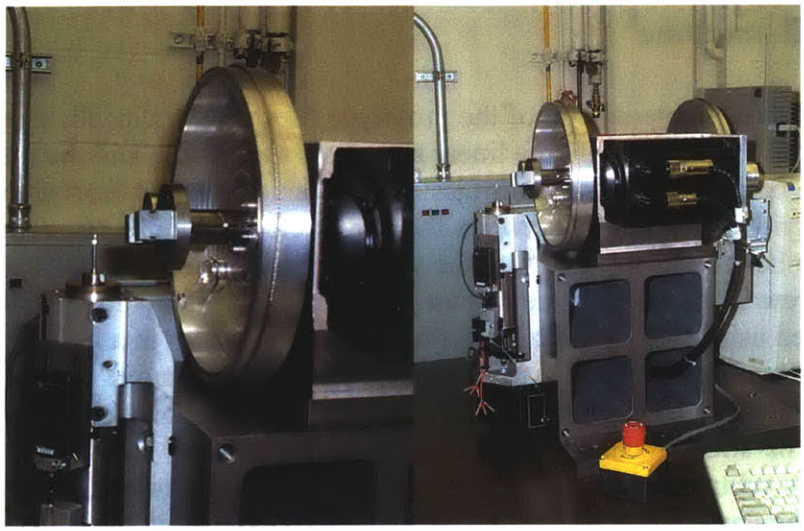

Figure 80: Photos of the prototype three axis rotary milling machine tool

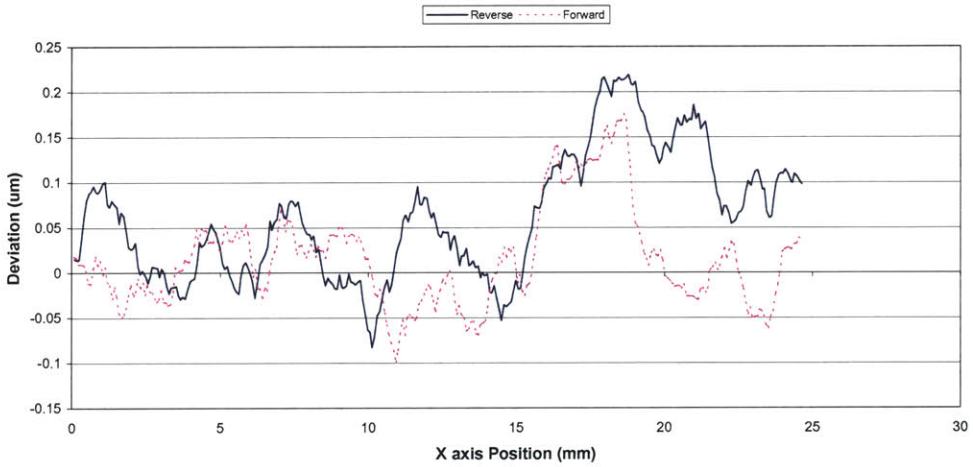

Figure 81: Prototype machine's vertical straightness error measured at the work piece location.

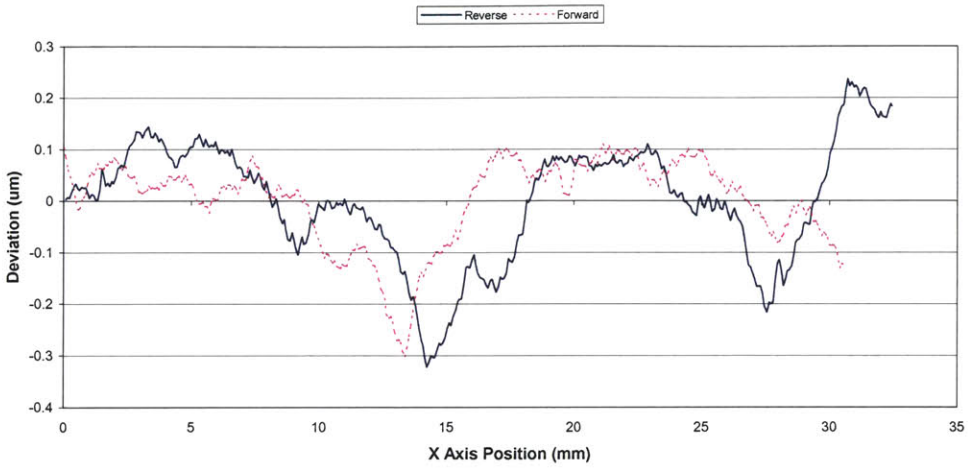

Figure 82: Prototype machine's horizontal straightness error measured at the work piece location.

It is possible that the recirculating balls in the ball nuts are causing the periodic error motions as a ball in a helical track must pass over an axial track and vice versa.

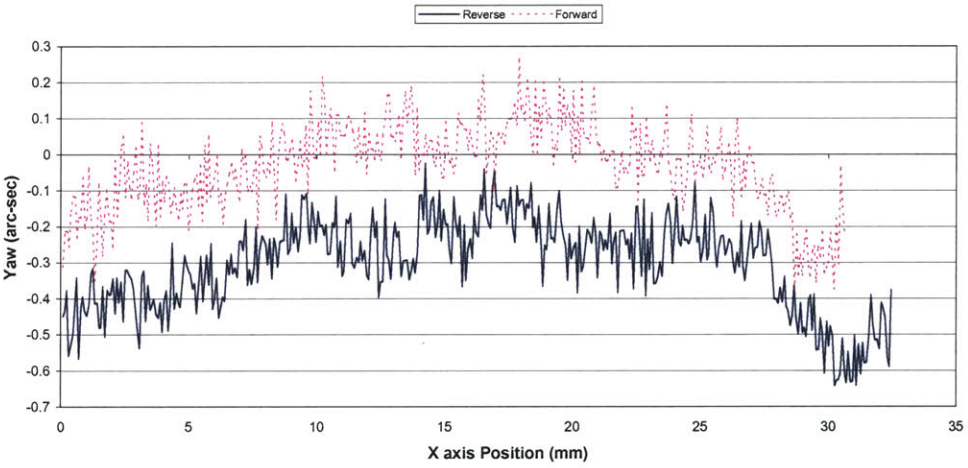

Figure 83: Prototype machine's Yaw error measured at the work piece location.

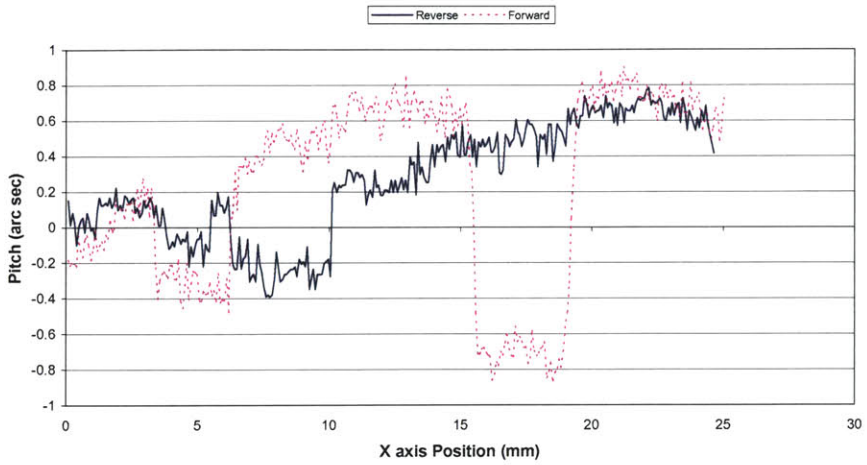

Figure 84: Prototype machine's Pitch error measured at the work piece location.

From these preliminary results, the prototype machine has the potential to meet the accuracy goal of ± 0.5 microns. Hence despite the balls having to cross tracks, the ball-screw spline system has great potential as a combined actuator/bearing/axis structure for meso-scale machines.

6.5.1 Sensors for the MesoMill

To detect the linear and rotary movement of the ball-screw spline shaft, an encoder is needed. Due to the complexity of the combined shaft movement, translation and rotation, neither a rotary nor linear encoder can be used separately because each encoder needs a fixed platform to work off of and with the combination of the two movements, this is not available. The solution is to wait for a prototype encoder that can detect translation along with rotary movement. This piece will be located at the end of the shaft next to, depending on which axis, the work piece or aerostatic spindle. Since this encoder will not be available until August 2004, the encoders on the motors that drive the capstan drives will be used.

7 Conclusion

The error budget indicated the machine concept is feasible, and tests on the prototype verify the next step is to machine parts and verify accuracy. The error budget predicted the error of the MesoMill to be 8 microns, but from experimentation it was shown to be 0.5 – 1 micron. The initial assumption of 10ppm estimation of random error is actually false. If 100ppm was inputed, then the results give a 3-5 μm random error. In addition 3 of the 5 axis have been built and were tested in the experiment above. Looking at just the work path error and not the spindle, the error of 1 - 0.5 μm is predicted and agrees with the measurements taken at NIST. As for the ball-screw spline, the assembly was simple and didn't require major machining. The only operation done was to cut the shaft to length. Through measurements, it was shown the spindle is only meant for higher speeds during cutting. Thus a higher speed spindle metrology is needed for further testing. Looking at some of the other components analyzed the wire capstan drive's stiffness was measured and 10% agrees with theory given the proper coefficient of friction.

In conclusion the basllscrew–spline is a great machine element for mesomachining and direct drive.

The Mesomill testbed has been assembled and is currently being integrated with the control system and the motors. Once the prototype of the encoder, due in August 2004, is finished, this too will be integrated in the system. In the meantime, the existing encoders on the motors will be used.

References:

[1] Proceedings of the *Manufacturing Three-Dimensional Components and Devices at the Meso and Micro Scales: A Workshop Cosponsored by the National Institute of Standards and Technology and the National Science Foundation,* Gaithersburg Maryland, 1999

[2] National Science Foundation workshop on M^4: Micro/Meso-Mechanical Manufacturing. Northwestern University: Evanston, IL, May 2000. http://216.239.53.100/search?q=cache:gGx0lQtiaTMC:www.mech.northwestern.edu/MFG/AML/M4/M4-Files/M4-REPORT.doc++site:www.mech.northwestern.edu+machines+meso+Illinois&hl=en&ie=UTF-8

[3] ROBOTOOL-Project, *Advanced Kinematics for Manufacturing Applications: List of existing parallel kinematics.* Last updated July 9, 2002. http://www.ifw.uni-hannover.de/robotool/pages/listeenglisch.htm

[4] Proceedings of the *Manufacturing Three-Dimensional Components and Devices at the Meso and Micro Scales: A Workshop Cosponsored by the National Institute of Standards and Technology and the National Science Foundation,* Gaithersburg Maryland, 1999

[5] National Science Foundation workshop on M^4: Micro/Meso-Mechanical Manufacturing. Northwestern University: Evanston, IL, May 2000. http://216.239.53.100/search?q=cache:gGx0lQtiaTMC:www.mech.northwestern.edu/MFG/AML/M4/M4-Files/M4-REPORT.doc++site:www.mech.northwestern.edu+machines+meso+Illinois&hl=en&ie=UTF-8

[6] Sherline Products, 2000/2010 8-directional mill. 1996: http://www.sherline.com/mill.htm

[7] Machine Tool Distributor.com *Precision Bench Top Mills.* Emarket America, Inc and American Machine Tools Corp., 2001: http://www.machinetooldistributor.com/bench_top_mills.htm

[8] Small Engineering: Specialists in engineering small parts. Website by: Blue Pyramid Software Ltd. Last visited 01/18/03. http://www.smallengineering.co.uk/capabilities.asp

[9] TechSoft Roland Modela: *3D Scanning and Modeling/Milling in one Low Cost Machine.* Date Last visited 01/18/03: http://www.techsoftuk.co.uk/page49.htm

[10] Modela PCB Manufacturer meta-tutorial by Brygg Ullmer. Last visited 01/18/03. http://web.media.mit.edu/~ullmer/tutorials/modela/

[11] Pathfinders, Incorporated HexVantage. © 1997-2002 Pathfinders Incorporated: http://my.execpc.com/~bkonkel/faq.html

[12] Low Inertia 6DOF Parallel Kinematic Mechanisms from PI, Sub-Micron Precision Hexapod Technology. Last viewed on 01/18/03: http://www.physikinstrumente.de/news/pdf/Hexapod_fold_finCrp.pdf

[13] Light Machines: an interlitek inc. division. © 1996-2003 Light Machines. Date visited 05/03: http://www.lightmachines.com/

[14] Sandia National Laboratories, Manufacturing Science and Technology Center. Last Modified on Nov 18, 2002: http://mfgshop.sandia.gov/1400_ext/1400_ext.htm

[15] Sandia National Laboratories: Meso-machining. Last modified on April 20, 2002: http://mfgshop.sandia.gov/1400_ext/1400_ext_MesoMachining.htm

[16] Center for Machine Tool Systems Research. Colleges of Engineering University of Illinois at Chicago and Urbana-Champaign. Date visited 02/03. http://mtamri.me.uiuc.edu/cmtsr/fy01-02.htm

[17] NSF Award Abstract - #0000386, "Development of Meso-Machine-Tools Systems". DeVor, Richard and Kapoor, Shiv. NSF Program: 1468 MANUFACTURING MACHINES & EQUIP. Field Application: 0308000 Industrial Technology. Program Reference Code 9146,9237,MANU. https://www.fastlane.nsf.gov/servlet/showaward?award=0000386

[18] Sarma, S. E. and Wright, P. K., "Reference Free Part Encapsulation: A New Universal Fixturing Concept," Journal of Manufacturing Systems 16 (1), 35-47, 1997

[19] THK *The Mark of Linear Motion, General Catalog.* Catalog No. 300-1E. THK CO., LTD.

[20] Qualfab Machining, Tool Sensor products. Copy right 1997. Last visited 5/ 30/03. http://www.qualfab.com/tool.html

[21] Gere, James M., *Mechanics of Materials*, 5th ed., Brooks/Cole, CA 2001

[22] Roberts, Michael, *Approximation of Air Bearings as Linear Point Springs: Verification of an Analytical Model for a New Five-Axis Machine Tool.* Massachusetts Institute of Technology, 2002.

[23] Beer, F.P. and E.R. Johnson, *Vector mechanics for Engineers Statics and Dynamics*, 6th ed., McGraw-Hill, Inc. New York 1997.

[24] F.M. Spotts, Design of Machine Elements, 6th ed. Prentice-Hall, Inc., NJ, 1985.

[25] G. Newton, "Selecting the Optimum Electric Servo-motor for Incremental Positioning Applications," 10th Symp.. Increment. Motion Control Syst. and Dev., B.C. Kuo (ed) pg. 353

[26] Slocum, Alexander, *Precision Machine Design.* SME, USA 1992, pp 644.

[27] ASME B89.3.4M – 1985 Axes of Rotation Methods for Specifying and Testing, ASME NY, NY 1985

[28] Lion Precision Instruction Manual Advanced Spindle Error Analyzer Version 7. Lion Precision, MN: 2000

[29] Lion Precision Instruction Manual Advanced Spindle Error Analyzer Version 7. Lion Precision, MN: 2000

[30] Tlusty, *Systems and Methods of Testing Machine Tools* . J.Microtechnic, Vol 13, 1959.

[31] U.S. Patient No. 06227777

[32] Machinery's Handbook, 26th ed. pg. 342

[33] Slocum, Alexander, *Precision Machine Design.* SME, USA 1992, pp 691 - 693.

Appendix A - Detailed Calculations

7.1 Error analysis

Table 22: Work path with movement in x and z directions. No movement in y can be performed in the work path.

	Part-to-fixture (D_5)		**Fixture to Disc** (D_4)		**Disc to Shaft** (D_3)	
Axes	Dimensions (mm)	Random Errors (μm)	Dimensions (mm)	Random Errors (μm)	Dimensions (mm)	Random Errors (μm)
X	**0.0**	**0.25**	**0.0**	**0.13**	**0.0**	**0.32**
Y	**0.0**	**0.25**	**0.0**	**0.13**	**0.0**	**0.32**
Z	**-25.4**	**0.25**	**-12.7**	**0.13**	**-12.7**	**0.32**
θX (rad)	**0.0**	**1.0E-5**	**0.0**	**1.0E-5**	**0.0**	**1.0E-5**
θY (rad)	**0.0**	**1.0E-5**	**0.0**	**1.0E-5**	**0.0**	**1.0E-5**
θZ (rad)	**0.0**	**1.0E-5**	**0.0**	**1.0E-5**	**0.0**	**1.0E-5**

	Shaft to Bearing (D_2)		**Bearing to Reference** (D_1)	
Axes	Dimensions (mm)	Random Errors (μm)	Dimensions (mm)	Random Errors (μm)
X	**0.0**	**1.68**	**-240.0**	**2.4**
Y	**0.0**	**1.68**	**0.0**	**2.4**
Z	**-125.7**	**1.68**	**0.0**	**2.4**
θX (rad)	**0.0**	**1.0E-5**	**0.0**	**1.0E-5**
θY (rad)	**0.0**	**1.0E-5**	**0.0**	**1.0E-5**
θZ (rad)	**0.0**	**1.0E-5**	**0.0**	**1.0E-5**

Table 23: Tool path: with movement in the x and y directions.

	Tool tip to Collet (D_6)		**Collet to Shaft** (D_7)		**Shaft to Bearing** (D_8)	
Axes	Dimensions (mm)	Random Errors (μm)	Dimensions (mm)	Random Errors (μm)	Dimensions (mm)	Random Errors (μm)
X	**0.0**	**0.1**	**0.0**	**2.5E-3**	**0.0**	**2.5E-3**
Y	**-44.4**	**0.1**	**-60.2**	**2.5E-3**	**12.7**	**2.5E-3**
Z	**0.0**	**0.0**	**0.0**	**0.0**	**0.0**	**0.0**
θX (rad)	**0.0**	**1.0E-5**	**0.0**	**1.0E-5**	**0.0**	**1.0E-5**
θY (rad)	**0.0**	**1.0E-5**	**0.0**	**1.0E-5**	**0.0**	**1.0E-5**
θZ (rad)	**0.0**	**1.0E-5**	**0.0**	**1.0E-5**	**0.0**	**1.0E-5**
	Bearings to holder (D_9)		**Holder to Shaft** (D_{10})		**Shaft to Bearings** (D_{11})	
Axes	Dimensions (mm)	Random Errors (μm)	Dimensions (mm)	Random Errors (μm)	Dimensions (mm)	Random Errors (μm)
X	**0.0**	**0.9**	**50.8**	**0.25**	**189.2**	**1.68**
Y	**-39.5**	**0.9**	**-131.4**	**0.25**	**0.0**	**1.68**
Z	**0.0**	**0.0**	**0.0**	**0.25**	**0.0**	**1.68**
θX (rad)	**0.0**	**1.0E-6**	**0.0**	**1.0E-5**	**0.0**	**1.0E-5**
θY (rad)	**0.0**	**1.0E-6**	**0.0**	**1.0E-5**	**0.0**	**1.0E-5**
θZ (rad)	**0.0**	**1.0E-6**	**0.0**	**1.0E-5**	**0.0**	**1.0E-5**
	Bearings to Reference (D_{12})					
Axes	Dimensions (mm)	Random Errors (μm)				
X	**0.0**	**0.0**				
Y	**227.4**	**2.7**				
Z	**0.0**	**0.0**				
θX (rad)	**0.0**	**0.0**				
θY (rad)	**0.0**	**0.0**				
θZ (rad)	**0.0**	**0.0**				

Table 24: Tool path movement in the x, y, and z axes. Work path is same case as previous.

	Tool tip to Collet (D_6)		**Collet to Shaft** (D_7)		**Shaft to Bearing** (D_8)	
Axes	Dimensions (mm)	Random Errors (μm)	Dimensions (mm)	Random Errors (μm)	Dimensions (mm)	Random Errors (μm)
X	**0.0**	**0.1**	**0.0**	**2.5E-3**	**0.0**	**2.5E-3**
Y	**-44.4**	**0.1**	**-60.2**	**2.5E-3**	**12.7**	**2.5E-3**
Z	**0.0**	**0.0**	**0.0**	**0.0**	**0.0**	**0.0**
θX (rad)	**0.0**	**1.0E-5**	**0.0**	**1.0E-5**	**0.0**	**1.0E-5**
θY (rad)	**0.0**	**1.0E-5**	**0.0**	**1.0E-5**	**0.0**	**1.0E-5**
θZ (rad)	**0.0**	**1.0E-5**	**0.0**	**1.0E-5**	**0.0**	**1.0E-5**
	Bearings to holder (D_9)		**Holder to Shaft** (D_{10})		**Shaft to Bearings** (D_{11})	
Axes	Dimensions (mm)	Random Errors (μm)	Dimensions (mm)	Random Errors (μm)	Dimensions (mm)	Random Errors (μm)
X	**0.0**	**0.9**	**50.8**	**0.25**	**189.2**	**1.68**
Y	**-39.5**	**0.9**	**92.9**	**0.25**	**0.0**	**1.68**
Z	**0.0**	**0.0**	**-92.9**	**0.25**	**0.0**	**1.68**
θX (rad)	**0.0**	**1.0E-6**	**0.0**	**1.0E-5**	**0.0**	**1.0E-5**
θY (rad)	**0.0**	**1.0E-6**	**0.0**	**1.0E-5**	**0.0**	**1.0E-5**
θZ (rad)	**0.0**	**1.0E-6**	**0.0**	**1.0E-5**	**0.0**	**1.0E-5**

	Bearings to Reference (D_{12})	
Axes	Dimensions (mm)	Random Errors (μm)
X	**0.0**	**2.7**
Y	**227.4**	**2.7**
Z	**0.0**	**2.7**
θX (rad)	**0.0**	**1.0E-5**
θY (rad)	**0.0**	**1.0E-5**
θZ (rad)	**0.0**	**1.0E-5**

7.2 Hertz Contact Stress on V-Block Mounting

Originally, mounting the shaft onto the base was done with a block of material that had a V-groove cut out. Since the mounting evolved to bolting the flange of the nuts to a 203 mm cube and the use of air bearings was no longer a choice, this idea is no longer in use. The preliminary calculation is discussed below. Two components, air bearings and ball screw-spline nuts will be encased in a cylinder that is placed within the V-groove. This allows for easy alignment. When placed in the V-groove, a clamp will be placed on top to keep the components secure. To make sure the force on top and on the sides of the cylinders do not interfere with the movement of the components inside, the hertz contact stress is calculated. Figure 85 gives a representation of the v-groove and definition of variables

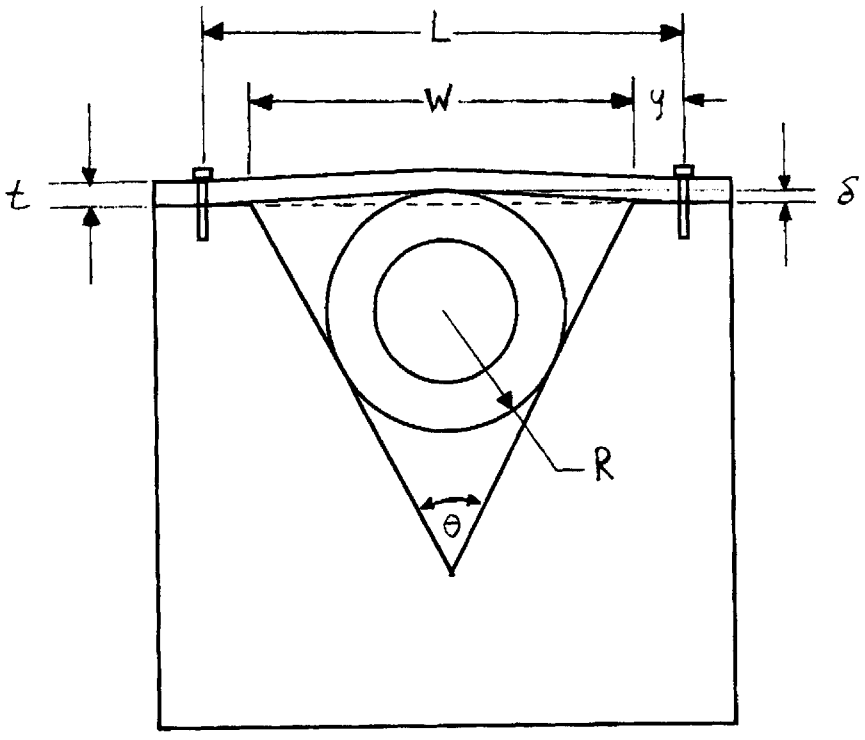

Figure 85: V-groove representation and definition of variables

Two components, v-block and cylinder are both composed of the same material, steel. The modulus of elasticity of steel is 2.00×10^{11} Pa and the Poisson ratio is 0.32. The beam that secures the cylinder is made out of aluminum and it's modulus of elasticity and Poisson ratio are 7.31×10^{10} Pa and 0.35 respectively. The contact between the two surfaces is equivalent to the contact between a sphere and flat plane. In this type of problem, the equivalent modulus of elasticity is determined with the elastic moduli and Poisson ratio of the two material [33].

$$E_e = \frac{1}{\frac{1-\eta_1^2}{E_1} + \frac{1-\eta_2^2}{E_2}} \tag{123}$$

The equivalent modulus of elasticity of the cylinder and V-block is 1.11×10^{11} Pa and similarly the cylinder and beam is 6.06×10^{10} Pa. The cylinder radius, length, and angle of the v-block are known values. From Figure 85, the geometry shows the depth of the V is

$$d = R + \frac{R}{\sin(\frac{\theta}{2})} - \delta \tag{124}$$

and the width is

$$w = 2d\tan(\frac{\theta}{2})$$

(125)

In the case of the beam, its width is the same as the length of the cylinder. The other variables known of the beam are y and thickness t. The moment of inertia is calculated using the shape of a rectangular beam. The equation looks like

$$I = \frac{qt^3}{12}$$

(126)

where q is the cylinder length or beam width. This value is needed to find the force that the beam inflicts on the cylinder. Deriving the equation using the same elastic curve equations used in the section on beam bending, results in a deflection of

$$\delta = \frac{FL^3}{48EI}$$

(127)

Solving for the force produced on the beam results in

$$F = \frac{48\delta EI}{L^3}$$

(128)

The difference between this and the normal force on the v-block is the angle theta and a factor of half the force. That is

$$F_n = \frac{\frac{F}{2}}{\sin(\frac{\theta}{2})}$$

(129)

Two equations are used to find the contact radius and contact area for the cylinder top and V-block.

$$b = \sqrt{\frac{2F(2R)}{\pi qE(2R + D_{plate})}}$$

(130)

$$a = 2qb$$

(131)

The difference is the contact radius for the cylinder top uses the force F and the V-block radius uses the normal force. These two equations are used in determining the deformation of four parts: on top of the beam, on top of the cylinder, on the V-block surface, and of the cylinder at the V-block. Those equations are:

$$\delta_{cylinder} = \frac{2F}{\pi q E_e}[\ln(\frac{2(2R)}{b}) - \frac{1}{2}] \tag{132}$$

$$\delta_{flat} = \frac{2F}{\pi q E_e}[\ln(\frac{2(2R)}{b}) - \frac{\eta}{2(1-\eta)}] \tag{133}$$

After these four deformations are determined, the net vertical deformation can be calculated with the following equation

$$\delta_{system} = \delta_{top\_beam} + \delta_{cylinder\_top} + \frac{\delta_{V-block\_surface}}{\sin(\frac{\theta}{2})} + \frac{\delta_{cylinder\_v-block}}{\sin(\theta)} \tag{134}$$

The two deformations, V-block surface and cylinder at the V-block, are divided by sine functions because the vertical component is what is sought. The deflection of the system is 5.3 microns. The maximum contact pressure q (not to be confused with the cylinder length or beam width) that results from the system is 56.1 MPa and is calculated using the following equation

$$q = \frac{2F}{\pi b L} \tag{135}$$

Lastly, the maximum shear stress is 18.7 MPa and is one-third the maximum contact pressure q.

7.3 Drive system – Dual Pinion

A dual pinion consits of one central wormgear and two worms attached to either side. The second worm is to eliminate backlash by creating a preload force. To determine the stiffness of the individual teeth, one tooth can be modeled like a fixed beam and the elastic curve equations can be used to determine the deflection. The following equation results with the system shown below. Note the boundary conditions are all zero because there are no shear, moment, angle, or deflection forces on the beam when x is zero.

$$q = F < x-b >_{-1} + V < x >_{-1} + M < x >_{-2}$$
$$V = -F < x-b >^{0} - V < x >^{0} - M < x >_{-1}$$
$$M = F < x-b >^{1} + V < x >^{1} + M < x >^{0}$$
$$EI\theta = \frac{F}{2} < x-b >^{2} + \frac{V}{2} < x >^{2} + M < x >^{1}$$
$$EI\delta = \frac{F}{6} < x-b >^{3} + \frac{V}{6} < x >^{3} + \frac{M}{2} < x >^{2}$$

The deflection equation can be reduced further because V and M are known from the reaction froces.

$$V = -F$$

(136)

$$M = Fb$$

(137)

Thus the equation becomes

$$EI\delta = \frac{F}{6} < x-b >^{3} - \frac{F}{6} < x >^{3} + \frac{Fb}{2} < x >^{2}$$
$$\delta = \frac{F}{6EI}(< x-b >^{3} - < x >^{3} + 3b < x >^{2})$$

(138)

When x is equal to b, the first term goes to zero and the equation looks like this

$$\delta = \frac{Fb^{3}}{3EI}$$

(139)

To find the stiffness of the tooth, the above equation is rearranged to produce force over displacement.

$$K = \frac{3EI}{b^{3}}$$

(140)

Since the beam is rectangular, the inertia is

$$I = \frac{1}{12} t^{3} h$$

(141)

$$K = \frac{Et^3 h}{4b^3}$$

(142)

This makes the stiffness a function of modulus of elasticity (E), thickness (t), height (Ht), and length of contact between two teeth (b). In order to solve for the above variables the following terms must be known: circular pitch of worm gear (P), axial pitch of worm (P_x), lead angle of worm (*lambda*), helix angle of wormgear (*psi*), number of threads in worm (n), and number of teeth in wormgear (N_g). With these known variables, the following equations, which are in any "Mechanical Engineering Handbook", determine the thickness, height, and length of contact between two teeth.

Normal circular pitch of worm and wormgear

$$P_n = P_x \cos(\lambda)$$

(143)

Ratio of gearing

$$m_g = \frac{N_g}{n}$$

(144)

Lead angle

$$l = nP_x$$

(145)

Addendum

$$a = 0.3183P_n$$

(146)

Whole depth

$$Ht = 0.7003P_n + 0.002$$

(147)

Working depth

$$Hk = 0.6366P_n$$

(148)

Clearence

$$c = Ht - Hk$$

(149)

Tooth thickness

$$t = 0.5P_n$$

(150)

Pitch diameter in worm

$$d = \frac{l}{\pi \tan(\lambda)}$$

(151)

Pitch diameter in wormgear

$$d_g = \frac{N_g P}{\pi}$$

(152)

Center distance

$$center = 0.5(d + d_g)$$

(153)

Outside diameter of wormgear

$$d_{g\_out} = 2center - d + 2a$$

(154)

Contact length for worm

$$b_{worm} = Ht - (\frac{d_{out}}{2} - \frac{d}{2})$$

(155)

Contact length for wromgear

$$b_{gear} = Ht - (\frac{d_{g\_out}}{2} - \frac{d_g}{2})$$

(156)

Now that the thickness, contact length, and height are known, the stiffness can be calculated. The overall stiffness of the system is similar to three springs in series. That is

$$\frac{1}{K_{tot}} = \frac{1}{K_{shaft}} + \frac{1}{K_{w\_gear\_torsional}} + \frac{1}{K_{worm\_torsional}}$$

(157)

Before the torsional stiffness is found, the spring stiffness of the worm and wormgear is divided by a factor of safety of four. This number accounts for the tooth being almost the same height and thickness. Since torsional stiffness is sought, the spring stiffness is multiplied by the radius of the worm and wormgear. Thus tosional stiffness looks something like this

$$K_{worm\_torsional} = K_{worm}\frac{d^4}{4} \tag{158}$$

$$K_{w\_gear\_torsional} = K_{w\_gear}\frac{d_g{}^4}{4} \tag{159}$$

When calculated the overall stiffness of the dual pinion is on the order of 20^4 N-m/rad.